Mass measurements on neutron-deficient nuclides at SHIPTRAP and commissioning of a cryogenic narrow-band FT-ICR mass spectrometer

Von Rafael Ferrer García
geb. in Valencia (Spanien)
Mainz, 2007

Zusammenfassung

Die vorgelegte Doktorarbeit behandelt hochpräzise Massenspektrometrie an kurzlebigen Radionukliden mittels Penningfallen. Aufgrund der Fähigkeit alle Kernwechselwirkungen zu Tage zu bringen, können Massenmessungen weitab der β-Stabilitätslinie neue Einsichten zum gegenwärtigen Wissen über nukleare Eigenschaften liefern und die Vorhersagemacht von Massenmodellen sowie -gleichungen testen. Auf dem Gebiet der nuklearen Astrophysik dienen atomare Massen als grundlegende Parameter um Kernsynthese in stellarem Umfeld zu verstehen. In dieser Arbeit werden zehn Massenwerte von Radionukliden um $A = 90$ vorgestellt, die den vorhergesagten Pfad des rp-Prozesses durchsetzen. Sechs davon wurden zum ersten Mal experimentell bestimmt. Die Messungen wurden am Penningfallenmassenspektrometer SHIPTRAP durchgeführt unter Ausnutzung der destruktiven Flugzeit-Ionenzyklotronresonanz (TOF-ICR) Nachweismethode. Da die Leistungsmerkmale des TOF-ICR Nachweises der Erforschung von schweren/superschweren Spezies mit kleinen Produktionsquerschnitten ($\sigma < 1\,\mu$b) Grenzen setzt, wurde ein neues Nachweissystem unentbehrlich. Im zweiten Teil dieser Arbeit wird die Inbetriebnahme eines kryogenen Doppel-Penningfallensystems diskutiert, in dem eine hochsensitive, schmalbandige Fouriertransformation-Ionenzyklotronresonanz (FT-ICR) Nachweismethode zur Anwendung gebracht wird. Mit der nicht-destruktiven FT-ICR Nachweismethode liefert ein einzelnes, einfach geladenes gespeichertes Ion bereits die notwendige Information um dessen Masse zu bestimmen. Es wird berichtet über erste "off-line" Experimente mit einem neuen Detektorsystem basierend auf einem "Channeltron" mit angehängter Konversionsdynode, mit einer kryogenen Pumpsperre, die ultrahohe Vakuumbedingungen während der Massenbestimmung garantiert, und schließlich mit der für die Einzelionnensensitivität benötigten Nachweiselektronik.

Summary

The dissertation presented here deals with high-precision Penning trap mass spectrometry on short-lived radionuclides. Owed to the ability of revealing all nucleonic interactions, mass measurements far off the line of β-stability are expected to bring new insight to the current knowledge of nuclear properties and serve to test the predictive power of mass models and formulas. In nuclear astrophysics, atomic masses are fundamental parameters for the understanding of the synthesis of nuclei in the stellar environments. This thesis presents ten mass values of radionuclides around $A = 90$ interspersed in the predicted rp-process pathway. Six of them have been experimentally determined for the first time. The measurements have been carried out at the Penning-trap mass spectrometer SHIPTRAP using the destructive time-of-flight ion-cyclotron-resonance (TOF-ICR) detection technique. Given the limited performance of the TOF-ICR detection when trying to investigate heavy/superheavy species with small production cross sections ($\sigma < 1$ μb), a new detection system is found to be necessary. Thus, the second part of this thesis deals with the commissioning of a cryogenic double-Penning trap system for the application of a highly-sensitive, narrow-band Fourier-transform ion-cyclotron-resonance (FT-ICR) detection technique. With the non-destructive FT-ICR detection method a single singly-charged trapped ion will provide the required information to determine its mass. First off-line tests of a new detector system based on a channeltron with an attached conversion dynode, of a cryogenic pumping barrier, to guarantee ultra-high vacuum conditions during mass determination, and of the detection electronics for the required single-ion sensitivity are reported.

Contents

List of Figures

List of Tables

Chapter 1

Introduction

The ground-state properties of an exotic nucleus such as half-life, decay mode, decay energy, and mass are usually the first experimental information obtained for a new nuclide. Among all these, the ground-state mass is of particular importance since all nuclear interactions and correlations contribute to it. Their sum is expressed as the nuclear *binding energy B*, which is a measure of how much energy has been gained through the strong force by forming the nucleus from its single constituents. Thus, the nuclear binding energy is defined as the difference in mass between a nucleus $^A_Z X_N$ and its constituents, Z protons and N neutrons, and it is written as

$$B(Z, N) = \left[Zm_p + Nm_n - m(^A X) \right] c^2 . \tag{1.1}$$

Since the binding energy depends on the detailed composition of protons and neutrons, the mass of each of the more than 3500 nuclides as observed today is highly specific and represents a key property of nuclear systems [1].

Most of the present-day knowledge about the atomic nucleus is based on the properties of nuclei close to the line of β-stability where the proton-to-neutron ratio is similar to the one of the stable nuclei. However, the extrapolation of this knowledge to the region far from stability is difficult and already now it is clear that some of the basic knowledge of nuclear physics has to be reviewed. For instance, by experimentally mapping the mass surface and improving the theoretical mass formulas it becomes evident that clustering [2] and nucleon correlations create more binding than previously anticipated and thus, more exotic nuclei are expected to be bound.

The dependence of the nuclear interaction on the isospin degree of freedom is believed to bring clear answers on a number of aspects of the nuclear interactions and dynamics. Studying nuclei under extreme conditions of isospin (completely different from stable nuclei) will not only provide a stringent check of the actual knowledge but is also closely related to the discovery of new and exciting phenomena [3].

In literature, one speaks of two categories of mass measurements: so-called indirect techniques like, *e.g.*, reactions and decays, that produce Q-values, or energy differences; and direct mass spectrometry techniques, where time-of-flight or cyclotron-frequency measurements of the exotic species are combined with those of well-known reference masses, linking them finally to ^{12}C, from which the mass unit is defined. While a decade ago most of the masses of radioactive nuclei were deduced indirectly from their decay characteristics and were closer to stability, the manipulation of radio-active beams has advanced so much that direct mass-measurement

techniques, such as Penning-trap and storage-ring mass spectrometry, have provided high sensitivity and high-precision tools for a detailed investigation of nuclear binding far from the valley of stability [4, 5].

For nuclear structure studies, first and second derivatives of the mass surface along isotopic and isotonic chains, *i.e.* specified differences between the mass of two nearby nuclei, provide information about shell structures and phase transitions via separation energies. The fact that the strong interaction between the nucleons cannot be treated in a perturbative way and that the small number of nucleons does not allow the use of statistical methods, in addition to the presence of the weak and electromagnetic forces, cause the atomic nucleus to be among the richest and most challenging of the quantum systems. As a consequence, the binding energy cannot be treated by ab-initio theories and one has to rely on mass predictions by models and formulas [6]. These models make a description of the nucleus in a macroscopic or microscopic approach and are applied depending on the nuclide or the particular nuclear property being studied. There are even models which combine the best part of different approaches in order to describe the species or predict properties of nuclei not experimentally accessible.

A well-known prediction of nuclear models is the existence of a region of long-lived superheavy elements (SHE) beyond the actinides. This enhanced nuclear stability against spontaneous fission is due to closed shells in the structure of both protons and neutrons. However, theoretical approaches to date do not yield consistent predictions of the precise limits of the *island of stability*, which requires experimental studies in this region [7]. Experimental work at the velocity filter SHIP did show that the spontaneous fission was more stable due to deformed shell stabilization and led to the discovery of six new elements at GSI [8], the most recents darmstadtium ($Z = 110$) and roentgenium ($Z = 110$).

Another important application of high-accuracy mass spectrometry on radionuclides are the tests of fundamental interactions and the Standard Model. Here, the unitarity of the Cabibbo-Kobayashi-Maskawa (CKM) quark-mixing matrix and the conserved-vector-current (CVC) hypothesis are ultimately tested by mass measurements on nuclides which undergo *superallowed nuclear β-decay* [9].

Among the many applications of mass measurements, one of the most demanding is that of nuclear astrophysics, which plays a vital role in understanding the structure and the isotopic composition of the Universe. The energy in stars is generated through nuclear reactions between stable as well as radioactive nuclei in the so-called process of nucleosynthesis. This process can be steady during hydrostatic burning stages of stellar evolution on long timescales or sometimes it can be explosive, involving a time scale of seconds [10]. Some of the most important scenarios of matter creation in stars are (see Fig. 1.1):

- *s-process*: the slow neutron capture leads to the build-up of heavy elements along the line of β-stability during He-burning. A series of neutron capture and beta-decays, starting on existing heavy nuclei around iron (Fe), end up with the synthesis of elements up to lead (Pb) and bismuth (Bi).

- *r-process*: the explosive rapid neutron capture involves species with high density of neutrons (near the neutron drip line) leading to the formation of the heaviest elements in nature like thorium (Th), uranium (U), and plutonium (Pu).
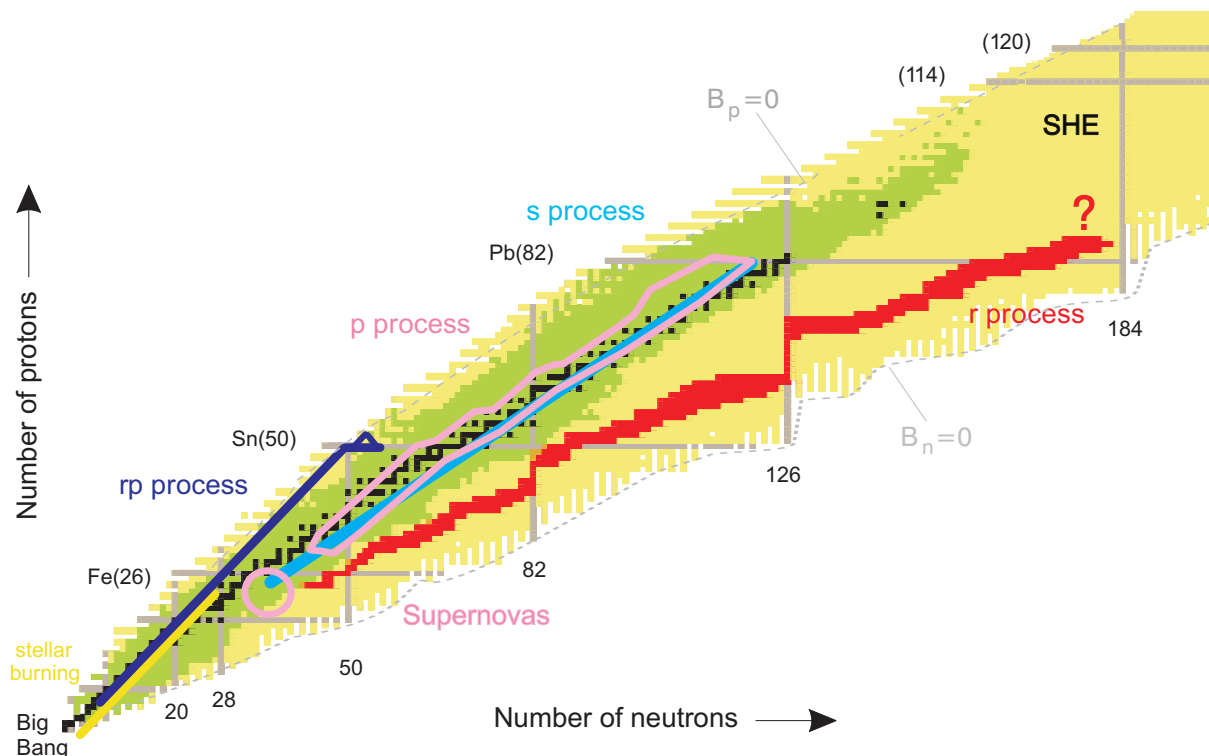
Figure 1.1: Chart of the nuclides showing the main processes of nuclear synthesis in stars [10]. Stable elements are indicated with black squares while green squares show radionuclides with known masses and/or half-lives. The yellow squares represent experimentally unknown radionuclides predicted by nuclear theory to exist, delimited by the proton dripline ($B_p = 0$) and neutron dripline ($B_n = 0$) [3]. The r- and rp-processes proceed far-off stability where experimental mass values are highly demanded to reveal their nucleosynthesis mechanisms. The endpoint of the r-process, in the vicinity of the superheavy elements (SHE), is still unknown.

- *rp-process*: represents a sequence of rapid proton capture and subsequent beta-decays, responsible for the burning of hydrogen into heavier elements near the proton drip line. This process powers for example type I X-ray bursts, which occur when a neutron star accretes hydrogen rich matter from a companion star in a binary system [11].

The s-process is believed to be generally understood [12], mainly because the masses and half-lives of the involved nuclei are sufficiently well known. The r-process path, however, proceed along species that are not yet available at radioactive beam facilities and therefore its evolution across the nuclide chart is not clearly known. In this situation nuclear astrophysics is forced to rely on nuclear mass models and theoretical predictions, which sometimes disagree by several MeV.

Concerning the rp-process, precision mass measurements on neutron-deficient species have been performed at SHIPTRAP in the framework of this thesis and are still ongoing with the goal to clarify the pathway, nuclear abundances, and endpoint of this process [13].

The second chapter of this thesis reviews the theory of the Penning trap, since it is considered to be the heart of the mass spectrometer and has been developed

within this work, followed by the discussion of the main sources of ion production and detection techniques in the third and fourth chapter, respectively. The fifth chapter is devoted to the presentation of the SHIPTRAP mass spectrometer facility and the experimental mass measurement procedure. In the following chapter the mass values of ten species involved in the rp-process will be presented; six of them have been experimentally determined for the first time. In the last part of the thesis the commissioning of a new setup based on a non-destructive detection technique is reported and some results of first off-line tests are presented. In the region of superheavy elements the experimentally found low production rates ($< 1/s$), but with rather long half-lives species, make no longer possible the application of the conventional time-of-flight ion-cyclotron-resonance (TOF-ICR) detection technique. Here, the non-destructive Fourier-transform ion-cyclotron-resonance detection technique (FT-ICR) is ideally suited and will be applied with the setup constructed within this thesis for the very first time to short-lived radionuclides. The new experimental data in the heavy/superheavy region will enable to constrain the choice of theoretical mass models and improve their predictions, allowing for a decisive test of the predictive power of the models and providing an extended and reliable basis for the adjustment of their parameters, all of great benefit for nucleosynthesis calculations.

Part I

Theory

Chapter 2

Theory of ion traps

Ion traps have been extensively used in fundamental and applied physics and chemistry research [14, 15] since F.M. Penning published first his work in the late 1930s [16] about an application of electromagnetic fields on charged particles. He found a way of increasing the sensitivity of ion gauges by applying an axial magnetic field. Since it forces the charged particles to orbit around the field lines, the ions travel a longer path between the electrodes. This configuration, however, does not yet represent a full confinement in three dimensions since there are no electrodes to avoid that the particles escape along the magnetic field axis. One decade later, J.R. Pierce [17] added *end hats* in the axial direction and described in detail an electron trap using the geometric configuration that represents the actual *Penning trap*.

Aiming for an improvement of the classical mass spectrometers, W. Paul and coworkers investigated a new device for mass spectrometry [18], which is known today as radiofrequency quadrupole (RFQ) mass filter [19]. This two-dimensional storage device was extended in 1953 to a storage tool capable to confine charged particles with a certain charge-to-mass ratio q/m in all three dimensions [20], nowadays known as *Paul trap* [21].

There are different types of ion traps, but the two most important ones are Penning traps and Paul, or radiofrequency, traps. A common feature is their ability to confine ions in a small volume in well-controlled fields apart from external influences. Therefore, ion traps can be considered as a very important tool to perform precision experiments like it is done in mass spectrometry [4]. However, in the field of high-accuracy mass spectrometry Paul traps are commonly used only as beam preparation tools, since their mass resolution is limited by the stability of the electric field. Hence, Penning traps are the ones used to perform high-precision experiments and have become already famous for the high sensitivity and accuracy reached in a number of measurements. The first most famous measurement was the determination of the electron *g-factor* by Dehmelt[1] *et al.*, with a precision of $4 \cdot 10^{-12}$ [22]. This result, together with theoretical calculations, served to define the fine structure constant α until last year when a new measurement of the electron *g-factor* was performed by Gabrielse *et al.* [23], which improved the former one by a factor of six. Current experiments in this line study the *g-factor* of bound electrons in highly-charged ions as a sensitive test of bound-state quantum electrodynamics (BS-QED) [24, 25]. Other key experiments are the determination of the mass ratios of electron and positron [26, 27] and proton and antiproton [28]. The latter one

---

[1]Dehmelt was the one who proposed the name Penning trap.
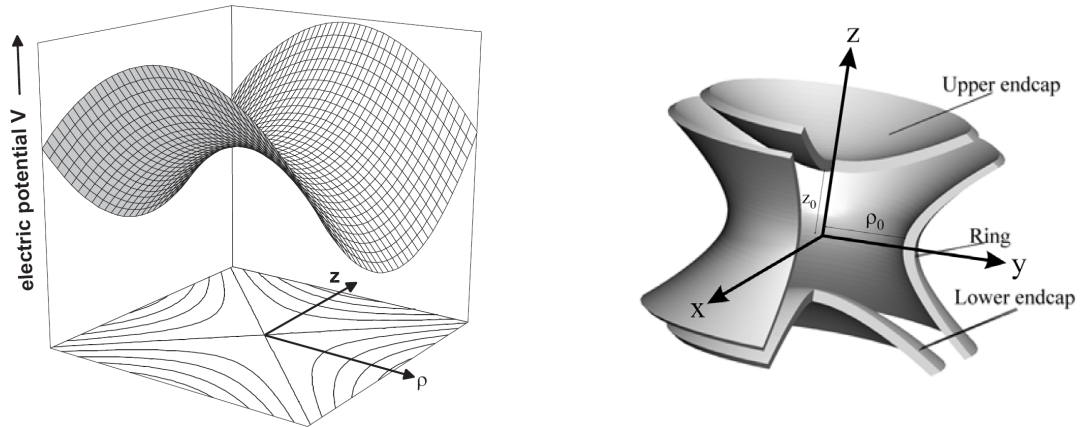
Figure 2.1: (Left) Quadrupole potential V as a function of the cylinder coordinates ρ and z. The projection shows the equipotential lines [30]. (Right) Ideal electrode configuration for the generation of an axially symmetric quadrupole potential. The inner surfaces of the electrodes are hyperboloids and follow equipotential surfaces of the electric field.

has a precision of 10^{-10} and represents the most precise hadronic test of the charge, parity, and time (CPT) reversal theorem. Wolfgang Paul and Hans G. Dehmelt were awarded the Nobel Prize for physics in 1989 for *the development of the ion trapping techniques* [21, 29].

2.1   Generation of the electric trapping potential

An inherent property of the Penning and Paul trap is their ability to create a potential minimum in all three dimensions. In one dimension, the parabola represents the lowest polynomial function that produces a potential in which an ion can be trapped. In the case of three dimensions and assuming cylindrical symmetry, the Laplace equation leads to a potential in the form $V \propto \rho^2 - z^2/2$, where ρ is the distance from the z-axis. Such a potential represents a quadrupole, as illustrated in Fig. 2.1 (left). A common feature of both techniques is the use of a quadrupole potential that ensures a linear force on the trapped particles and therefore harmonic oscillations around the trap center with their motional frequencies being independent of the amplitudes. The graphical representation of the quadrupole potential clearly reveals that it only enables a confinement in the radial or axial direction, depending on the polarity and the ion's charge.

The easiest way of creating an axially symmetric quadrupole potential is to choose a set of electrodes with a shape that follows the equipotential surfaces. Such an electrode configuration is depicted in Fig. 2.1 (right) and consists of two end electrodes, so-called endcaps and a ring electrode, which in the ideal case are hyperboloids of revolution that obey the surface equations

$$z^2 = \frac{\rho^2}{2} + z_0^2 \,, \tag{2.1}$$
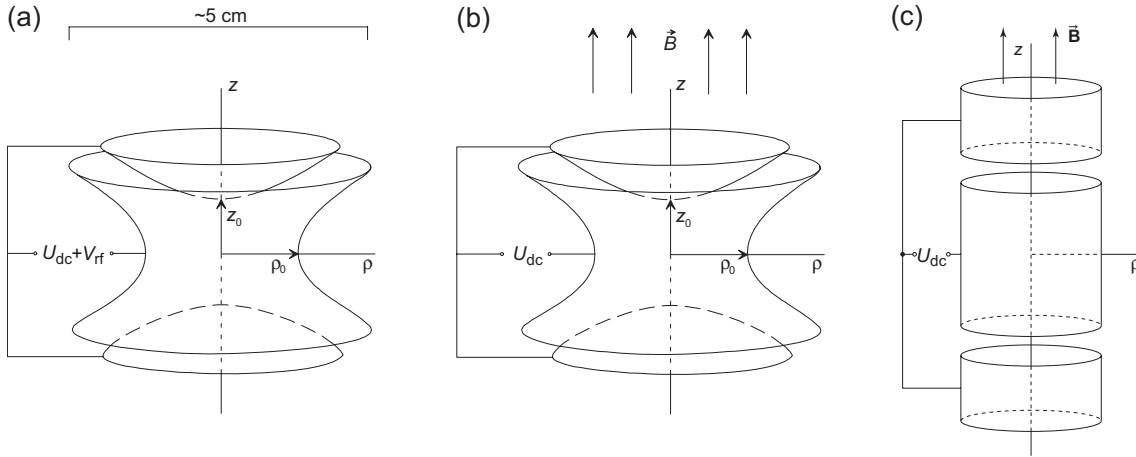
Figure 2.2: Configuration of electrodes for a Paul (a) and a Penning trap (b,c), consisting of a ring electrode and two endcaps with hyperbolical shape (a,b) or cylindrical shape (c).

for the two endcaps and

$$z^2 = \frac{1}{2}(\rho^2 - \rho_0^2) \ , \rho \geq \rho_0 \tag{2.2}$$

for the ring electrode, with z_0 and ρ_0 being the shortest distances from the electrode surfaces to the center of the trap (see Fig. 2.1 (right)). The same ones are also used to define the characteristic trap dimension

$$d = \sqrt{\frac{1}{2}(z_0^2 + \rho_0^2)} \ . \tag{2.3}$$

If a voltage difference U is applied between the two endcaps and the ring electrode, as shown in Fig. 2.2, this electrode configuration will generate the desired quadrupole potential,

$$V(\rho, z) = \frac{U}{2d^2}\left(\frac{\rho^2}{2} - z^2\right) . \tag{2.4}$$

Since the Laplace equation does not permit an absolute potential minimum in all three dimensions by pure electrostatic fields, the three-dimensional confinement in the case of the Paul trap is achieved by applying an oscillating radiofrequency field as shown schematically in Fig. 2.2 (a). This alternating field causes the potential to change polarity, forcing the ion to slide back from the remaining free direction, keeping the ion stored in the center of the trap. As already mentioned this trap is well suited for ion storage as well as for ion cooling and bunching [31, 32] (see also Chap. 5). In the case of the Penning trap the confinement is achieved by the force due to combined magnetic and electric fields. Figures 2.2 (b,c) illustrate two different electrode geometries for the Penning configuration. The presence of the strong and homogeneous magnetic field is the basic requirement for Penning trap mass spectrometry. Here, the mass determination relies on the measurement of an ion's cyclotron frequency in the way it will be explained later since it is the main topic of the work presented here. For this reason, in the following, only the Penning trap technique will be considered, disregarding the Paul trap formalism and leaving
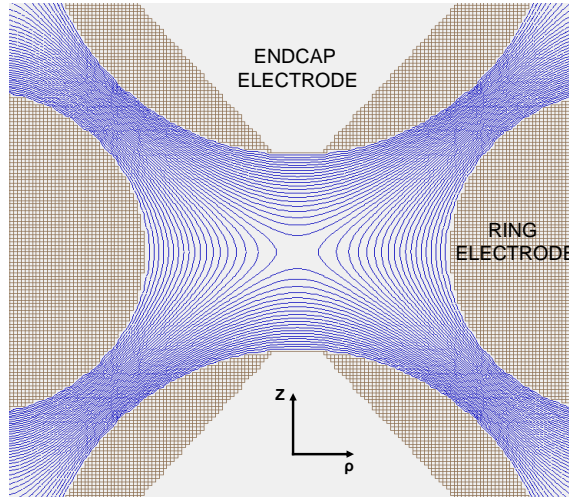
Figure 2.3: Simulation of a quadrupolar electric field generated as a result of applying a potential difference $U = 20$ V between the endcaps and the ring electrode.

only for a subsequent section a more detailed description of the application of the RFQ traps.

2.2   Description of the ion motion in a Penning trap

An ion with charge-to-mass ratio q/m stored in a pure magnetic field $\vec{B} = \vec{B}(z)$, and moving with a velocity component $\vec{v}$, experiences a Lorentz force $\vec{F} = q\vec{v} \times \vec{B}$ that confines the particle in a radial plane perpendicular to the field lines. The ions undergo a circular motion with angular frequency

$$\omega_c = \frac{q}{m}B, \tag{2.5}$$

known as the free cyclotron frequency. Due to the absence of any force in the direction of the magnetic field lines, *i.e.* in the axial direction, an electric potential U like in Eq. (2.4) is applied for the three dimensional confinement. This potential is the source of an electric field (see Fig. 2.3) of the form

$$\vec{E} = \frac{U}{2d^2}(x, y, -2z), \tag{2.6}$$

where d represents the characteristic trap dimension defined in Eq. (2.3). The combination of a magnetic field in z-direction and the electrostatic quadrupole potential produces a force on the charged particles which leads to the following set of differential equations:

$$\ddot{x} - \omega_c \dot{y} - \frac{\omega_z^2}{2} x = 0$$
$$\ddot{y} + \omega_c \dot{x} - \frac{\omega_z^2}{2} y = 0$$
$$\ddot{z} + \omega_z^2 z = 0,$$

$$(2.7)$$

with the free cyclotron frequency ω_c given in Eq. (2.5) and

$$\omega_z = \sqrt{\frac{qU}{md^2}}, \tag{2.8}$$

being defined as the axial oscillation frequency of the harmonic motion along the trap axis. Solving the equation of motion for all three coordinates results in three independent motional modes

$$x = \rho_+ \sin(\omega_+ t + \phi_+) + \rho_- \sin(\omega_- t + \phi_-)$$
$$y = \rho_+ \cos(\omega_+ t + \phi_+) + \rho_- \cos(\omega_- t + \phi_-)$$
$$z = \rho_z \sin(\omega_z t + \phi_z),$$

$$(2.9)$$

where $\rho_{+,-,z}$ and $\phi_{+,-,z}$ represent the amplitudes and phases of the motions, respectively. This set of solutions can be seen as the superposition of three harmonic oscillators as illustrated in Fig. 2.4. One in the axial direction with the axial eigenfrequency ω_z and two radial motions with eigenfrequencies

$$\omega_+ = \frac{\omega_c}{2} + \sqrt{\frac{\omega_c^2}{4} - \frac{\omega_z^2}{2}} \tag{2.10}$$

and

$$\omega_- = \frac{\omega_c}{2} - \sqrt{\frac{\omega_c^2}{4} - \frac{\omega_z^2}{2}}. \tag{2.11}$$

Thus, the addition of the electric field has three effects on the ion motion: It not only provides the restoring force that confines the ion motion in the axial plane with frequency ω_z, but it also reduces the free cyclotron frequency ω_c to ω_+, the so-called reduced cyclotron frequency, and in addition introduces a slow magnetron precession ω_-. The magnitude of the eigenfrequencies follow the order $\omega_- < \omega_z < \omega_+$ and fulfill the conditions

$$\omega_c = \omega_+ + \omega_- \tag{2.12}$$

$$2\omega_+ \omega_- = \omega_z^2 \tag{2.13}$$

$$\omega_c^2 = \omega_+^2 + \omega_-^2 + \omega_z^2. \tag{2.14}$$

Equations 2.12 and 2.14 show the two main options available for the mass determination of the stored ions: (i) a direct observation of the cyclotron frequency sideband
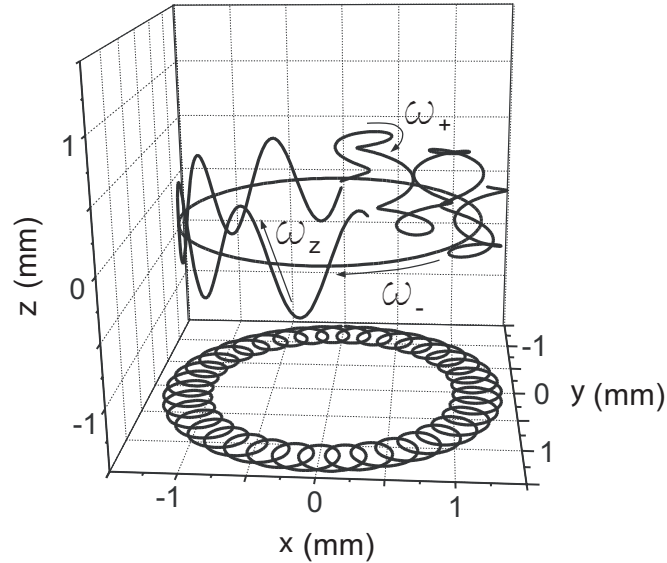
Figure 2.4: Illustration of the ion trajectory (three-dimensional and projection on the x-y plane) with the three independent eigenmotions in an ideal Penning trap: a harmonic oscillation in the axial direction with frequency ω_z and a radial motion as the combination of the reduced cyclotron motion with frequency ω_+ and the magnetron motion with frequency ω_-.

ω_c (see Sec. 4.1) or (ii) a measurement of the individual frequencies, either the two radial or all three eigenfrequencies. Both techniques will be discussed in the next chapter. Notice that Eq. (2.14) is independent of trap and field imperfections to first order and is called *The Invariance Theorem* [33].

It is useful to consider the energy of the motion in order to understand some features of the ion motion in a Penning trap. The total energy of an ion stored in a Penning trap is the sum of the kinetic and potential energies of each eigenmotion,

$$E = E_+ + E_z + E_- = \frac{m}{2}\rho_+^2(\omega_+^2 - \omega_+\omega_-) + \frac{m}{2}\rho_z^2\omega_z^2 + \frac{m}{2}\rho_-^2(\omega_-^2 - \omega_+\omega_-). \quad (2.15)$$

The potential energies $-e(U/d^2)\rho_\pm^2 = -m\rho_\pm^2\omega_z^2 = -\frac{m}{2}\rho_\pm^2(\omega_+\omega_-)$ of the two radial motions are negative due to the potential hill the ions experience in the radial direction. Since $\omega_+ > \omega_-$, we can see from Eq. (2.15) that the total energy of the magnetron motion is always negative. This has important consequences in case of energy loss of the ion motion as it will be discussed in the context of the cooling techniques in Sec. 2.5. For the axial and cyclotron[2] motion a decrease of the amplitude is accompanied by a loss of energy. In contrast to this, the magnetron motion increases its amplitude while losing energy.

2.3   The real Penning trap

So far we have supposed that the hyperbolically-shaped configuration shown in Fig. 2.1 generates a perfect quadrupole electric field, but in reality it cannot fully

---

[2]I refer to cyclotron motion as the motion related with the frequency ω_+, which from now on I will call cyclotron frequency. The name free cyclotron frequency will be used for ω_c.
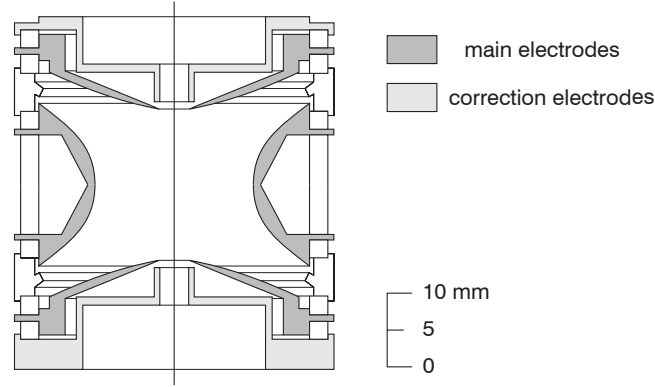
Figure 2.5: Illustration of a real hyperbolical precision Penning trap. The set of correction electrodes counteract the deviation from the ideal quadrupole field due to the truncation of the electrodes and the holes for injection and ejection of the ions.

accomplish this task since the electrodes do not extend to infinity. The result of such a truncation is the presence of higher-order multipole components in the trapping potential. More deviations from the ideal Penning trap are, *e.g.*, generated by field inhomogeneities, trap imperfections, and misalignment of the trap axis with respect to the magnetic field axis, among other. All these effects that set apart the electric potential from its pure quadrupole geometry, lead to a dependence of the motional frequencies on the motional amplitudes. This produces a shift of the eigenfrequencies, resulting in a limitation of the resolving power and in an increase of the systematic uncertainties in the mass determination. For this reason an accurate investigation of these imperfections is demanded in order to design a high-precision Penning trap mass spectrometer. In the following the most important trap imperfections will be briefly discussed. For a more detailed study of these effects refer to [34, 35].

- *Electric field imperfections*: They are present due to the inherent geometrical imperfections of the trap construction such as the holes in the endcaps for injection/ejection of the ions or, as mentioned already, from the inevitable truncation of the electrodes. As a result, a deviation from the pure quadrupole field as defined in Eq. (2.4) is produced, that generally is expressed in terms of a multipole expansion of the trapping potential. For the sideband frequency $\omega_c = \omega_+ + \omega_-$, the frequency shift $\Delta\omega_c^{\mathrm{elec}}$ depends on the amplitudes of the individual eigenmotions in the form

$$\Delta\omega_c^{\mathrm{elec}} = \Omega_c^{\mathrm{elec}} \left[\frac{3}{2}\frac{C_4}{d^2}(\rho_-^2 - \rho_+^2) + \frac{15}{4}\frac{C_6}{d^4}(\rho_z^2(\rho_-^2 - \rho_+^2) - (\rho_-^4 - \rho_+^4)) \right] \quad (2.16)$$

with

$$\Omega_c^{\mathrm{elec}} = \frac{\omega_-}{1 - \omega_-/\omega_+} \approx \omega_- \approx \frac{U_0}{2d^2 B} \quad (2.17)$$

and C_4 and C_6 being the coefficients of the octupole and dodecapole components of the electric field. Notice that $\Delta\omega_c^{elec}$ is in a good approximation mass-independent due to the mass independence of Ω_c^{elec}. These deviations of the ideal quadrupole field and the resulting frequency shifts are minimized
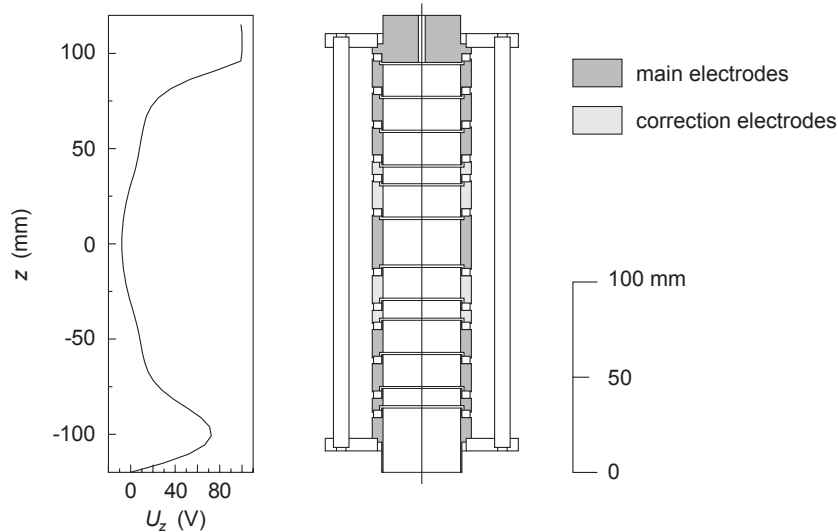
Figure 2.6: Illustration of a real cylindrical Penning trap. The graph on the left shows the potential on axis that results from the suitable voltages applied to the cylinder segments (right).

by the addition of compensation or correction electrodes to the Penning trap configuration. Figures 2.5 and 2.6 show as examples real hyperboloidal and cylindrical Penning traps, very similar to the ones used in our setup (see Chap. 7). A deviation of the trap axis relative to the magnetic-field axis also causes systematic uncertainties in the mass determination since it shifts all eigenfrequencies. For the sideband frequency $\omega_+ + \omega_-$ the shift produced $\Delta\omega_c^{\mathrm{tilt}}$ can be calculated and is found to be also mass-independent. For small tilting angles $\alpha \ll 1$, the shift is given by

$$\Delta\omega_c^{\mathrm{tilt}} \approx \frac{9}{4}\omega_-\sin^2\alpha \ . \tag{2.18}$$

- *Magnetic field instabilities and imperfections*: Magnetic field inhomogeneities and fluctuations are very important sources of uncertainty in high-precision Penning trap mass spectrometry. In the following some of the processes which lead to a change in the strength of the magnetic field are listed:

  1. The current flowing through the superconducting coils slowly decreases in a permanent way due to the impurities which are present in the superconducting material. The effect is known as *flux creep* phenomenon [36]. This drift of the magnetic field strength can be described approximately in modern solenoids by a linear decrease [37].

  2. Objects close to the superconducting magnet with some magnetic susceptibility are easily magnetized, distorting in consequence the field of the magnet.

  3. Fluctuations of the temperature and pressure in the nitrogen and helium vessels of the superconducting magnet cause a change in the magnetic permeability of the materials surrounding the Penning trap, such

as the vacuum chamber and the trap material itself, and therefore of the magnetic-field homogeneity and strength [38].

When the magnetic field is a function of the even powers of the distance from the trap center, a frequency shift is introduced. In such cases the ion experiences average magnetic fields that depend on the amplitude of its motion. The lowest multipole term of interest is a magnetic hexapole component β_2 that creates a frequency shift given by

$$\Delta\omega_c^{\text{magn}} \approx \beta_2 \omega_c (\rho_z^2 - \rho_-^2). \tag{2.19}$$

- *Ion-Ion interaction*: The presence of two different species, *i.e.* having different mass, in the trap content affects the ion motion and thus the cyclotron frequency of the species under investigation due to the Coulomb interaction with the other one[3]. If the resolving power is not large enough a single resonance at a common center of gravity is observed. If different resonances can be resolved, both frequencies shift to lower values and the shift is depending on the number of ions, as shown in [40]. In order to perform high-accuracy trap experiments it is very important to have a pure ion sample stored in the trap. If that is not the case, there is a way of minimizing the effect of the Coulomb interaction by measuring the cyclotron frequency for groups of different number of stored ions and extrapolating it to a single stored ion in the trap [41] (see also Chap. 6).

2.4 Excitation of the ion motion

The resonant excitation of the ion motion with an external radiofrequency (rf) field is a very important tool in various preparation steps of the mass measurement procedure and even in the mass determination itself (see Sec. 4.1). It is applied for the manipulation of the individual eigenmotions, as, *e.g.*, in the removal of contaminant ion species. This excitation can be made very selective and its effect depends on the applied frequency amplitude and the multipolarity of the rf field.

2.4.1 Dipolar excitation

The application of a dipolar rf field in either the radial or axial direction can be used to change the amplitude of the corresponding motion independently. Such a field is created by an rf voltage applied with a 180° phase-shift between two opposite segments of the ring electrode (see Fig. 2.7 (a)). It drives one of the radial motions if the suitable frequency is used, *e.g.*, for the radial x-component:

$$\vec{E}_x = \frac{U_d}{a}\cos(\omega_{\text{rf}} t - \phi_{\text{rf}})\hat{x}, \tag{2.20}$$

with a being the radius formed by the electrodes ($a = r_0$ in Fig. 2.7) and U_d, ω_{rf} and ϕ_{rf} being the amplitude, frequency and phase of the dipolar field, respectively. In the

---

[3]For ions of the same species simultaneously stored the driving frequency acts on the q/m center of the ion cloud and no frequency shift is observed [39].
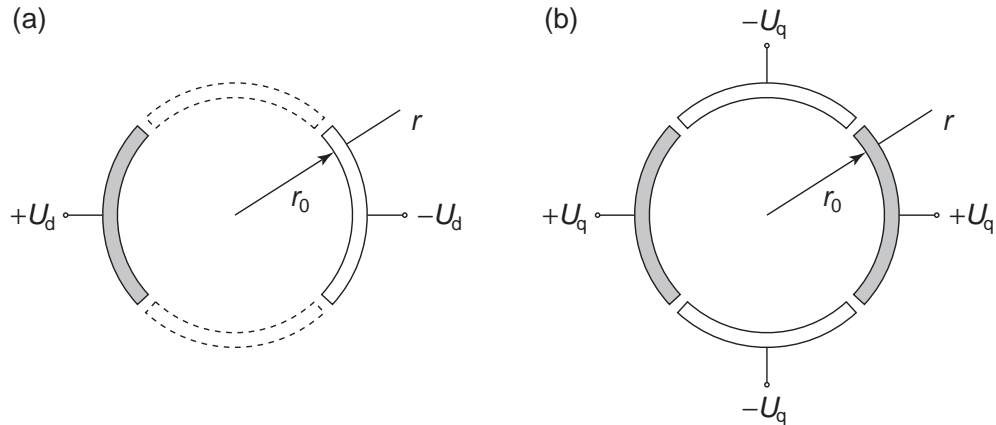
Figure 2.7: Electrode configuration for the creation of a dipolar (a) or a quadrupolar (b) field using a segmented ring electrode.

same way an axial dipolar field generated by applying an rf voltage between both endcaps will drive the axial motion if the frequency is in resonance, *i.e.*, if $\omega_{\rm rf} = \omega_z$. In resonance, the amplitude of an eigenmotion will increase linearly, but the initial behavior will depend on the initial position and velocity of the ion and the phase of the rf field. Assuming an injection of the ions in the center of the trap with a narrow velocity distribution, the effect on the motion's amplitude is governed only by the phase difference between the dipolar excitation signal and the ion eigenmotion, as illustrated in Fig. 2.8 for the magnetron motion. In Sec. 4.1 we will see that this phase difference can be fixed in practice. This technique is known as phase-locked excitation of the magnetron motion [42] and allows to apply the dipolar field automatically in the most efficient way, directly increasing the magnetron radius linearly up to the required amplitude.

2.4.2   Quadrupolar excitation

The quadrupolar excitation is the other important multipolarity used in common practice. Quadrupolar rf fields enable the manipulation of the ion motion by excitation at differences or sums of the eigenfrequencies. The most important case taking into account its application to mass spectrometry is the case at the sum frequency $\omega_+ + \omega_-$ of the magnetron and cyclotron motion (see Eq. 2.12). This excitation geometry is achieved by an azimuthal quadrupole generated by a four-fold segmented ring electrode, as illustrated in Fig. 2.7 (b) and with the form:

$$\vec{E}_x = \frac{2U_q}{a^2}\cos(\omega_{\rm rf}t - \phi_{\rm rf})y\hat{x} \tag{2.21}$$

$$\vec{E}_y = \frac{2U_q}{a^2}\cos(\omega_{\rm rf}t - \phi_{\rm rf})x\hat{y}, \tag{2.22}$$

with all parameters in analogy to Eq. (2.20) but for the quadrupole field. The quadrupole or sideband excitation $\omega_+ + \omega_-$ has a very important usage in mass spectrometry since this sum frequency equals the free cyclotron frequency $\omega_c = qB/m$. In addition, this sideband excitation is of importance in respect to the buffer-gas cooling
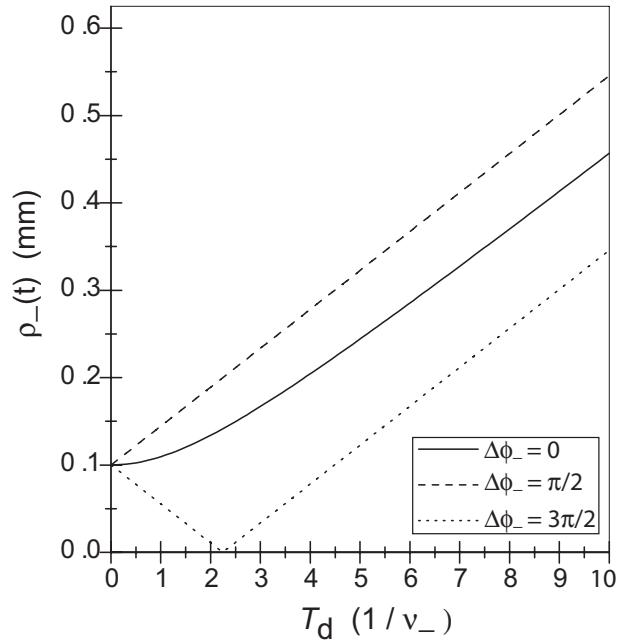
Figure 2.8: Magnetron radius as a function of the duration of the dipolar excitation. The behavior is given for three values of the phase difference between the excitation and the final magnetron motion [42].

technique in Penning traps, which will be described in the next section. The most important feature of this excitation is that it couples the two radial motions in a periodical way as illustrated in Fig. 2.9, where initially the ion is prepared such that it has only magnetron motion. When the azimuthal field at $\omega_q = \omega_c$ is applied the amplitude of the magnetron motion decreases while the cyclotron amplitude increases. After a certain time (depending on the amplitude U_q of the excitation) the magnetron motion has disappeared and the amplitude of the cyclotron motion is that of the initial magnetron one. The total effect is a harmonic beating between the magnetron and cyclotron motion [30]. For $\omega_{\rm rf} = \omega_c$ the beating frequency Ω_0 is proportional to the amplitude $V_{\rm rf}$ of the rf field[4]. For $\omega_+ \gg \omega_-$ it is

$$\Omega_0 = \frac{V_{\rm rf}}{a^2} \frac{1}{4B}, \tag{2.23}$$

being practically mass independent. A conversion between a pure magnetron motion into a pure cyclotron motion is performed after a time $T_{\rm conv}$, that is half of the beating period

$$T_{\rm conv} = \frac{\pi}{\Omega_0} = \frac{4\pi a^2 B}{V_{\rm rf}}. \tag{2.24}$$

If the initial condition does not correspond to a pure magnetron or cyclotron motion, the beating will not be completed and the minimum and maximum amplitudes will depend on the initial ones, as well as on all phases involved. For this reason, in

---

[4]If a fourfold-segmented ring electrode with inner radius $r_0 = a$ is used for the creation of the azimuthal quadrupole field, then U_q is to first order equal to the amplitude $V_{\rm rf}$ of the oscillating voltages applied to the ring segments [43].
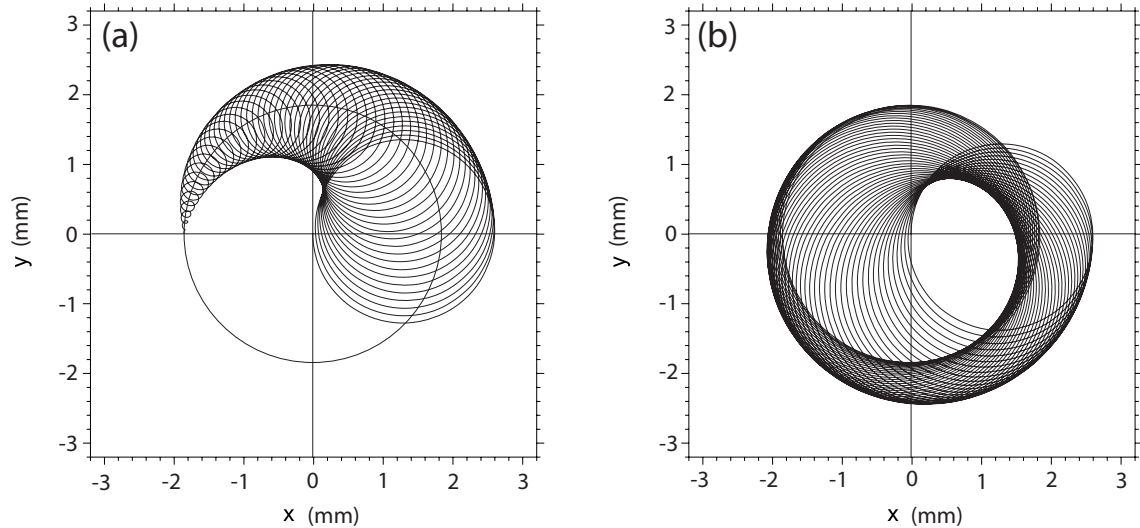
Figure 2.9: Conversion of radial motions under a quadrupolar excitation at $\omega_{\mathrm{rf}} = \omega_c$. The motion starts with a pure magnetron component (a), indicated by the circle, and ends after a time T_{conv} in a pure cyclotron motion (b). Part (a) shows the first part of the conversion, (b) the second half.

practice one tries to perform a situation the most similar to the ideal case depicted in Fig. 2.9.

The radial kinetic energy E_r is proportional to the revolving frequency of the trapped ion:

$$E_r \propto \omega_+^2 \rho_+(t)^2 - \omega_-^2 \rho_-(t)^2 \approx \omega_+^2 \rho_+(t)^2, \tag{2.25}$$

with ρ_+ and ρ_- being the amplitudes of the cyclotron and magnetron motion, respectively. As we will see in Sec. 4.1, the coupling of these two motions produces an increase of the radial kinetic energy and therefore of the associated magnetic moment. The radial energy gain as a function of the detuning $\Delta\omega = \omega_{\mathrm{rf}} - \omega_c$ for a rectangular excitation profile is described by (see Fig. 2.10)

$$E_r \propto \frac{\sin^2(\omega_b T_{\mathrm{rf}})}{\omega_b^2}, \tag{2.26}$$

with

$$\omega_b = \frac{1}{2}\sqrt{(\omega_{\mathrm{rf}} - \omega_c)^2 + (\omega_{\mathrm{conv}}/2)^2}. \tag{2.27}$$

From a measurement of such a profile one can determine the free cyclotron frequency ω_c of the trapped ions, as we will see later in Sec. 4.1.

Recently, studies have been done to investigate the applicability of an azimuthal octupolar field to excite the stored ions in a Penning trap. Here, the excitation is performed at $2\omega_c$. The technique still requires further testing but the first results indicate that $2\omega_c$ excitation may provide benefits that are similar to doubling the magnetic field strength B [44, 45].
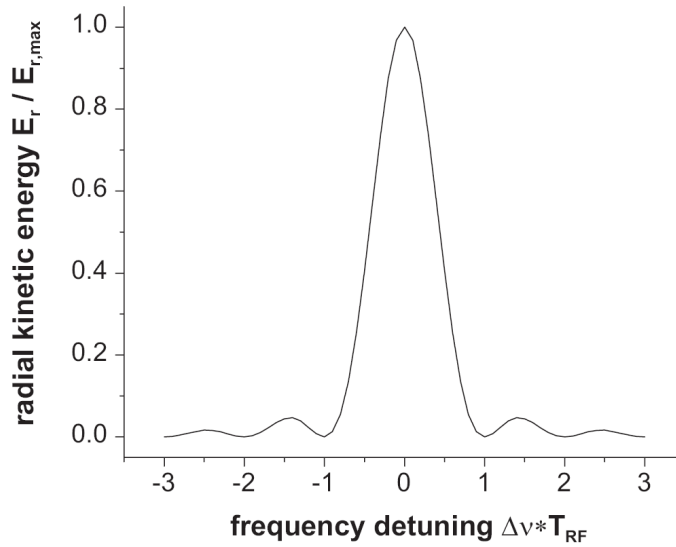
Figure 2.10: Radial energy gain of the ion motion in case of a quadrupole excitation near ω_c as a function of the detuning $\Delta\omega = \omega_{\text{rf}} - \omega_c$ [30].

2.5   Cooling techniques

The main purpose of cooling in traps is to reduce the motional amplitudes of the stored ions and consequently to reduce the effects of trap imperfections on the determination of the individual frequencies, as discussed already in Sec. 2.3. The cooling techniques that have been developed for stored ions in Penning traps are resistive dissipation of energy in a cold external circuit via the image currents induced in the trap electrodes, laser cooling, *i.e.* interaction with an intense laser beam of appropriate wavelength, sympathetic cooling with cold charged particle clouds, evaporation cooling, and buffer gas cooling, *i.e.* damping the motional amplitudes by collisions with noble gas atoms [4].

For mass measurements on short-lived radionuclides, within the scope of this work, the four first techniques are not applicable. The current induced in an external circuit for resistive cooling is proportional to the ion frequency and for heavy ions this is not high enough to achieve an efficient cooling in the time available, that is limited by the half-life of the species. Laser cooling allows to cool down to sub-Kelvin temperatures, but optical transitions of suitable wavelengths are required from the species under investigation, limiting so its applicability to only a few particular element species. This restriction could be overcome by using laser-cooled ions for sympathetic cooling of another ion species, but as we discussed in Sec. 2.3, effects of Coulomb interaction between the two clouds of different ion species modify the eigenmotions, perturbing the measurable eigenfrequencies. Evaporation cooling is also not possible since typically only a few ions are available per second. Thus, for mass spectrometry of singly-charged radionuclides buffer gas cooling is the most relevant and will be discussed in the following in more detail.
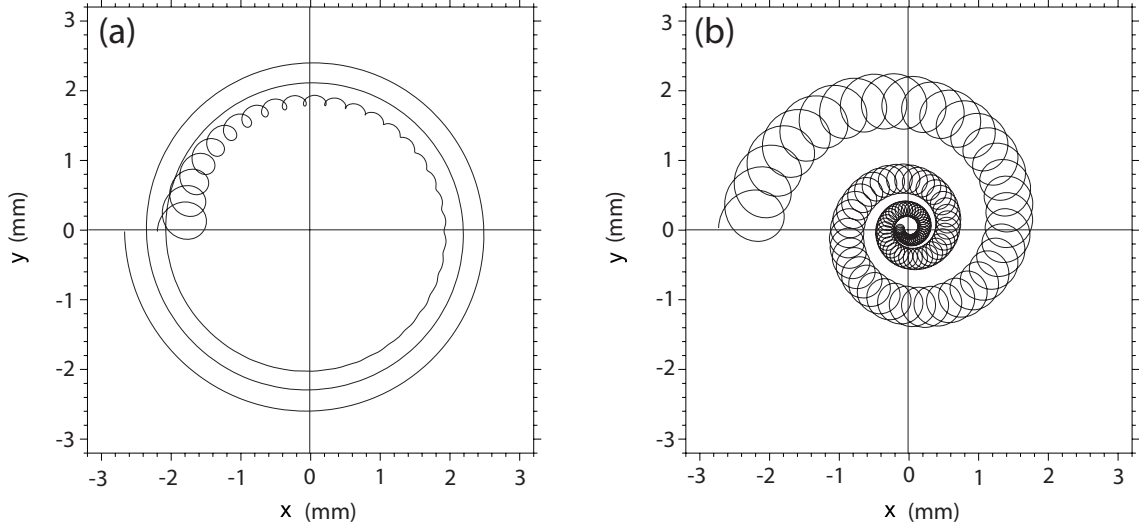
Figure 2.11: Simulation of the ion trajectory in the radial plane perpendicular to the magnetic field, under presence of a damping force produced by a buffer gas. In (a) a fast damping of the cyclotron motion and a slow increase of the magnetron motion are observed. In (b) the effect of an additional excitation with an azimuthal quadrupole field of frequency ω_c is shown. Both cyclotron and magnetron motions are decreased and a mass-selective centering is achieved.

2.5.1 Buffer gas cooling

In the buffer gas cooling technique the trap is filled with a buffer gas which provides the necessary damping environment to decrease the energy of the ions and consequently cool them down until a thermal equilibrium with the gas molecules is reached. Usually a noble gas is used at a pressure of about 10^{-5} mbar and at room temperature. As we will see later in Chap. 7, within this thesis a cryogenic Penning trap operated at liquid nitrogen temperature has been developed allowing buffer gas cooling at 77 K. The damping force can be approximated as a velocity dependent viscous force for a simple analytical formulation [46]

$$\vec{F} = \delta \cdot \dot{\vec{x}}, \tag{2.28}$$

being δ the damping constant. After the addition of this force the equations of motion (2.7) become

$$\begin{pmatrix} \ddot{x} \\ \ddot{y} \\ \ddot{z} \end{pmatrix} - \frac{\omega_z^2}{2} \begin{pmatrix} x \\ y \\ -2z \end{pmatrix} - \begin{pmatrix} \omega_c \dot{y} - \frac{\delta}{m}\dot{x} \\ -\omega_c \dot{x} - \frac{\delta}{m}\dot{y} \\ -\frac{\delta}{m}\dot{z} \end{pmatrix} = 0. \tag{2.29}$$

The axial motion, still independent of the radial motion, represents now a damped oscillator

$$z = A_z' e^{-(\delta/2m)t} \cos(\omega_z' t - \phi_z'), \tag{2.30}$$

where

$$\omega_z' = \sqrt{\omega_z^2 - \left(\frac{\delta}{2m}\right)^2}. \tag{2.31}$$

Combining the two radial equations into a complex one and using the ansatz $u = e^{-i(\omega t - \alpha)}$, one obtains the solution of the radial part

$$\begin{pmatrix} x \\ y \end{pmatrix} = \rho_- e^{\alpha_- t} \begin{pmatrix} \cos(\omega'_- t - \phi_-) \\ \text{-}\sin(\omega'_- t - \phi_-) \end{pmatrix} + \rho_+ e^{\alpha_+ t} \begin{pmatrix} \cos(\omega'_+ t - \phi_+) \\ \text{-}\sin(\omega'_+ t - \phi_+) \end{pmatrix}, \qquad (2.32)$$

where $\omega'_\pm = \omega_\pm \pm \Delta\omega$ and

$$\Delta\omega = \frac{1}{16} \cdot \left(\frac{\delta}{m}\right)^2 \cdot \frac{8\omega_z^2 + \left(\frac{\delta}{m}\right)^2}{(\omega_c^2 - 2\omega_z^2)^{\frac{3}{2}}}. \qquad (2.33)$$

As we can see from these solutions, the radial motion in the presence of a damping force is still composed of two circular motions, but now comparing with the undamped case, the frequencies are shifted up and down, respectively, by $\Delta\omega$ from the cyclotron ω_+ and magnetron ω_- frequencies. These frequency shifts are very small and can be neglected in most cases. On the other hand, since the shifts are equal in magnitude and opposite in direction, their sum and therefore ω_c remains unchanged. The amplitude of the motions $\rho(t) = \rho_0 \cdot e^{-\alpha t}$ change exponentially with time constant $\alpha_\pm$ given by

$$\alpha_\pm = -\frac{\delta}{2m} \left[1 \pm \left(1 + \frac{1}{8} \frac{8\omega z^2 + \left(\frac{\delta}{m}\right)^2}{\omega_c^2 - 2\omega_z^2} \right) \right]. \qquad (2.34)$$

Taking into account that $\omega_c \gg \omega_z$, we can conclude that the cyclotron amplitude decreases with a time constant $\alpha_+ \approx -\delta/m$ and the magnetron amplitude increases with a shorter time constant $\alpha_- \approx (\delta/2m) \cdot (\omega_z/\omega_c)^2$, due to the addition of the buffer gas. In order to overcome this increase of the magnetron radius, which would result in a loss of the ions by hitting the trap electrodes (see Fig. 2.11(a)), an azimuthal quadrupole excitation at the free cyclotron frequency $\omega_c = \omega_+ + \omega_-$ is applied to couple the two radial motions for the ion of interest (see also Sec. 2.4.2). In combination with the buffer gas, the quadrupolar excitation continuously converts the magnetron into cyclotron motion, resulting in an overall centering of the ions of interest [47]. An illustration of the process is shown in Fig. 2.11(b). Notice that this net centering of the ions can be made mass-selective due to the dependency of ω_+ on the ion mass.

Chapter 3

Ion production mechanisms

3.1 Methods of ion production

Several ionization processes are possible: electron ionization, chemical ionization, spray ionization, photo ionization, thermal ionization, surface ionization, etc. In the following, only the two ionization techniques of relevance for this work will be considered in more detail. For a pedagogic review of the different ionization methods refer to [48].

3.1.1 Surface ionization

Surface ionization is a process known to generate low-energy and low-temperature ions with a narrow distribution of ion energy. These properties make surface ionization a widely used method in mass spectrometry to produce ions of inorganic samples, especially for isotope analysis [49]. Such an ionization scheme is also applied for the production of reference ions for the mass determination of short-lived species in Penning traps (see Sec. 4.1).

The process of surface ionization (SI) combines elements of low ionization potentials ϕ, mainly alkali and earth-alkali elements, as ion products and a hot surface of a metal with a high work function W, like tungsten, rhenium, etc., as the ionizer medium. The ionization efficiency, or fractional ionization, is described by the Saha-Langmuir equation [50] as

$$\frac{n_+}{n_0} = \frac{g_+}{g_0} \cdot e^{\left[\frac{-e(\phi_i - W)}{kT_s}\right]}, \tag{3.1}$$

where n_+ and n_0 are the number densities of the ionic and the neutral species, $g_{+/0} = 2\mathrm{J}_{+/0} + 1$ are the statistical weights of the ionic and atomic ground state, respectively[1], and e, k, and T_s are the electron charge, Boltzmann's constant, and the temperature of the surface. There are different ionization mechanisms depending on the temperature or kind of compound being used in every case [51]. Here, by simplicity, the surface ionization process of a pure alkali metal is described. The ionization process is represented schematically by

$$\mathrm{M}_g \overset{\text{adsorption}}{\rightarrow} \mathrm{M}_a \overset{\text{ionization}}{\rightarrow} \mathrm{M}_a^+ + e_a^- \overset{\text{desorption}}{\rightarrow} \mathrm{M}_g^+ + e_a^-, \tag{3.2}$$

---
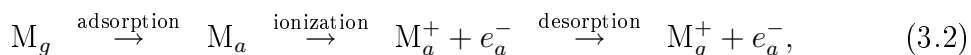
[1]For example $g_0 = 2$ and $g_+ = 1$ for alkalies ($^2S_{1/2}$ atomic ground state and $^1S_0$ ionic ground state).
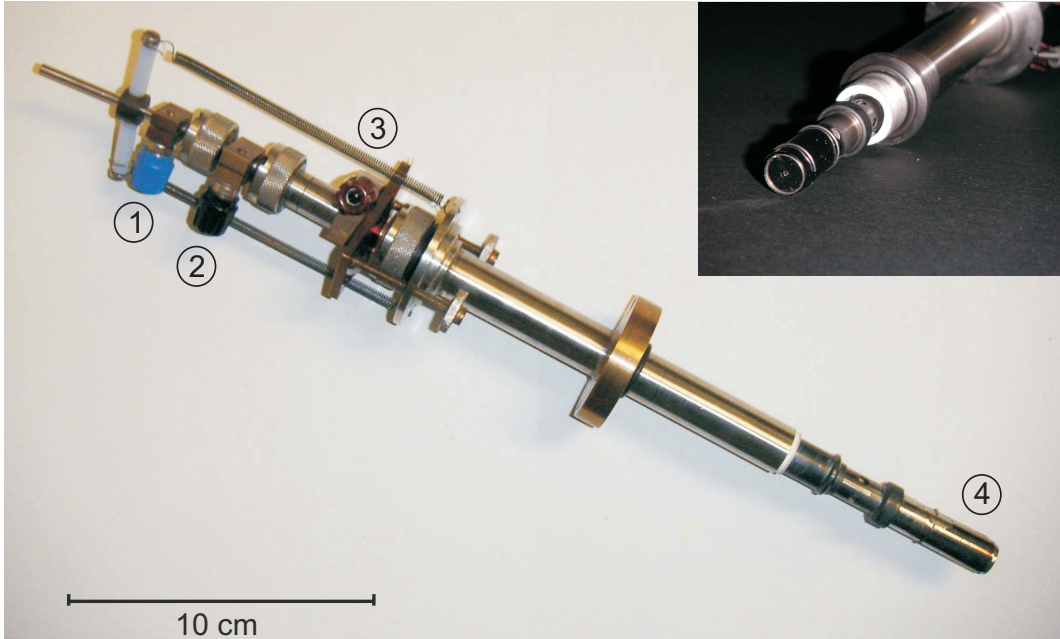
Figure 3.1: Surface ionization source of hot-cavity filled with cesium-zeolite $(Cs_{12}\,[(AlO_2)_{12}(SiO_2)_{12}]\cdot(27H_2O))$. The connectors (1) and (2) are used to apply the current to a filament for the electron bombardment of the tungsten cup (4). Through the connector (3) a bias voltage is supplied to the metallic surface to produce the desorption and to give some kinetic energy to the ions.

where the subscripts g and a indicate the gaseous and the adsorbed species on the hot surface, respectively. The process is described as follows:

1. the metal vapor contacts the hot surface and is adsorbed;

2. an electron is drawn into the surface due to the high work function ionizing the metal atom;

3. the metal ion is released (desorbed) from the surface by application of a positive bias voltage.

The surface ionization source used in our experiment was manufactured at GSI by R. Kirchner (see Fig. 3.1) and is based on the hot-cavity thermal ion source type [52], which shows a higher ionization efficiency with respect to common surface ionizers. Here, a tungsten cup ($W = 4.5\ eV$) located in the tip of the source and heated by electron bombardment, acts as cavity in whose interior a compound of cesium zeolite is deposited. The zeolite is a mineral that has a micro-porous structure where the Cs atoms can be inserted by means of a chemical process [53]. By heating the zeolite, the Cs atoms are released and then ionized at the cavity's wall surface. The ionization efficiency for ions extracted from the volume of the cavity may exceed the surface ionization efficiency given in Eq. (3.1) by orders of magnitude, even though surface ionization is the only ionizing mechanism of relevance. The reason is the accumulation of ions in the plasma formed inside the cavity due to a flux of glow electrons and surface-ionized particles from the wall into the volume, see [54] for a detailed discussion.

3.1.2   Electron impact ionization

Another method used for the ion production in our laboratory is the ionization by electron bombardment, also known as electron impact ionization (EI). This process occurs when an energetic electron (10 - 100 eV) strikes a molecule or atom and takes away an electron from the outer orbitals. Again the ionization process involved can have different scenarios depending on the electron (projectile) energy and the atom/molecule composition. The simplest case for the ionization of a molecule is described as follows:
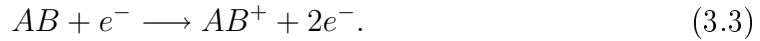
$$AB + e^- \longrightarrow AB^+ + 2e^-. \tag{3.3}$$

Notice that this process could end with a molecule ionization and dissociation if the electron energy imparted to the molecule in the collision exceeded the molecular binding energy, $AB + e^- \longrightarrow A + B^+ + 2e^-$, extracting an atom-ionic beam out of a molecular sample.

In this work an *Axial Molecular Beam Ionizer* produced by *ABB Automation Inc* was used (see Fig. 3.2). The technical features are described in detail in App. A, thus only the working bases will be given here.
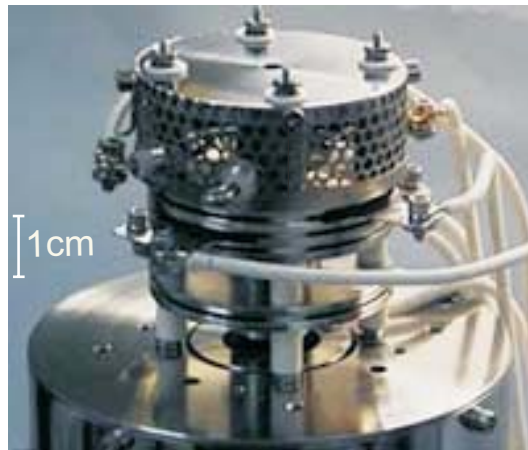
Figure 3.2: Electron impact ion source for the ionization of atomic or molecular beams and gaseous species. The ion source includes a small set of electrodes in the lower part for the extraction and focusing of the ions.

The ionizer can be used for ionization of atomic or molecular beams and gaseous species entering along the geometrical axis through the hole in the top plate or which are fed into the vacuum system, respectively, up to the ionizing region formed by a cylindrical grid. The cylindrical structure accelerates electrons towards the axis from four filaments surrounding the grid in the form of a square (see the technical drawings in App. A). The ionizing electrons are created by thermionic emission when applying an electric current through the filament. The electrons are accelerated into the ionization volume where they interact with the molecules to create ions. The ionization efficiency of the molecules present in the source ranges from 10^{-4} to 10^{-6} [55], taking into account the different ionization probabilities of the different species. The maximum cross-section for most molecules is at electron energies between 20 and 70 eV. This electron energy, usually fixed to 50 eV, is determined by the potential

difference between the ion volume and the repelling potential applied to the electron filaments.

3.1.3   Laser-induced ionization of carbon clusters

With this kind of ion source, carbon clusters $^{12}C_n^+$, $n = 1,2,3,..$, are extracted with high efficiency (see Fig. 3.3 (a)) from either a C_{60} target or a glassy carbon composite Sigradur™ target by laser induced desorption, fragmentation, and ionization. Typically a frequency doubled ($\lambda = 532\,\mathrm{nm}$) Nd:YAG laser is in use for that purpose. The big advantage of this source, when used as a reference for the magnetic field calibration in the mass measurement procedure, is the possibility to perform absolute mass measurements [56]. Furthermore, since the atomic mass unit u is defined as $1/12$ of the mass of ^{12}C, *i.e.*, any uncertainty of the reference mass is eliminated by definition. The only remaining source of uncertainty by the use of the clusters is due to the binding energy of the carbon atoms which is of the order of few eV. This error can be considered negligible for the level of accuracy reached at present with SHIPTRAP. Another important feature of carbon clusters is the large amount of reference masses available that allow to cover the full nuclear chart. Moreover reference masses are at most only six mass units away from the nuclide of interest, as illustrated in Fig. 3.3 (b). Thus, the systematic mass-dependent uncertainties that increase with the mass difference between the reference and the mass of interest are minimized along the whole nuclear chart. These features give the carbon-cluster ion source a natural advantage over alternative ion sources for mass calibration. In addition, clusters can be used to detect systematic errors and to determine the present limit of accuracy of a given mass spectrometer [41], as it has been recently performed at SHIPTRAP. Here, by means of cross-reference measurements between cluster ions of different size (84 u to 240 u), the mass-dependent uncertainty was found to be negligible but a systematic uncertainty of $4.5 \cdot 10^{-8}$ was revealed [57].

3.2   Production of radionuclides at GSI

The ion production methods that have been discussed so far deliver stable species that are taken either as a calibrant or simply as a source of ions to perform commissioning tests. The main topic of this thesis, however, deals with the study of short-lived radioactive species that are produced at Radioactive Ion Beam (RIB) facilities. Here, exotic nuclides are synthesized from various nuclear reactions with a projectile impinging on a target. The production mechanisms are classified according to the energy of the projectile in: transfer and charge-exchange reactions, deep-inelastic reactions, fusion-evaporation, fission, and fragmentation or spallation reactions. In all these processes, exotic nuclides of a wide range of masses are produced.

The two techniques employed to separate the ions of interest from the primary beam are the in-flight separation method, as *e.g.* at SHIP/GSI [58, 59] and the 'Isotope Separation On Line' (ISOL) method, as *e.g.* at ISOLDE/CERN [60]. In the latter the reaction products are thermalized in a high-temperature thick target and further diffused to the ion source, where they are ionized by one of the methods mentioned above, to finally be mass separated by bending magnets. On the other hand,
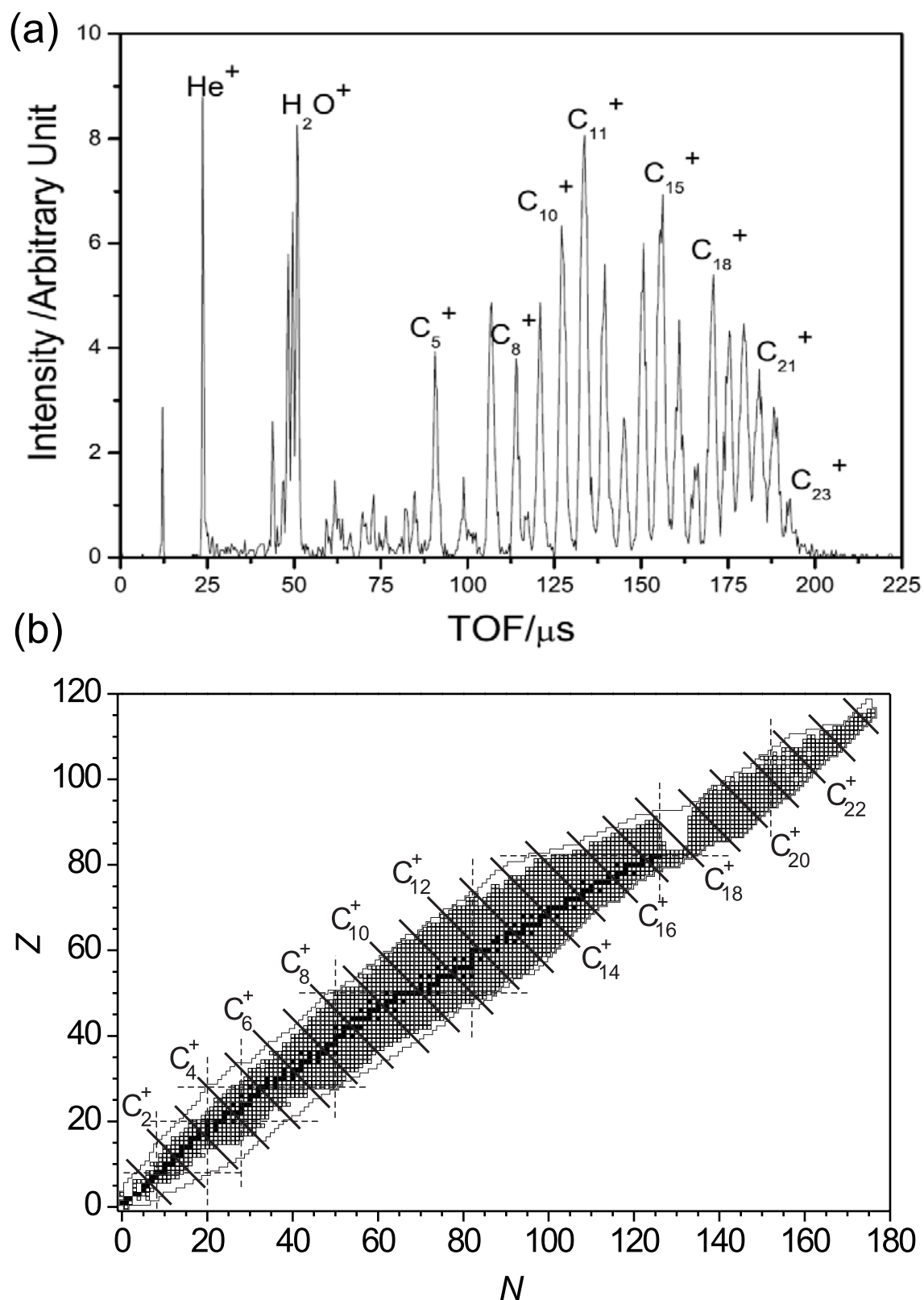
Figure 3.3: (a) Typical time-of-flight mass spectrum of singly-charged carbon-cluster ions and some contaminants produced in the laser induced ionization process of carbon composite Sigradur™. By the selection of the proper timing a certain cluster can be selected. (b) Nuclear chart with diagonal solid lines indicating the isobars of carbon clusters $^{12}\mathrm{C}_n^+$. Stable nuclides are indicated by black squares and shell closures by dashed lines.

the in-flight technique combines thin targets with heavy projectiles and uses strong focusing in the forward direction to transport the products that are separated from the first beam by means of magnetic and in some cases (charge independent velocity separation) also electric fields. The radioactive ion production and separation used at SHIP is based on the in-flight technique. Since the on-line mass measurements within this thesis have been performed at SHIPTRAP only the latter technique will be discussed in somewhat more detail.

3.2.1   The velocity filter SHIP

The Separator for Heavy Ion reaction Products (SHIP) is installed at the UNIversal Linear ACcelerator (UNILAC) at GSI, Darmstadt. It was designed for the synthesis and in-flight mass separation of heavy-ion induced reaction products [59]. It can provide transuranium species that are not available at ISOL- or fragmentation facilities elsewhere.
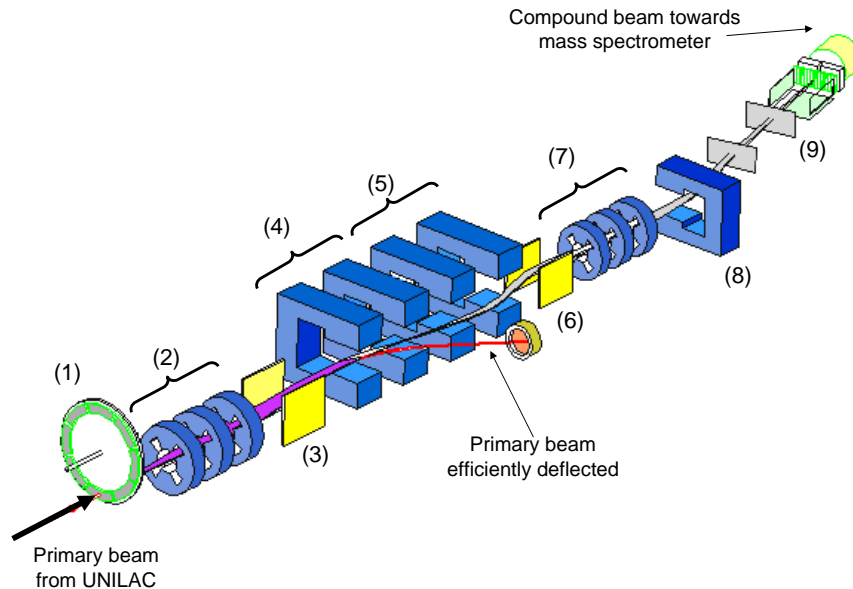
Figure 3.4: Layout of the SHIP velocity filter at GSI, Darmstadt. It is used for the production and in-flight separation of heavy and super-heavy species. The different components are (1) the rotatable target wheel, (2,7) magnetic quadrupole lenses for beam focusing, (3,6) electric dipoles, (4,5) pairs of magnetic dipoles, (8) last magnetic dipole, and (9) a detector setup for a time-of-flight measurement and the registration of the subsequent decays. The components (3,4) and (5,6) form the two-stage velocity filter. The overall length is 11 m [59].

The projectiles delivered by the UNILAC with energies of $5 - 7$ MeV/u, ranging from $A = 50$ to $A = 150$, impinge on a thin target of about 1 mg/cm^2 to undergo mainly fusion evaporation reactions. As a result a compound nucleus is formed that due to conservation of momentum, recoils from the target with a velocity lower than

that of the projectiles. The energy of the projectiles has to be sufficiently high to overcome the Coulomb barrier of the target nucleus, while the angular momenta of the recoils have to be small. Otherwise the centripetal force of the rotating nucleus would be larger than the binding nuclear force, making fission to be the dominant reaction.

Once the compound nuclei are produced, they are separated by a two-stage static velocity filter. Figure 3.4 illustrates the complete experimental setup of SHIP, which consist of a target, quadrupole lenses, the velocity filter, dipole magnets, and a set of detectors. The two-stage velocity filter consist of two electrostatic plates ((3) and (6)) and a set of four dipole magnets ((4) and (5)). This configuration allows to pass the filter without deflection only by those ions with the appropriate velocity, for which the electrostatic force is balanced by the Lorentz force. This method has been proven to be very efficient in the separation of the primary particles. It has allowed for the investigation of small cross-section reactions with low background rate, leading to the discovery of some of the heaviest elements from $Z = 107$ to 112 [8].

Chapter 4

Ion detection techniques

Several methods exist in order to monitor the ion presence in the trap. However, in this section we will understand ion detection as the technique used for the determination of the ions' eigenfrequencies, or combinations of them, whose knowledge will lead us to the atomic mass value. This technique is known as Ion Cyclotron Resonance (ICR) mass spectrometry and has the advantage, compared to other mass spectrometry techniques, of dealing with frequencies, which can be measured more accurately than any other experimental parameter, therefore, giving the most accurate atomic mass determination. For the frequency measurement of stored ions one has to distinguish between *destructive* and *non-destructive* detection techniques. While in the first case the ions get lost after being detected and a new loading of the trap is required, in the second case the ions stay stored during the detection process and several detection cycles can be performed with the same trap content. In addition, the ions can be transfered to other setups for further experiments.

Two detection methods are currently used for high-precision ICR mass spectrometry: (1) a destructive method based on the excitation of the ion motions by an external rf field prior to the ejection towards a detector and measurement of the time of flight (TOF) spent from the trap to the detector and (2) a non-destructive detection method based on broad-/ narrow-band Fourier Transform (FT) of the image currents induced in the trap electrodes by the oscillating motion of the ions.

For mass spectrometry on very short-lived radionuclides ($T_{1/2} < 1$ s) with sufficient production rates (> 100 ions/s) the destructive detection method is well suited since the nuclei will anyhow decay in a short period, leaving few chances for the use of a non-destructive detection. However, for long-lived radionuclides ($T_{1/2} \geq 1$ min) with low production rates, as the heavy and super-heavy species, the non-destructive detection is the most advantageous as it will be pointed out in the course of this chapter.

4.1   Destructive time of flight-ICR detection

This technique exploits the interaction of the magnetic moment $\vec{\mu}$ of the stored ions with the gradient $\vec{\nabla}\vec{B}$ of the magnetic field they experience when ejected from the trap [61]. By means of this interaction the free cyclotron frequency ω_c of the ions under investigation can be accessed in the following way:

The ions are first prepared in a well defined pure magnetron motion by means of a dipolar excitation ($\rho_-(0)$, $\rho_+(0) = 0$) [42]. Since the radial energy of the stored
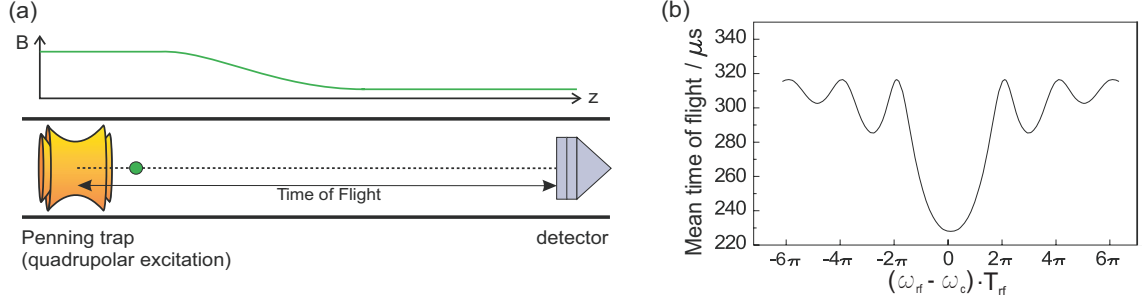
Figure 4.1: (a) Illustration of the time-of-flight ion cyclotron resonance detection. In the top the magnetic field gradient along the ion path towards the detector is shown. (b) Theoretical line shape of a TOF resonance where the time of flight is represented as a function of the frequency detuning. The curve has its minimum for $\omega_{\mathrm{rf}} = \omega_c$. The typical side-band structure is due to the rectangular pulse of finite duration used for the quadrupolar excitation.

ions is mainly dominated by the cyclotron frequency, as it becomes obvious from Eq. (2.25), the ions will have a small radial kinetic energy E_r and therefore a small magnetic moment $\vec{\mu}$ associated as given by:

$$\vec{\mu} = \frac{E_r}{B} \hat{z}. \tag{4.1}$$

If at this point the ions are excited by a quadrupolar field at a frequency ω_{rf} close to their free cyclotron frequency, a periodic conversion will occur between magnetron and cyclotron motions (see Section 2.4.2) being only complete, *i.e.*, $\rho_-(T_{\mathrm{conv}}) = 0$ and $\rho_+(T_{\mathrm{conv}}) = \rho_-(0)$, for those ions irradiated with $\omega_{\mathrm{rf}} = \omega_c$. After excitation, the ions are ejected from the trap, by lowering the endcap potential, towards the detector and through the gradient of the magnetic field, as illustrated in Fig. 4.1 (a). The interaction of the magnetic moment with the gradient of the magnetic field causes the ions to experience an axial force

$$\vec{F} = -\vec{\mu} \cdot \vec{\nabla} \vec{B} = -\frac{E_r}{B} \frac{\partial B}{\partial z} \hat{z}, \tag{4.2}$$

that leads to a maximum reduction in the time of flight from the trap to the detector for the ions excited under resonance condition, *i.e.* at $\omega_{\mathrm{rf}} = \omega_c$. Thus, the resonant quadrupole excitation gives a maximal gain in the magnetic moment, that produces the strongest axial force resulting in the shortest time of flight. The total time of flight from the trap center $z = 0$ to the detector $z = z_1$ for a given radial energy E_r can be calculated by [62]

$$T_{tot}(\omega_{\mathrm{rf}}) = \int_0^{z_1} \sqrt{\frac{m}{2\left(E_0 - qU(z) - \mu(\omega_{\mathrm{rf}})B(z)\right)}} dz, \tag{4.3}$$

where E_0 is the initial radial kinetic energy of the ion, and U_z and B_z the electric and magnetic fields along the ion path to the detector. Thus, a scan of the quadrupolar excitation ω_{rf} produces a characteristic time-of-flight resonance. The theoretically expected line shape of such a resonance is determined by the Fourier transformation

of the rectangular time excitation profile[1] and is found to be similar to the absolute value of the so-called sinc-function $f(x) = \sin(\alpha x)/\alpha x$ (see Fig. 4.1 (b)) [62]. At this point, a series of concepts that will be very useful to characterize the quality of the mass measurements in both detection methods considered in this work will be presented.

If we take the module of the first derivative of Eq. (2.5) with respect to the mass m and replace the differentials by increments, the resulting identity is used to define the resolving power

$$\Re = \frac{\omega_c}{\Delta\omega_c} = \frac{m}{\Delta m}, \tag{4.4}$$

in the frequency or mass domain, respectively. The inverse value of the resolving power $\Re^{-1}$ is known as the mass resolution and gives information about the ability of a mass measurement of being distinguished between two values very close to each other, *i.e.*, it is a measure of the width of the spectral feature associated with the detection technique. On the other hand, the uncertainty of a mass measurement δm is how well the centroid of the spectral feature can be found. The uncertainty of a mass measurement is usually better than the resolution. It is limited by statistics, signal to noise, and the knowledge of the peak shape.

Coming back to the case of the TOF-ICR technique, the resolving power is given by

$$\Re = \frac{\omega_c}{\Delta\omega_c} \equiv \frac{\nu_c}{\Delta\nu_{\mathrm{FWHM}}}, \tag{4.5}$$

where the line width $\Delta\nu_{\mathrm{FWHM}}$ of the central peak in Fig. 4.1(b) can be obtained from a Taylor expansion of Eq. (2.26) and a time-of-flight analysis, and is found to be [62]

$$\delta\nu_{\mathrm{FWHM}} \approx \frac{1}{T_{\mathrm{rf}}}, \tag{4.6}$$

that transforms the expression of the resolving power into

$$\Re \approx \nu_c \cdot T_{\mathrm{rf}}. \tag{4.7}$$

Thus, the resolving power could be selected beforehand depending upon the duration of the quadrupolar excitation, but in practice the lifetime of the radionuclides and the pressure conditions are the limiting factors in the achievable mass resolution. The relative precision with which the cyclotron frequency can be determined is in first order proportional to the resolution and to the number of ions N detected in the frequency scan

$$\frac{\delta\nu_c}{\nu_c} \propto \frac{1}{\Re\sqrt{N}} \ . \tag{4.8}$$

An important quantity to characterize the quality of the resonance is the *contrast*[2] C that is defined as [65]

$$C = \frac{t_{off} - t_{in}}{\sqrt{\sigma_{off}^2 + \sigma_{in}^2}}, \tag{4.9}$$

---

[1] A different excitation profile, known as Ramsey excitation, based on the interruption of the normal excitation pulse by waiting periods, has proven in on-line measurements at ISOLTRAP to reduce the FWHM of the resonance curve, enabling a better determination of the center frequency and thus reducing the mass uncertainty up to a factor of 3 [63, 64]

[2] sometimes also referred to in literature with the name of signal-to-noise (S/N) ratio.
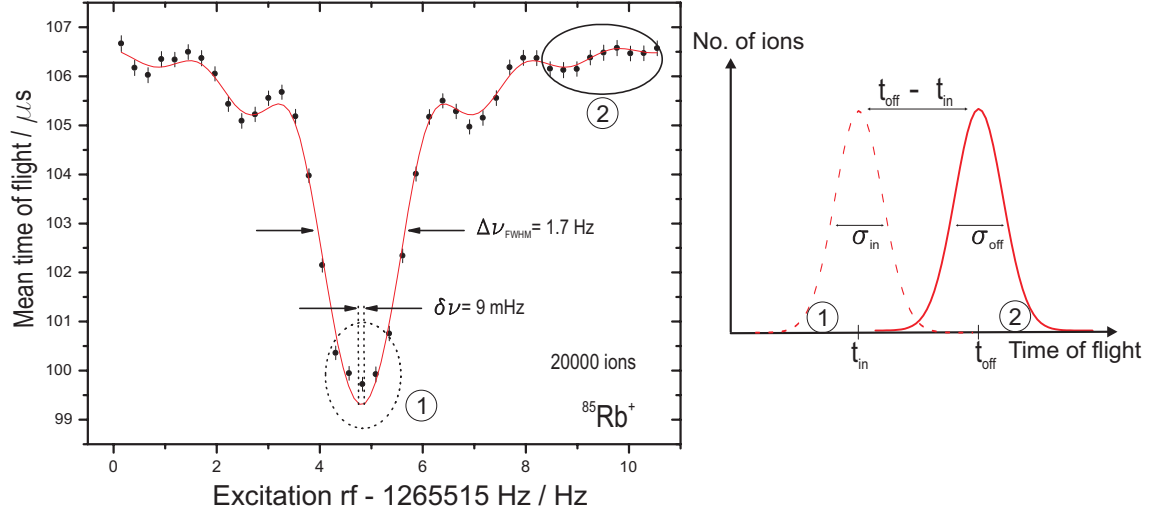
Figure 4.2: (left) Cyclotron resonance of ^{85}Rb$^+$. The quadrupolar excitation was applied for $T_{\mathrm{ex}} = 600$ ms that corresponds to a resonance width $\Delta\nu_{\mathrm{FWHM}} = 1.7$ Hz, which results in a resolving power $\Re = 7 \cdot 10^5$. The error of the centroid is determined by a least-square fit with a standard deviation of 9 mHz that leads to a relative precision $\delta\nu/\nu = 7 \cdot 10^{-9}$. (right) Definition of the contrast C using the regions marked as 1 and 2 of the rubidium cyclotron resonance.

where t_{in} and t_{off} indicate the time of flight of the ions excited resonantly (*in* resonance) or non-resonantly (*off* resonace) by the quadrupolar rf-field, respectively, and σ_{in} and σ_{off} are the associated uncertainties to those distributions (see Fig. 4.2). Then, the value of the contrast C for a given resonance describes how well the non-resonantly excited ions are separated from the resonantly excited ones with respect to their time of flight. Thus, the value of C is related with the precision with which the cyclotron frequency can be determined for a given number of ions N. In fact, the uncertainty in the cyclotron frequency determination $\delta\nu_c$ given by Eq. (4.8) assumes that the shape of the resonance curve can be approximated by the one of a Gaussian distribution of data points. In a Gaussian distribution the uncertainty of the centroid (expected value) is given by the standard deviation over the square root of the number of ions. However, the cyclotron frequency ν_c is taken from a least-square fit of the theoretically expected curve (see Fig. 4.1 (b)) to the data points. Consequently, Eq. (4.8) has to be rewritten as

$$\delta\nu_c = a\frac{\Delta\nu_{\mathrm{FWHM}}}{\sqrt{N}} = a\frac{\nu_c}{\Re\sqrt{N}} \ , \qquad (4.10)$$

where the proportionality constant a accounts for the difference between the uncertainty associated with the least-square method and the one with the Gaussian theory. Therefore its size depends on the contrast and on how the ions are distributed over the scanning frequencies [66]. A high contrast results in a low a and means that a smaller mass uncertainty can be reached with the same number of ions when those are properly located on the resonance. Or the other way around, a minimum number of ions is needed when the contrast is high. This is especially important for nuclides with low production rates where the measurement time becomes very
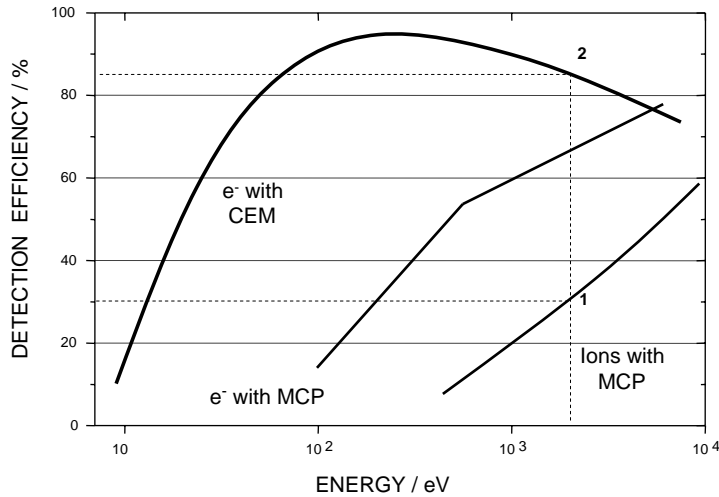
Figure 4.3: Detection efficiency of a microchannel plate (MCP) and a channel electron multiplier (CEM) detector as a function of the energy and the particle detected. The dashed lines show the present detection efficiency numbered as 1. Number 2 indicates the detection efficiency that will be reached with the use of the CEM.

long. Here, fluctuations of the magnetic field or damping with the rest gas make the mass measurement difficult, or in some cases even impossible. Due to damping the contrast of a cyclotron resonance is reduced for long excitation times and the resolving power $\Re$ increases less than linearly with T_{rf}. The way of improving the contrast is increasing the depth of the resonance or decreasing the width of the time-of-flight distributions. The depth depends mainly on the radial energy of the ions, which is determined by the amplitude of the magnetron excitation. The widths of the time-of-flight distributions are determined mainly by the axial energy distribution and the ejection of the ion cloud from the center of the trap to the detector. An optimization of this features and therefore of the contrast can be carried out by a position-sensitive MCP detector (see Chap. 8), which is used to monitor the position of the ions inside the trap in their magnetron orbit and to study the axial energy distribution. An optimized extraction scheme to guarantee a resonance with high contrast with the mass spectrometer SHIPTRAP can be found in [65].

4.1.1 Charged particles detectors

The time-of-flight determination is always associated with the use of a particle detector. To this end, microchannel plate (MCP) detectors have been almost exclusively used for mass spectrometry on radionuclides since they are extremely reliable which is of major importance during on-line experiments. The problem of MCP detectors is that they exhibit a very low efficiency for low-energy ion beams as it is, *e.g.*, the case at the mass spectrometer SHIPTRAP, where the ions reach the detector with an energy around 2 to 3 keV. The MCP detects these ions with an efficiency of only 30% (indicated in Fig. 4.3 with the number 1). In Chapter 7 a study of the relative

detection efficiency of the MCP and another kind of particle detector known as chan-
nel electron multipliers (CEM) will be presented. It will be shown that with the use
of the later one the overall experimental efficiency can be improved up to a factor
of 3 (indicated in Fig. 4.3 with the number 2), decreasing consequently the mass
uncertainty and giving access to the investigation of species with lower production
rates.

In the following only the theoretical basis and technical features of the MCP
and CEM will be presented. A later discussion will focus on their experimental
performance and the already mentioned efficiency comparison. Both detectors are
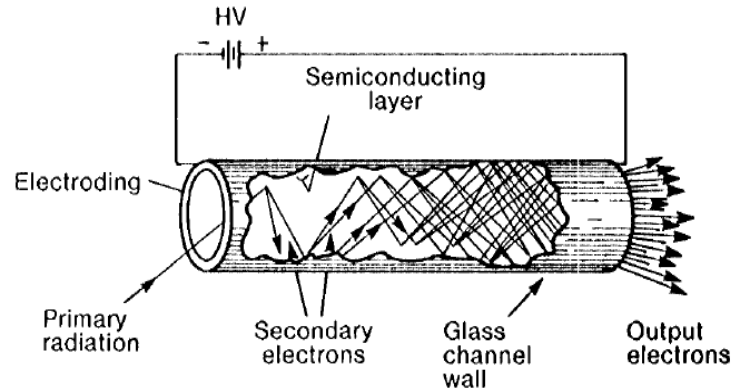
Figure 4.4: Cutaway view of a secondary electron multiplier when a voltage
difference is applied across the two sides of the channel [67].

based on secondary electron multipliers (SEMs) in which the signal is originated by
the successive multiplication of the secondary electrons produced by the collision of
an ion on the emissive coated surface of a lead silicate glass. Figure 4.4 illustrates
the process of electron multiplication through the walls of a coated channel when
a voltage difference is applied across the input- and output-sides of the channel.

Microchannel Plate detector
A microchannel plate is a specially fabricated plate of 0.4 to 3 mm thickness, that am-
plifies electron signals similar to a SEM, see Fig. 4.4. It consists of a two-dimensional
periodic array of very-small glas capillaries (channels), $5 - 15$ μm in diameter, fused
together forming a honeycomb structure as illustrated in Fig. 4.5. Unlike a SEM, the
MCP has several million independent channels, up to one million per cm^2 and each
channel works as an independent electron multiplier. In other words, one can imag-
ine the MCP as an assembly of millions miniature SEMs with a given bias angle.
The channel bias angle is the angle formed by the channel axis and the vertical axis
to the plate surface. Channels are tilted to prevent incident particles from passing
through the channels without striking the walls. The optimum angle is between $5°$
and $15°$.

A single incident particle (ion, electron, photon, etc.) enters a channel and emits
an electron from the specially coated channel wall. Secondary electrons are accel-
erated by the electric field due to a voltage difference of about 1100 V across both
ends of the MCP. They travel along their parabolic trajectories until they strike the
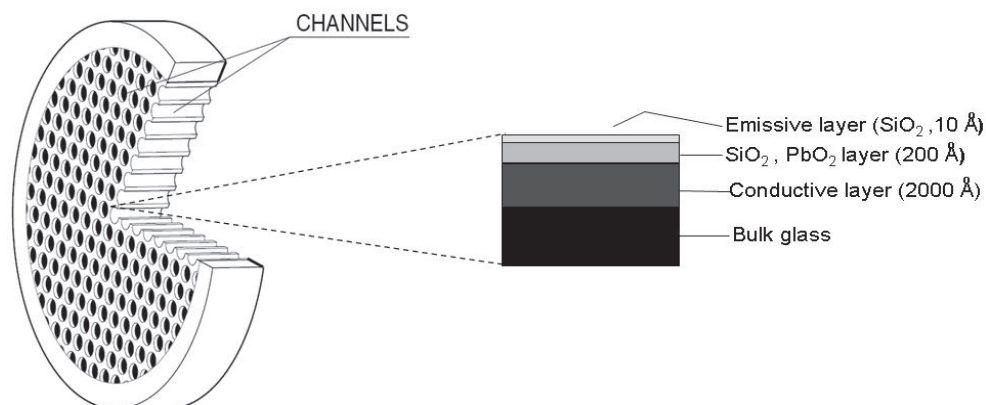
Figure 4.5: Sketch of a MCP detector with its honeycomb channel structure. A zoom into the coating reveals the different layers with their composition and thickness.

channel surface, thus producing more secondary electrons. As a result, this cascade process yields a cloud of $10^3 - 10^4$ electrons, which emerge from the rear of the plate and are collected on a metallic anode.

Microchannel plates have a combination of unique properties like high gain and high spatial and temporal resolution that make them suitable for a large variety of applications. For time-of-flight mass spectrometry a high temporal resolution is required from the MCP. The gain can be increased by assembling two (V-stack or Chevron configuration) or three (Z-stack) plates together adjacent to one another and with their bias angles rotated by 180° with respect to each other. To this end, in our setup the Chevron configuration is used[3]. Here, a single input event generates a pulse of about 10^7 electrons at the output with a pulse width of ~ 2 ns (see Tab. 4.1).

Channel Electron Multiplier detector

A channel electron multiplier, also known as Channeltron [67], is a single horn-shaped SEM structure having an inner diameter of approximately 1 mm and an outer diameter of 2-6 mm, see Fig. 4.6. The effective detection area is given by the diameter of the entrance horn and is in the order of 1-2 cm^2. The secondary electron multiplication is produced when an incoming particle (ion, electron, photon, etc.) impinges on the horn surface. The avalanche of electrons is accelerated down the channel by a positive bias of 1.8-2 kV and a pulse of typically 10^7 electrons is collected in the anode. See Tab. 4.1 for further specifications.

It has been proven that CEM detectors are more efficient than MCPs for the typical ion energies used at SHIPTRAP (see Chap. 7) and ISOLTRAP [68]. However, the time resolution of the CEM is around 10 times less than for a MCP. In order to avoid losses by the intrinsic dead time[4] the count rate has to be limited to $\leq 10^5$Hz.

---

[3]The MCP detector used in our setup are not only for the TOF detection but also for the ion transport monitoring along the beam line.

[4]The dead time is the time the detector employs in processing an event. Within this time a new
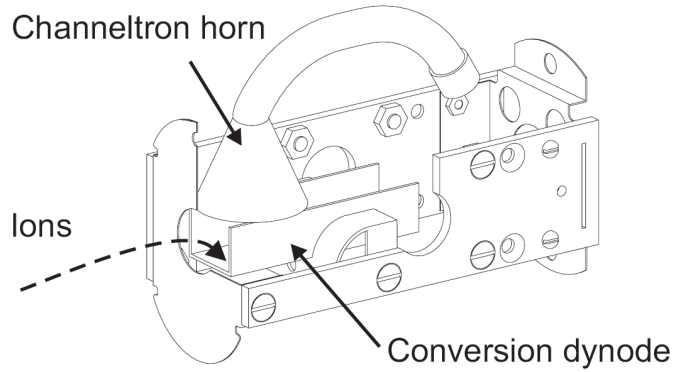
Figure 4.6:   Illustration of a CEM detector with a conversion dynode for the detection improvement of low energetic particles or heavy ion beams.

This does not imply any disadvantage concerning its use in high-precision mass spectrometry, since the aim is to perform single ion experiments. It is well known that the detection efficiency in a SEM decreases nearly exponentially with increasing mass [67] or more correctly that the secondary emission efficiency depends on the velocity of the impinging particle. To this end, as illustrated in Fig. 4.6, the CEM detector has incorporated a conversion dynode that enhances the detection sensitivity in case of heavy or low energy ion beams. The conversion dynode is simply a metal surface, which can be held at a high voltage (*e.g.* 3 to 20 kV). The dynode potential serves to accelerate the ions to a point where good conversion efficiency (to either electrons or secondary ions, depending on the charge of the detected particles) occurs.   The
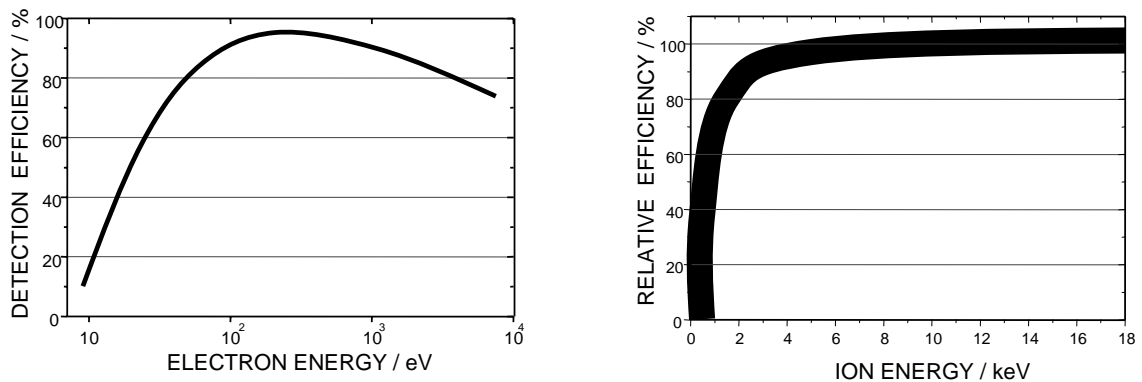
Figure 4.7:   CEM detection efficiency as a function of the energy of the incoming electrons (left) and ions (right) [67].

CEM is then used to detect the emission from the dynode surface. The high negative potential on the dynode serves to guide electrons towards the CEM input, which is held at a lower negative potential. The energy of the outgoing electrons is given

_____

incoming signal is not seen by the detector.

Table 4.1: Technical specifications of the two different detectors used for ion detection within this work.

	MCP V-STACK	CEM
Model	Topag-MA 34	DeTech 402A-H
Effective Diameter	25 mm	11.2 mm
Channel Diameter	$10\,\mu\mathrm{m}$	1 mm
Gain	$10^6 - 10^7$	$5 \cdot 10^7$
Resistance	320 MΩ	130 MΩ
Dark Counts	< 3 cps/cm^2	< 0.05 cps/cm^2
Pulse Width	< 1 ns	18-20 ns

by the difference between the potential applied to the dynode and the CEM. This energy can be selected in order to match the ion beam characteristics and to increase consequently its detection efficiency. Figure 4.7 shows the detection efficiency of the CEM detectors as a function of the energy of the detected ions or electrons.

4.2 Non-destructive Fourier transform-ICR detection

The FT-ICR detection method enables different measurement cycles to be performed with the same trap content since the measurement process does not imply the loss of the ion, as it is the case for the TOF-ICR technique. The great advantage of this non-destructive detection is that species with low production rate, like the transuranium elements, can be investigated as long as their storage time and half-life is long enough. Hence, first direct mass measurements on these species will become feasible (see Chap. 7)

The FT-ICR technique is based on the measurement of the motional eigenfrequencies by the detection of the induced image currents, as conceived by W. Shockley [69], on two opposite trap electrodes. In particular, in our setup the induced current of the circulating ion in its cyclotron motion with frequency ω_+ is picked up on two opposite segments of the four-fold segmented ring electrode (see Fig. 4.9). The detection of the cyclotron frequency requires the cyclotron radius r_+ to be large enough to induce a measurable image charge on the detection electrodes. To this end, an azimuthal dipolar excitation (see Sec. 2.4.1) has to be applied prior to the detection of the induced image currents.

The current induced on an arbitrary electrode arrangement by an ion of charge q moving with velocity $\vec{v}$ is related by means of the electrostatic reciprocity principle[5] to the absorbed power from an electric field $\vec{E}$, which is generated by a voltage U applied to a pair of electrodes perpendicular to the ion motion. Thus, the current

---

[5]Namely, that "the charge induced on an electrode by a unit point charge is equal in magnitude to the potential that would be produced at that same ion position, in the absence of the ion, when a unit potential is applied to the conductive electrode" [70].
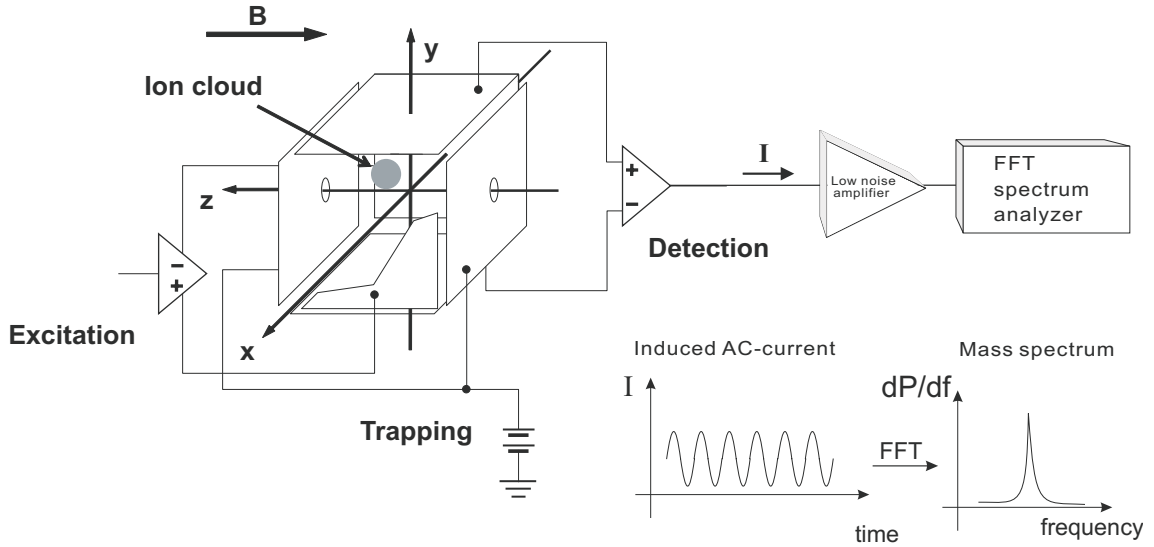
Figure 4.8: Illustration of a rectangular Penning trap and its electronic circuitry for a broad-band, non-destructive Fourier-transform mass spectrometer using induced cyclotron resonance detection of the eigenfrequencies. The two perpendicular plates are used for axial confinement while the parallel ones are used for resonance excitation and detection. The induced AC-current in the detection plates is converted to a frequency spectrum by Fourier transformation [4].

supplied by an external circuit connected to the plates is given by

$$i = \frac{P}{U} = \frac{q\vec{v}\vec{E}}{U}.$$ (4.11)

Exchange of the external circuit by an ohmic resistor leads to an energy dissipation from the system across the resistor and after application of the reciprocity principle Eq. (4.11) becomes equivalent to the induced image current of an ion on two opposite electrodes [70]. A different derivation of the induced current is given in [71] based on a signal model consisting of a rotating electric monopole. When the dipolar detection electrode arrangement is approximated by two parallel plates [72], Eq. (4.11) becomes

$$i = q\frac{2\pi\nu_{ion}r_{ion}(t)}{d} \ ,$$ (4.12)

where ν_{ion} is the frequency of the detected ion motion, $r_{ion}(t)$ the projection of the radius perpendicular to the electrodes , and d the distance between the two electrodes. The broad-band FT-ICR mass spectrometry is widely practiced in analytical chemistry since its invention by M. B. Comisarow and A. G. Marshall in 1974 [73, 74]. In these experiments an ion cloud with a large number of ions (typically $10^3 - 10^6$ charges) induces an oscillating image charge on two opposing electrodes. A frequency spectrum is obtained by Fourier transformation of the digitized time-domain ICR signal. The rectangular Penning trap configuration (see Fig. 4.8) is commonly used because of its easy construction for large volumes, and its performance for those interested in measuring masses over a broad mass range [75] with typical resolving powers of several millions. The main problem of applying this non-destructive detection technique to high-precision mass determination of radionuclides is the large
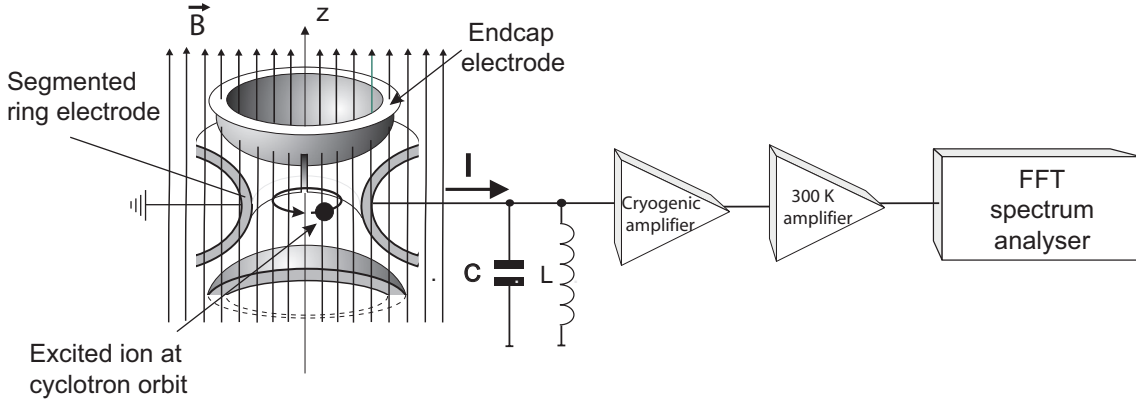
Figure 4.9: Detection scheme for the non-destructive FT-ICR detection technique. Due to a tuned resonance circuit with a high quality factor Q an increased detection sensitivity is reached in a narrow-band range. An amplification of the signal must be performed prior to the digital processing by a FFT analyzer.

number of ions required to have a measurable signal, which is limited to a minimum of approximately 200 ions stored simultaneously in a room temperature setup [76].

In this section a significant improvement of the detection sensitivity by adding a specific inductance L between the ion trap and the amplifier (see Fig. 4.9) that together with the intrinsic capacitance C of the trap and cables forms a parallel resonance LC circuit will be presented. With this new approach the current signal induced in the electrodes is not analyzed directly any longer but converted into a detectable voltage signal by means of the resonance circuit. The use of a cryogenic narrow-band detection, achieved by the tuned resonance circuit at 4-K temperature with the addition of some other requirements in the setup (see Chap. 7) will enable single ion sensitivity and therefore a first approach of FT-ICR mass spectrometry to the investigation of radionuclides will be possible [77]. For the hyperbolically shaped segments of the ring electrode, the distance d in Eq. (4.12), is modified by a geometric factor [78] that leads to an effective distance D. Considering this geometric factor and taking the rms value, Eq. (4.12) leads to

$$I_{\text{eff}} = \sqrt{2}\pi\frac{r_{ion}}{D}q\nu_{ion}\,, \qquad (4.13)$$

being now r_{ion} the ion motion amplitude.

Unlike the broad-band detection mentioned above, in a narrow-band detection setup the voltage signal produced by a tuned circuit (see Fig. 4.9) is analyzed. The resonance frequency of the tuned circuit has to match the frequency of the ion motion in order to take advantage of the high resistance peak exhibited under resonance, which will be found later to be given by $R = Q/\omega C$. Rather than using a simple ohmic resistor R, the detection sensitivity is improved by a tuned circuit with a frequency dependent impedance $Z(\nu)$. The need of a high quality factor (Q-value) is based on the expected image current of a single singly-charged ion at a relative radius of $r_{ion}/D = 0.4$ and a cyclotron frequency of $\nu_+ = 430$ kHz for $A = 250$ under normal experimental settings at SHIPTRAP ($B = 7$ T) which is about $I_{\text{eff}} = 0.12$ pA. With the value of R in resonance, the voltage rms-value needed for the

estimation of the signal-to-noise ratio (S/N) can be easily deduced from Ohm's law as

$$U_S = R \cdot I_{\text{eff}} = \frac{1}{\sqrt{2}} \frac{r_{\text{ion}}}{D} q \frac{Q}{C} \ . \tag{4.14}$$

The thermal noise (or Johnson's noise) of the detection system is given by

$$U_N = \sqrt{4k_B T R \Delta \nu} \ , \tag{4.15}$$

where k_B is the Boltzmann constant, T the temperature of the detection system, R the resistance in resonance of the tuned circuit, and $\Delta \nu$ is the spectral band width. Ideally, this is equivalent to the width of the ion signal, which is given by the inhomogeneity of the magnetic field $\Delta B / B = \Delta \nu / \nu$. The signal-to-noise ratio is given finally by

$$\frac{U_S}{U_N} = \frac{\sqrt{\pi}}{2} \cdot \frac{r_{\text{ion}}}{D} \cdot q \cdot \sqrt{\frac{\nu}{\Delta \nu}} \cdot \sqrt{\frac{Q}{k_B T C}}, \tag{4.16}$$

where the frequency ν denotes the frequency of the tuned circuit, since it has to match the frequency of the ion ν_{ion} during detection. Equation (4.16) reveals that in order to reach a good signal-to-noise ratio for the detection of a single singly-charged ion, a low temperature and small detection band width as well as a high Q-value of the tuned circuit are desirable. The value of the radius r_{ion} is limited by the maximal tolerable inhomogeneities and imperfections of the electromagnetic fields observed when moving off-axis of the trap (see Sec. 2.3). A complete study of the optimum parameters for the realization of a high-sensitive narrow-band FT detection setup for the mass spectrometer SHIPTRAP and a description of the design can be found in [77]. Chapter 7 of this work will report on the commissioning and first off-line tests of this setup.

Analogous to the TOF-ICR detection, the resolving power $\Re$ for the FT-ICR detection is given as

$$\Re \approx \nu_+ \cdot T_s \,, \tag{4.17}$$

and again the resolution is determined by the same Fourier limit, except that now it is the sampling time T_s rather than the excitation time that is relevant. The sampling time corresponds to the length of the transient recording or to the time while the induced current is being detected. In any case, the low cyclotron frequencies of the heavy and super-heavy species as well as the indirect influence of collisions with the fraction of the buffer gas transmitted through the pumping barrier connecting both traps (see Chap. 7) will constrain the value of $\Re$.

4.2.1   Narrow-band detection using a tuned circuit

The use of a tuned circuit prior to the Fast-Fourier-Transformation (FFT) analysis has been already justified as a necessary step to increase the detection sensitivity to a single singly-charged ion; a mandatory requirement for the investigation of super-heavy (SHE) species. A (FFT) of the time-dependent voltage signal originated by the use of the tuned circuit will result in the frequency of the ion. An inductance connected in parallel to two opposite segments of the ring electrode, from where the ion signal is picked up, together with the intrinsic capacitance of the elements forming the detection system, creates a parallel LC circuit that is used to convert
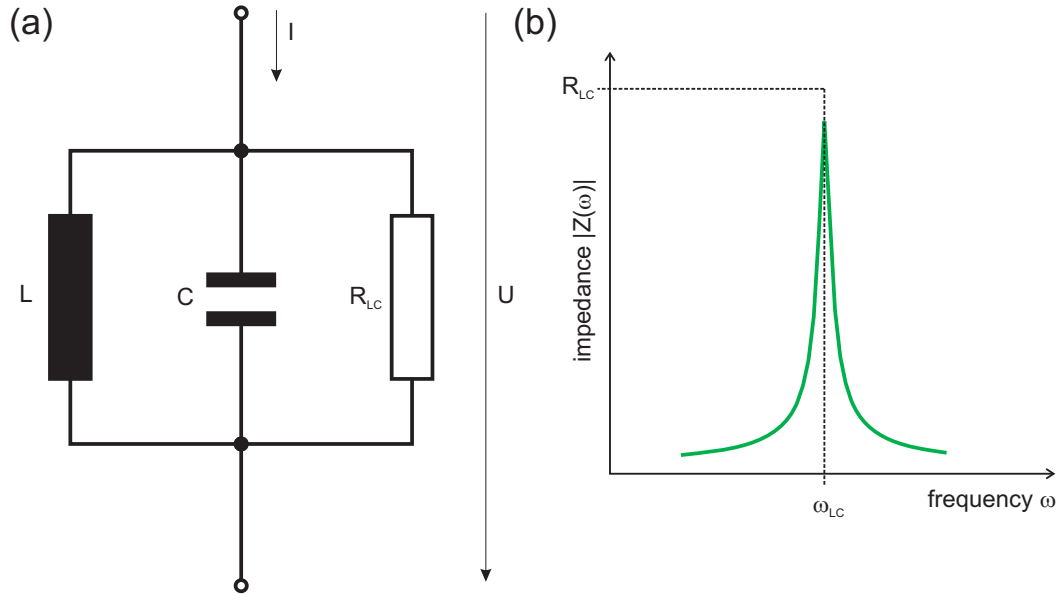
Figure 4.10: (a) Equivalent parallel LC-circuit including dissipative effects. The addition of an ohmic resistor in parallel accounts for the losses in the LC circuit components. (b) In resonance, the impedance of the parallel LC circuit is given by R_{LC}. In the ideal case, *i.e.* no loss mechanisms, the impedance for the resonance frequency ω_{LC} would be infinite.

the induced current into a voltage signal. The sensitivity enhancement of the detection system is due to the high resistance shown by the LC circuit in resonance. A small current signal is converted into a voltage drop, more convenient for being measured. The narrow band width implies that the impedance $Z(\omega)$ of the LC circuit is frequency dependent and has a very narrow maximum around its center frequency ω_{LC}. The width $\Delta\omega$ is an indication of how precise the tuned circuit is for a given frequency and it is a measure of the quality factor Q of the circuit, which is defined as

$$Q = \frac{\omega_{\mathrm{LC}}}{\Delta\omega} \ . \tag{4.18}$$

The broad band detection has been a very important tool for mass spectrometry, mostly for chemistry purposes, in the simultaneous investigation of a wide range of masses since the number of ions is large enough to produce a measurable induced image current and thus a suitable S/N ratio. For the narrow band detection method, the detectable mass range has to be sacrificed for an acceptable S/N ratio due to the detection of a single ion.

There exist two principle types of tuned circuits: the parallel and the serial circuit. Only the first will be considered since it is the one that shows a maximum of resistance in resonance. An inductance L and a capacitance C are placed in parallel to each other. Considering ideal components, the resulting impedance of the circuit is described by

$$Z_{\mathrm{LC}}(\omega) = i(\omega C - \frac{1}{\omega L})^{-1} \ . \tag{4.19}$$

In practice, one has to consider the dissipative effects taking place in the single

components [78], which can altogether be modeled by the addition of a parallel resistance. Thus, the real parallel tuned circuit is equivalent to two ideal components and one parallel ohmic resistor R_{LC} (see Fig. 4.10 (a)). Consequently, the real impedance of the tuned circuit is described by [79]

$$Z_{\mathrm{LC}}(\omega) = \frac{1}{\frac{1}{R_{\mathrm{LC}}} - i(\omega C - \frac{1}{\omega L})} \, . \tag{4.20}$$

The absolute value $|Z_{\mathrm{LC}}(\omega)| \equiv |Z(\omega)|$ is plotted as a function of the frequency ω in Fig. 4.10 (b). In resonance, the impedance has a maximum given by the resistance R_{LC}. The resonance frequency[6] ω_{LC} is determined via Thomson's formula

$$\omega_{\mathrm{LC}} = \frac{1}{\sqrt{LC}} \, . \tag{4.21}$$

As shown in Eq. (4.18), the quality factor Q is defined by means of the width $\Delta\omega$ which corresponds to the width in which the amplitude of the voltage across the parallel LC circuit drops to $1/\sqrt{2}$ of its maximum value. Assuming a constant current amplitude across the circuit, the last statement has to hold also for the impedance. Thus,

$$\left| \frac{Z(\omega)}{Z(\omega_{\mathrm{LC}})} \right| = \frac{1}{R_{\mathrm{LC}} \sqrt{\frac{1}{R_{\mathrm{LC}}^2} + (\omega C - \frac{1}{\omega L})^2}} = \frac{1}{\sqrt{2}}$$

$$\Rightarrow \frac{1}{R_{\mathrm{LC}}^2} = \left(\omega C - \frac{1}{\omega L} \right)^2 \, .$$

A Taylor expansion of second order with center in $\omega = \omega_{\mathrm{LC}}$ gives as a result

$$\frac{1}{R_{\mathrm{LC}}} \approx 2C \left(\omega - \omega_{\mathrm{LC}} \right) \, . \tag{4.22}$$

Since $\omega - \omega_{\mathrm{LC}}$ is by definition of the Q-value $\Delta\omega/2$, Eq. 4.22 results in

$$\Delta\omega \approx \frac{1}{R_{\mathrm{LC}} C} \, . \tag{4.23}$$

Finally, the Q-value of the real LC circuit, modeled by a parallel resistance R_{LC}, can be written as

$$Q = \omega_{\mathrm{LC}} C R_{\mathrm{LC}} = \frac{R_{\mathrm{LC}}}{\omega_{\mathrm{LC}} L} . \tag{4.24}$$

---

[6]The well-known effect of a damped circuit on the shift of its resonance frequency is neglected here since the damping factor of the detection system is very small ($Q \approx 10^3$) and the systematic error of the frequency determination will be always larger by orders of magnitude.

Part II

Experiment

Chapter 5

The SHIPTRAP facility

The SHIPTRAP facility [80, 81], located at GSI, represents a link between the velocity filter SHIP (see Sec. 3.2.1) and a double Penning trap mass spectrometer (see Fig. 5.1). A particular benefit of this association is the possibility to investigate transuranium species not accessible at ISOL- or fragmentation facilities [82]. The reaction products from SHIP with energies of a few 100 keV are first stopped in a buffer-gas filled stopping cell. The ions are extracted from the gas cell by a combination of DC and RF electric fields and swept out through a nozzle in a supersonic gas jet. Subsequently, the ions are precooled in the extraction radiofrequency quadrupole (RFQ) operated as an ion guide before they are transferred to a RFQ ion-beam cooler and buncher. Here, the ions are cooled within few milliseconds and extracted as a low-emittance bunched beam, which eases an efficient injection into the Penning trap system, consisting of two cylindrical traps in a superconducting 7-T magnet. The first trap is used for isobaric selection and the second for the high-precision mass determination by means of the TOF-ICR technique. In this chapter the characteristics of each part of the setup and the mass measurement procedure using the TOF-ICR are described.

5.1   The gas cell

The gas stopping cell [83] is designed to accept the beam of fusion-evaporation products from SHIP with the transversal dimensions of 50×30 mm^2. Figure 5.2 illustrates the gas stopping cell used in the SHIPTRAP setup. The ions enter through a few μm thin window foil, where the main energy loss occurs. They are further decelerated and finally thermalized by collisions with the He buffer gas. The pressure, typically around 50 mbar, and the thickness of the window foil have to be selected very carefully to ensure an efficient stopping inside the cell. The optimum values of pressure and foil thickness depend strongly on the absolute energy and the energy spread of the SHIP beam, which is mainly determined by the type of projectile and target in the fusion-evaporation reaction but also by the primary beam energy. For every new experiment the window foil and the pressure have to be chosen and optimized individually. For a more detailed discussion on the selection of those parameters see [65].

An important limitation in the performance of the gas cell is due to the presence of unwanted impurities that reduce the extraction efficiency of the stopped ions by molecular formation, recombination or charge exchange. In order to keep the
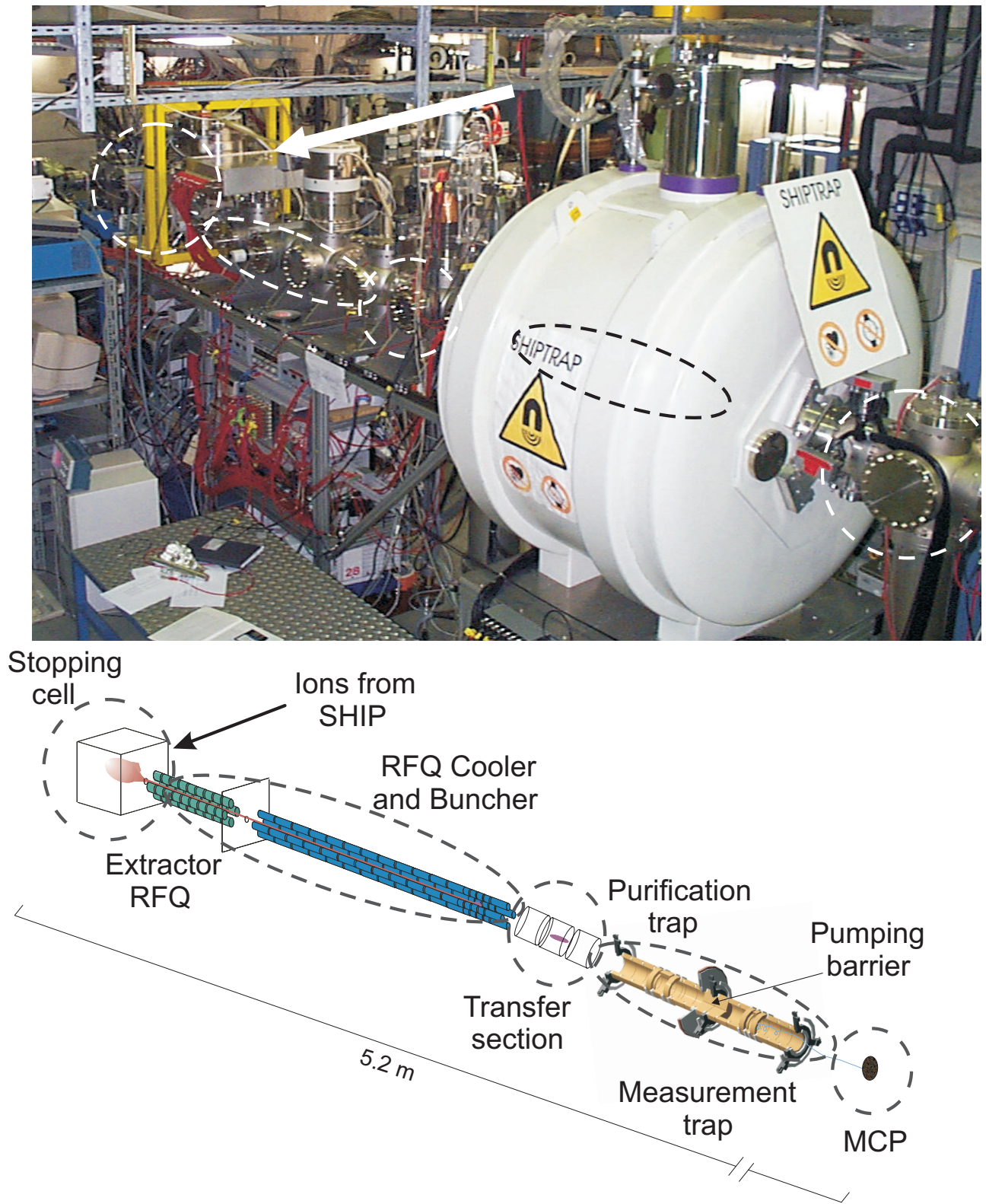
Figure 5.1: Schematic overview of the SHIPTRAP setup. Ions from the velocity filter SHIP are first stopped in the gas stopping cell and guided by the extraction RFQ into the RFQ cooler and buncher. A low emittance bunch of ions is then transferred to the double Penning-trap system where the mass determination is performed.
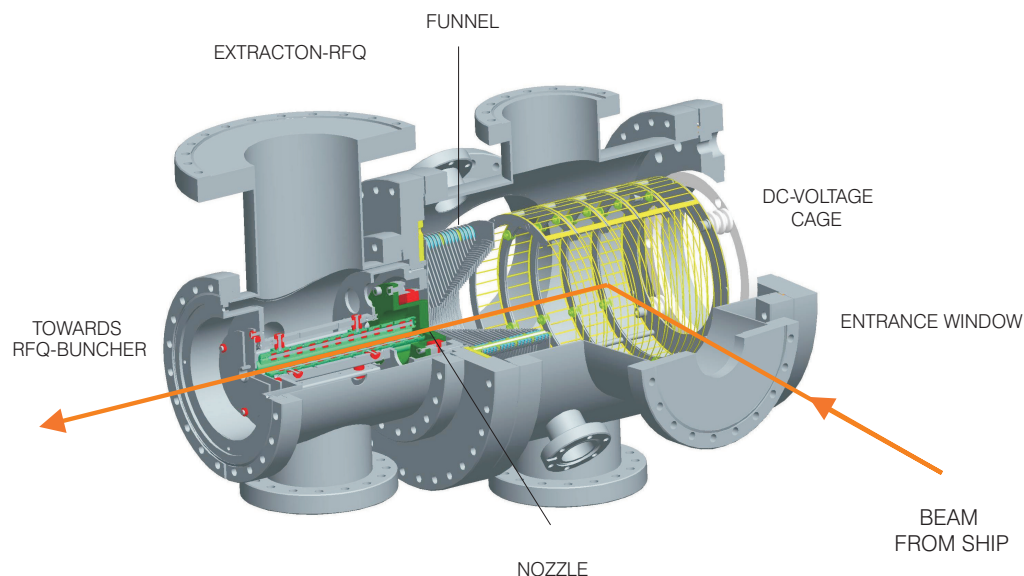
Figure 5.2: The SHIPTRAP gas cell. Ions from SHIP enter the cell through a thin foil window and are subsequently stopped by collisions with the He buffer gas. A combination of DC and RF fields guide the ions through the nozzle where they are swept out in a supersonic gas jet into the extraction RFQ.

extraction efficiency as high as possible ultra-high vacuum conditions are required before its operation. Therefore, a careful baking of the gas cell is performed for typically 1 to 3 days at 150°C, which ends up with a residual pressure below 10^{-9} mbar. Furthermore, highly purified He gas (99.9999% He) is employed for its use on-line, which is passed through a cold trap filled with liquid nitrogen to freeze out any impurity from the helium or even from the feeding line.

To drag the stopped ions out of the gas cell, DC potentials are applied to a cage electrode system in order to guide the ions towards a funnel-shaped configuration of 40 ring electrodes, which are installed in front of the nozzle. The voltage applied to the funnel consists of both DC and RF components to achieve a better focusing and acceleration towards the nozzle. The RF field is applied with 180° phase difference between two adjacent electrodes in order to generate a pseudo-potential, which prevents ion losses by hitting the funnel electrodes. Both sides of the nozzle have a conical shape. The ions are extracted by means of the gas flow, which is optimized to achieve a supersonic gas jet for an efficient transfer into the extraction RFQ. The latter consists of four 12-fold segmented rods which create a longitudinal DC potential. The purpose of the extraction RFQ is to guide the ions out of the gas cell and also serves as a differential pumping stage towards the RFQ buncher. The total efficiency of the gas cell, *i.e.*, the number of ions leaving the extraction RFQ divided by the number of ions impinging on the entrance window, has been determined in several on-line experiments with maximum values of 4 - 8 % [83].
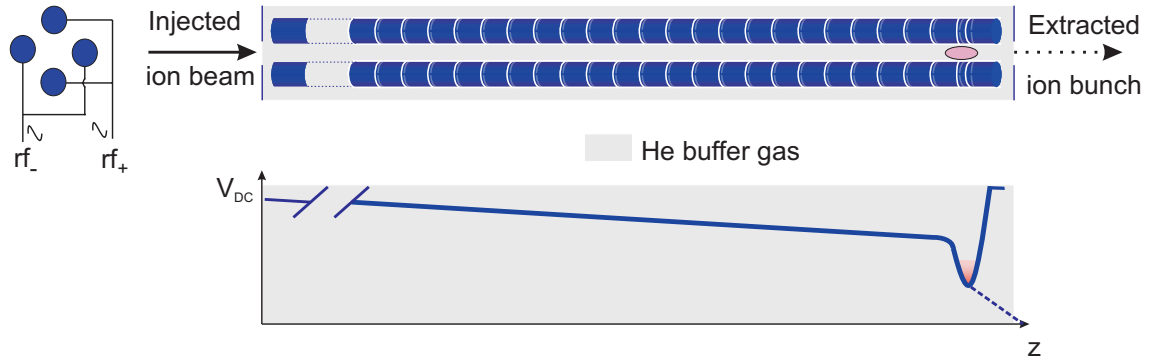
Figure 5.3: Schematic view of the SHIPTRAP RFQ buncher. (Top) Side and front view. (Bottom) Longitudinal DC potential. Collisions with the He buffer gas result in a cooling of the ions-motional amplitudes and their final trapping in the potential minimum. By lowering the voltage in the last electrode segments the bunch of ions is released.

5.2   The RFQ buncher

The SHIPTRAP RFQ buncher [32] is designed to accumulate the ions coming in a quasi-continuous beam from the gas cell and to eject them as a temporally well-defined bunch. In addition, it cools the ion motion to reduce the emittance of the ejected ion beam, which is required for an effective injection into the first Penning trap. The multi-fold segmented RF quadrupole structure confines ions radially in the pseudo-potential well of the RF quadrupole field similar to a mass filter [20] while their radial and longitudinal energy is reduced by collisions with the He buffer gas atoms at a typical pressure of 10^{-3} mbar. As the kinetic energy of the ions is dissipated, they are dragged along the ion guide by a logitudinal DC field applied to the electrode segments (see Fig. 5.3). At the end of the electrode structure a potential minimum is generated in which ions are accumulated and cooled within few milliseconds. Afterwards, the potentials of the last electrode segments are lowered and the ions are released as a low emittance bunch with a typical width of 2 μs. The efficiency of the RFQ buncher, which is defined as the ratio of the number of ions leaving the buncher to the one entering it, is found to be almost 100% in the continuous mode (no-bunching) and on the order of 50% with bunching.

The transfer section located between the RFQ buncher and the Penning traps consists of a set of electrostatic lenses and deflectors that facilitate the injection of the ion bunch into the magnetic field. In order to provide reference ions for the mass calibration, a 90° quadrupolar deflector is placed in the transfer section which allows for the injection of ions from a surface or carbon cluster ion source (see Chap. 3) into the main beam line.

5.3   The double Penning-trap system

Since a detailed description of the new cryogenic Penning-trap system for SHIP-TRAP is presented in Sec. 7.2, here only the essential characteristics of the present
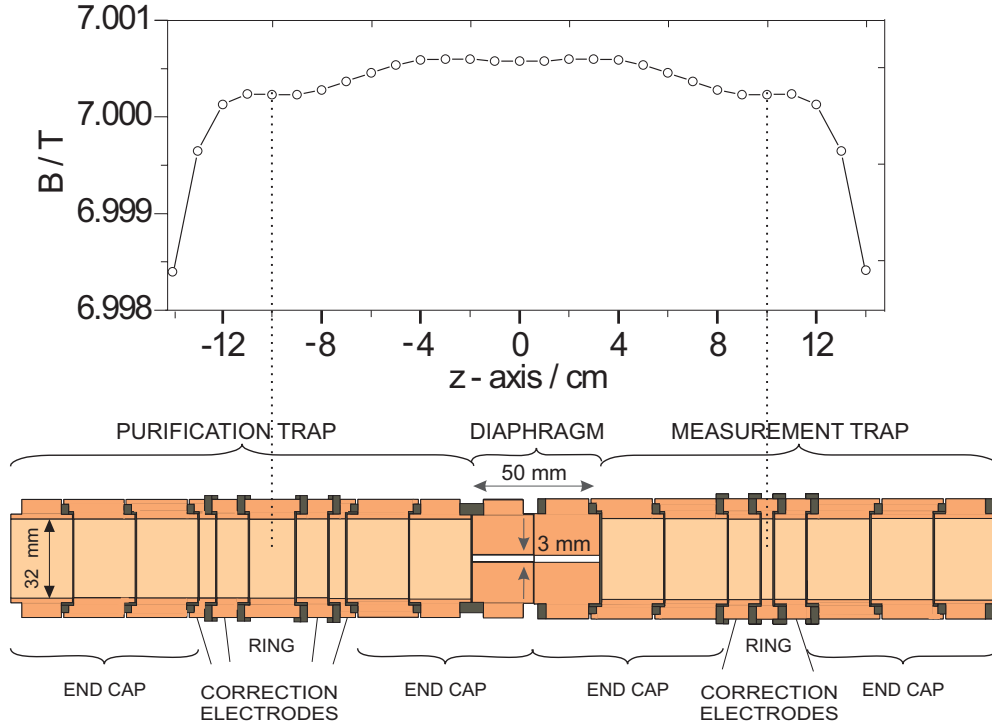
Figure 5.4: Double Penning-trap system and its location relative to the magnetic field. The trap centers, separated by 20 cm, sit in the two very homogeneous regions of the magnetic field.

room-temperature setup are given. The SHIPTRAP double Penning-trap system [84] consists of two cylindrical traps inserted in the bore of a superconducting magnet with two highly homogeneous regions[1] at approximately 7 T magnetic field strength (see Fig. 5.4). The two traps, connected by a 3 mm diameter channel, are 20 cm apart from each other and with their centers placed at the two homogeneous regions of the field. The first trap is a seven-pole *purification trap* [85] where accumulation and isobaric selection of ions are carried out by means of the buffer-gas cooling technique [47]. It consists of an eight-fold segmented ring electrode with a pair of inner and outer correction electrodes and a set of three-fold segmented endcaps. The azimuthally eight-fold segmentation of the ring electrode allows one to perform even octupolar excitation (see Sec. 2.4) [44, 45] and thus to increase the precision of the mass measurement. The second, so-called *measurement trap* is used to perform a determination of the cyclotron frequency by means of the TOF-ICR technique. It has a five-pole cylindrical geometry with a slightly shorter ring electrode. All trap electrodes are made from oxygen-free-electrolyte (OFE) gold plated copper. As insulation material between electrodes aluminum oxide Al_2O_3 is used. The dimensions and operation voltages are given in [84].

---

[1]At the precision trap the homogeneity is $\Delta B/B = 0.14$ ppm and at the purification trap $\Delta B/B = 1$ ppm.
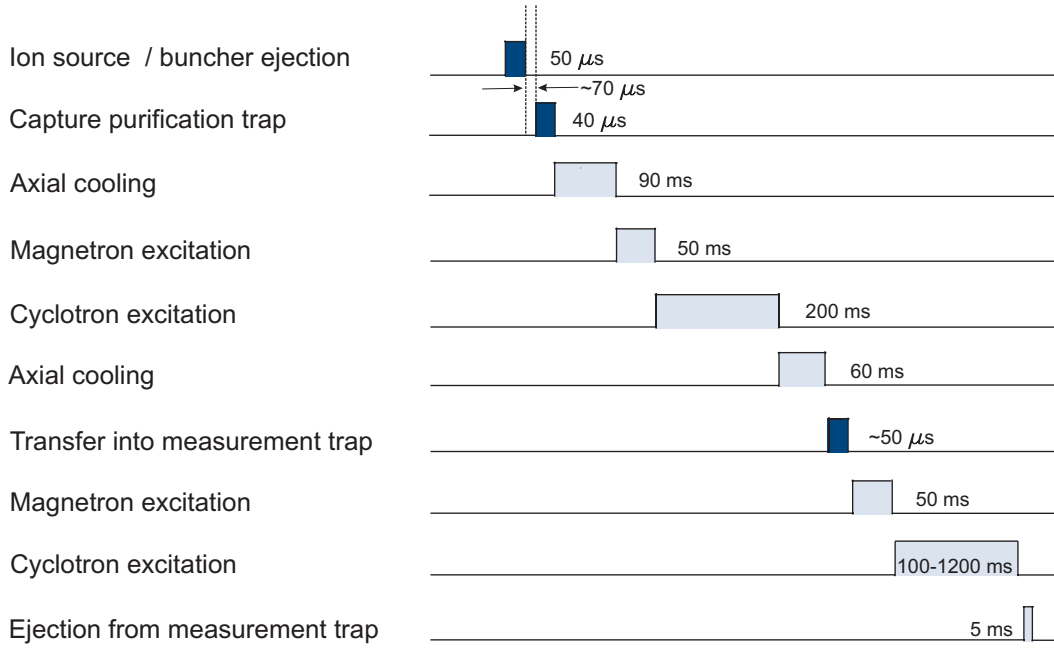
Figure 5.5: Sequence of an individual measurement cycle at a fixed excitation frequency. The dark pulses are enlarged for better visibility and the symbol $\sim$ indicates that the pulse width depends on the charge-to-mass ratio of the investigated ion. Cleaning times to remove contaminations in the precision trap are not indicated.

5.4 Experimental mass measurement procedure using TOF-ICR

The measurement procedure for the determination of the cyclotron frequency consists of several frequency scans around the predicted center frequency. Figure 5.5 shows the timing sequence of a measurement cycle, which takes place for each individual frequency step in a scan[2]. The number of collected scans in a given measurement depends upon the level of precision desired for the final mass value.

After the ion beam coming from SHIP or from one of the off-line ion sources is accumulated in the buncher, a bunch of ions is ejected into the purification trap. This ejection time defines the starting point of the individual measurement cycle. After a waiting time of around 70 μs the purification trap is opened for 40 μs by lowering the voltages in the entrance endcaps and correction electrodes (see Fig. 5.4). This delayed capture time is a critical parameter since a slight change of few μs can cause the loss of the ions. The proper value depends not only on the starting point of the ions but also on the voltage settings in the transfer section and on the ion's charge-to-mass ratio.

Once the ions are trapped in the purification trap they are stored for usually 400 ms, which includes the first waiting time for axial cooling, the time for magnetron and cyclotron excitation, and a further waiting time for a final axial and radial cooling. After this, ions are transferred through the 3 mm diaphragm into the

---

[2]Typically a frequency scan comprises 41 individual frequency steps.

measurement trap by lowering the voltages of the exit endcaps of the purification trap and the entrance endcaps of the measurement trap. Again a precise timing is crucial for an optimum transfer and furthermore for a precise mass determination. A badly synchronized timing can produce a non-desirable axial excitation of the ions when closing the endcap in the measurement trap. This gain in axial energy reduces the contrast of the cyclotron resonance and limits finally the achievable precision of the measurement. A dipolar excitation at the magnetron frequency is performed in order to prepare the ions in a pure magnetron motion for the subsequent excitation with a quadrupolar RF field (see Sec. 2.4.2). The excitation times vary from 100 to 1200 ms depending on the half-life of the investigated species and on the pressure conditions. As will be described in Sec. 7.3.2, collisions with the diffused buffer gas from the purification trap limit the applicable excitation time due to the damping of the resonance curve. With the new pumping barrier, designed and tested within this work, longer excitation times will be possible, which will enable a higher precision in the mass measurements.

The last step is the ejection of the ions by lowering the voltage of the exit endcaps of the measurement trap, which serves as a starting trigger for the time-of-flight measurement. A multichannel analyzer (MCA) is started to register the arrival time of the ejected ions. Successive measurements yield a resonance curve from which the cyclotron frequency ν_c is obtained by a fit of the theoretical lineshape to the data points.

The experimental result of a measurement at SHIPTRAP is a frequency ratio, $r = \nu_{c,ref}/\nu_c$, between the cyclotron frequencies of the reference ion and the ion of interest. In such way, the result is not affected by an eventual change in the mass value of the reference ion at a later time. In order to determine this ratio one has to account for the constant drift of the magnetic field, which has to be known at the moment where the ion of interest was measured. To this end, the measurement of a reference ion, with well-known mass, before and after the measurement of the ion of interest is used to determine the value of B by a linear interpolation.

Chapter 6

Results of on-line mass measurements around $A = 90$

During three days of beam time in July 2006 a number of mass measurements were carried out at the mass spectrometer SHIPTRAP. The UNILAC primary beam of ^{40}Ca ions at 200-MeV energy was used in combination with a 0.5 mg/cm^2 target of ^{58}Ni to produce neutron-deficient species of technetium, ruthenium, and rhodium (see Fig. 6.1) in the region around $A = 90$ via fusion-evaporation reactions. This chapter intends to motivate - as a complement to the introduction - the experimental data and to report on the measured masses and the data analysis procedure. By means of the latter, a set of values with their uncertainties properly assigned will be obtained and will enable a final adjustment of the data in the so-called Atomic-Mass Evaluation (AME). To end with the chapter a summary of the results and the consequences of those will be addressed.

91 Rh 46	92 Rh 47	93 Rh 48	94 Rh 49	95 Rh 50
1.74 s 7/2+# M⁻59100# (400#) β+=100% β+p?	4.3 s (6+) M⁻63360# (400#) β+=100% β+p=?	13.9 s 9/2+# M⁻69170# (400#) β+=100% β+p?	25.8 s (8+) Eex 300# (200#) β+=100% | 70.6 s (2+,4+) M⁻72940# (450#) β+=100% β+p=1.8 (5%)	1.96 m (1/2)⁻ Eex 543.3 (0.3) IT=88 (5)% β+=12 (5)% | 5.02 m (9/2)+ M⁻78340 (150) β+=100%

90 Ru 46	91 Ru 47	92 Ru 48	93 Ru 49	94 Ru 50
11 s 0+ M⁻65310# (300#) β+=100%	7.6 s (1/2⁻) Eex 80# (300#) β+=100% β+p=?... | 9 s (9/2+) M⁻68660# (580#) β+=100%	3.65 m 0+ M⁻74410# (300#) β+=100%	2.20 us (21/2) Eex 2082.6 (0.9) IT=100% | 10.8 s (1/2)⁻ Eex 734.40 (0.10) β+=78.0 (23)% IT=22.0 (23)%... | 59.7 s (9/2)+ M⁻77270 (90) β+=100%	71 us (8+) Eex 2644.55 (0.25) IT=100% | 51.8 m 0+ M⁻82568 (13) β+=100%

89 Tc 46	90 Tc 47	91 Tc 48	92 Tc 49	93 Tc 50
12.9 s (1/2⁻) Eex 62.6 (0.5) β+=100% IT<0.01% | 12.8 s (9/2+) M⁻67840# (200#) β+=100%	49.2 s (8+) Eex 310 (390) β+=100% | 8.7 s 1+ M⁻71210 (240) β+=100%	3.3 m (1/2)⁻ Eex 139.3 (0.3) β+>99% IT<1% | 3.14 m (9/2)+ M⁻75980 (200) β+=100%	1.03 us (4+) Eex 270.15 (0.11) IT=100% | 4.25 m (8)+ M⁻78935 (26) β+=100%	10.2 us (17/2)⁻ Eex 2185.16 (0.15) | 43.5 m 1/2⁻ Eex 391.84 (0.08) IT=76.6 (11)% β+=23.4 (11)% | 2.75 h 9/2+ M⁻83603 (4) β+=100%

Figure 6.1: Nuclides for which a mass measurement was carried out in the SHIPTRAP campaign of July 2006. The red color indicates species measured for the first time.

6.1   The importance of experimental data for rp-process calculations

Proton capture is one of the major mechanisms in the physics of stellar nucleosynthesis. In particular, the rapid capture of protons on seed nuclei is known as rp-process, breaking out from the CNO cycle. The main galactic scenario of such a process is for example the *type I* X-ray burst, which occurs when a neutron star accretes hydrogen rich matter from a companion star in a binary system. The explosive burning of hydrogen at high temperatures of $3 \cdot 10^8$ K and densities of around 10^6 g/cm^2 draw a pathway far away from the valley of β-stability through the region of neutron-deficient nuclei in a time scale of 10 to 100 seconds [11]. Calculations for different hydrogen abundance rates show that the rp-process can not overcome the closed SnSbTe cycle [86].

In order to constrain the stellar conditions and to understand the energy production, which is directly related to the observed luminosity, it is necessary to know the nuclear-physics parameters accurately [87]. For example, for the understanding of x-ray burst light curves it is a prerequisite to understand the rp-process in some detail, such as its pathway, its energy generation rate, and its endpoint.

For a given temperature, density, and composition of the seed nuclei, the rp-process reaction path is almost completely determined by proton-capture Q-values. The other important nuclear-physics input data, *i.e.*, the reaction rates, are also influenced by the nuclear binding energies and receive contributions from separation energies, pairing, and shell correction energies. Thus, nuclear masses are among the most important parameters for reliable rp-process nucleosynthesis calculations [13].
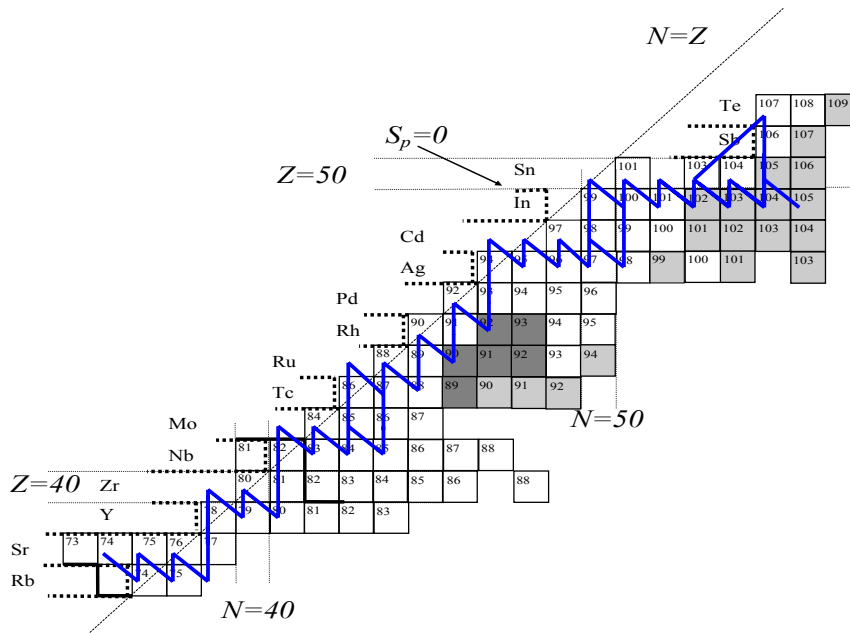
Figure 6.2: Sketch of the rp-process pathway in the endpoint region. The gray shaded squares mark the nuclides whose masses were measured at SHIPTRAP. The dark gray squares indicate nuclides measured for the first time [88].

Table 6.1: List of nuclides investigated in this work with half-life $T_{1/2}$, spin-parity J^π, and excitation energy of the first isomeric state E_{exc} [1]. The parenthesis in the third column indicates uncertain values of spin and/or parity, while # indicates a value that is estimated from systematic trends (from neighboring nuclides with same Z and N parities). The results of the PACE4 simulations for the reaction of interest yields the tabulated cross sections σ within a 10% error [89]. Additional calculations are used to get the transmission T through SHIP with 5% uncertainty [89]. With these numbers the yield in front of the gas cell for the investigated evaporation residues is calculated.

Nuclide	$T_{1/2}$	J^π	$E_{\text{exc}}/$ keV	$\sigma/$ mb	$T/\%$	Yield$/s^{-1}$
^{89}Tc	12.8 s	$(9/2^+)$		4.7	10	12562
^{89m}Tc	12.9 s	$(1/2^-)$	62.6(5)			
^{90}Tc	8.7 s	1^+		76.9	8	165137
^{90m}Tc	49.2 s	(8^+)	310(390)			
^{91}Tc	3.14 m	$(9/2^+)$		13.3	14.5	51766
^{91m}Tc	3.3 m	$(1/2^-)$	139.3(3)			
^{92}Tc	4.25 m	(8^+)		248	19	1264835
^{92m}Tc	1.03 μs	(4^+)	270.15(11)			
^{90}Ru	11 s	0^+		3.2	-	-
^{91}Ru	9 s	$(9/2^+)$		5.4	6.5	9422
^{91m}Ru	7.6 s	$(1/2^-)$	80(300)#			
^{92}Ru	3.65 m	0^+		57.7	22	340743
^{94}Ru	51.8 m	0^+		2.9	-	-
^{94m}Ru	71 μs	(8^+)	2644.6(3)			
^{92}Rh	4.3 s	(6^+)		2.5	-	-
^{93}Rh	13.9 s	$9/2^+$#		21.8	23	134590

The time scale of the rp-process is mainly given by the half-lives of the waiting points which are near the proton drip line where further proton captures are counteracted by (γ,p) photodesintegration of weakly proton bound, or proton unbound nuclei, forming equilibrium clusters that prevent the reaction paths from reaching or crossing the drip line. These waiting points delay the nuclear energy release and therefore affect the burst shape and duration [91, 92].

So far, most of the proton- and α-separation energies along the rp-process pathway are experimentally unknown. Due to this lack of knowledge, calculations are at present based on predictions of mass models and formulas, *e.g.* Skyrme Hartree-Fock mass formula [90], but the remaining uncertainties are still too large to properly calculate X-ray burst light curves. Hence, experimental mass measurements are then required. Even if the nucleus of interest cannot be accessed directly, the investigation of its vicinity will help to test the mass models and to improve their predictive power. In addition, short-range extrapolations yield more reliable estimates [6].

Motivated by these ideas, SHIPTRAP began a program to measure the masses of neutron-deficient medium-heavy nuclei up to and beyond the $N = Z$-line of interest for nuclear astrophysics. At present around 40 masses directly related with the rp-process calculations have been measured [93]. Figure 6.2 shows the rp-prosses path

way in the vicinity of its endpoint and the masses measured at SHIPTRAP in two runs of 2006. This work reports on ten of them. In Tab. 6.1 the main features of the nuclides investigated within this work are included. In the cases where an excited isomeric state is known to exist, it is also specified to facilitate the data analysis discussion in the next section. The half-lives $T_{1/2}$, spin-parities J^π, and excitation energies E_{exc} of the first isomeric state are given according to the NUBASE2003 evaluation [1]. The production cross sections σ have been calculated by means of the code PACE4, based on the statistical model. In order to produce reliable estimations, the parameters of the simulation are fixed as to reproduce the known experimental cross section of ^{92}Rh at 180 MeV primary beam energy [94]. Subsequently, the production cross section are re-calculated for a beam energy of 200 MeV [89]. The transmission T through SHIP is also calculated [89] for the seven most abundant evaporation residues (the three smallest cross sections correspond to a very small amount of evaporation residues generated by the Monte-Carlo code). The last column gives the number of ions per second of each species just in front of the gas cell. For their calculation an average primary beam current intensity of 400 particles-nA (20 eμA) was deduced from the available data of the whole beam time period.

With the help of the theoretical cross section and the transmission through SHIP, given in Tab. 6.1, the overall detection efficiency of the SHIPTRAP setup can be determined for the reported beam time. Such calculations are performed for two different species for which the intensity of the primary beam is well known during the measurement period. The number of events detected on the MCP for the time-of-flight spectrum of a given radionuclide is compared to the number of nuclides of these species in front of the gas cell just after the velocity filter. For the case of ^{92}Tc the overall efficiency is found to be $\epsilon = (2.3 \pm 0.3) \cdot 10^{-4}$ whereas for ^{92}Ru is $\epsilon = (3.6 \pm 0.4) \cdot 10^{-4}$. The two cases slightly differ from each other mainly due to the unpredicted fluctuations of the beam intensity not taken into consideration in the calculation of the uncertainties. The low efficiency measured is approximately ten times smaller than the one normally specified for the setup (about $\epsilon = 5 \cdot 10^{-3}$). The reason for that decrease might be because prior to the beam time the transfer section and trap voltages were optimized for the off-line ions from a source of ^{219}Rn located in the gas cell. This voltages, however, were not optimized again during the beam time, which might have produced a decrease of the total efficiency due to the much lighter species investigated.

6.2   Data analysis

As mentioned in Sec. 5.4 the result of a measurement at SHIPTRAP is given as a frequency ratio from which the mass value is calculated via the relation

$$r = \frac{\nu_{\mathrm{c,ref}}}{\nu_c} = \frac{q_{\mathrm{ref}}}{q} \cdot \frac{m - (q \cdot m_e)}{m_{\mathrm{ref}} - (q_{\mathrm{ref}} \cdot m_e)} \,, \tag{6.1}$$

and in the case of singly charged ions $q = q_{\mathrm{ref}} = 1$ it becomes

$$m = r(m_{\mathrm{ref}} - m_e) + m_e \,, \tag{6.2}$$

where m_e is the electron mass that must be introduced in order to obtain the atomic and not the ionic mass.

An important analysis tool used to detect the presence of contaminants during the frequency measurement is the count-rate or Z-class analysis. In this method the resonance frequency is calculated for different groups of ions or z-classes. The classes are ordered by the number of ions present in the trap content in each frequency step. A graphical representation of the cyclotron frequency as a function of the different classes can be used to determine possible frequency shifts. The slope of the regression line formed by the different data point is an indication of this shift. By extrapolation to one ion in the z-class the frequency measurement can be corrected from the influence influence contaminants, as *e.g.*, isobars and isomeric states.

The analysis of the data in this work is done following the analysis procedure used at ISOLTRAP and described in detail by A. Kellerbauer *et al.* [95]. Here, a brief description of these procedure is given, including all contributions to the total uncertainty.

1. A least-squares fit of the theoretical line shape (see Eq. (2.26)) to the experimental data points is initially performed using the fitting program *Eva 6.0.7.5*. From this fit the free cyclotron frequency ν_c and its statistical uncertainty σ_s are obtained (see Fig. 7.16).

2. A count-rate class analysis [95] is performed when the statistics is sufficiently high in order to eliminate the influence of contaminants on the cyclotron frequency value. This extrapolation of the cyclotron frequency ν_c to a single trapped ion increases the initial statistical uncertainty by a factor of 2 to 3. For the cases in which the statistics is not sufficient to perform the count-rate class analysis, the errors are increased by a certain value in order not to favor the low statistics measurements with a smaller uncertainty than the ones with more statistics. The added offset is an average value calculated from those cases where the count-rate analysis was possible.

3. A pair of measurements of the reference ion (in this work $^{85}\text{Rb}^+$), before and after the measurement of the investigated radioactive ion, is performed to calibrate the magnetic field B. A linear interpolation is used to calculate the value of B at the time of the measurement of the radioactive ion of interest.

4. With these data a frequency ratio $r = \nu_{c,\text{ref}}/\nu_c$ is calculated and an uncertainty accounting for the variations of the magnetic field (see Sec. 2.3) in the time scale of the measurement is given. Its magnitude was determined by recording the cyclotron frequencies of $^{133}\text{Cs}^+$ and $^{85}\text{Rb}^+$ over an extended period of some days. In such a way the measured magnetic field at a time t was compared to the one obtained via interpolation for different time intervals $(t - \Delta t, t + \Delta t)$ leading to the reported uncertainty [65]. Accordingly, an uncertainty $\sigma_B = 5 \cdot 10^{-9}\,\text{h}^{-1} \cdot \Delta t$, depending on the time interval Δt between the measurements of the reference ion, is quadratically added to the uncertainty of each frequency ratio.

5. The weighted mean value of the available frequency ratios for a given nuclide is calculated. Internal versus external uncertainty consistency are compared. The ratio of both was found to be very close to unity in all cases indicating that only statistical fluctuations due to accidental errors are present in the
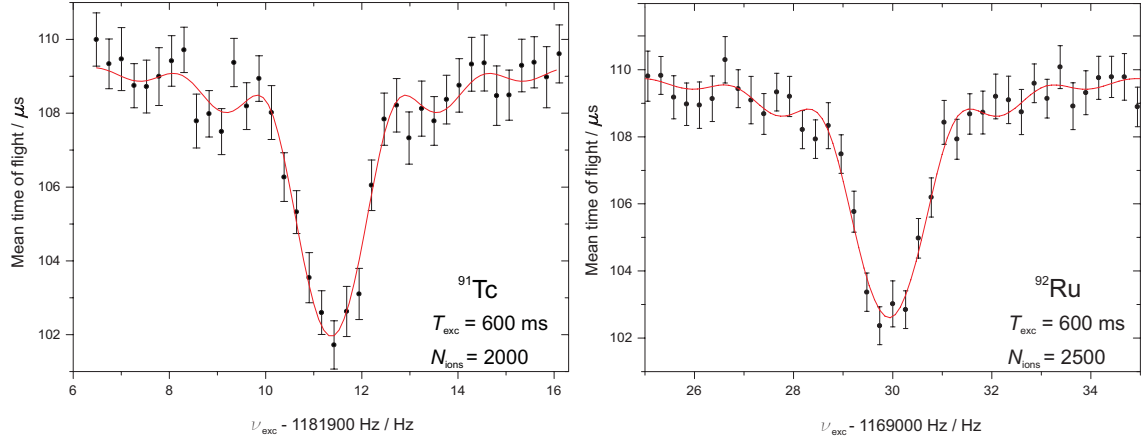
Figure 6.3: Fit of the theoretical line shape to the experimental data points of two of the nuclides investigated in this work. The fitting procedure results in the cyclotron frequency and its statistical uncertainty of $\nu_c = (1181911.36 \pm 0.04)$ Hz in the case of ^{91}Tc (left) and $\nu_c = (1169029.94 \pm 0.04)$ Hz in the case of ^{92}Ru (right).

experimental data [96]. The larger value of both is preferentially taken as the final uncertainty. In this way the uncertainties are always given conservatively.

6. By means of cross-reference mass measurements with carbon clusters at SHIP-TRAP [57], a relative mass-dependent shift of $\sigma_m = (1.1 \pm 1.7) \cdot 10^{-10}/u \cdot \Delta(m/q)$ was revealed, where $\Delta(m/q)$ indicates the difference of mass-to-charge ratio between the radionuclide of interest and the reference ion. The averaged frequency ratio is corrected by the amount of this shift and the same quantity is quadratically added to its uncertainty. Since the true frequency ratio of carbon clusters of different sizes is exactly known[1] the relative residual uncertainty was determined to be $\sigma_{res}/r = 4.5 \cdot 10^{-8}$, which is quadratically added to give the final uncertainty of the frequency ratio.

Table 6.2 summarizes the results obtained in the data analysis. For the species investigated during the data acquisition the total number of detected ions N_{ions} after a summation of the individual resonances and the ratio r of the cyclotron frequency of the reference ion ^{85}Rb$^+$ to that of the ion of interest with the total error (statistical plus systematic) in parenthesis are given. The experimental atomic masses m (u) and their uncertainties were calculated using Eq. (6.2). In the last column the relative overall mass uncertainties $\delta m/m$ are listed. The values used in combination with Eq. (6.2) to yield the atomic mass values are $m(^{85}\text{Rb}) = 84.911789738(12)$ u [98], where u is the unified atomic mass unit which is defined as $1/12$ of the atomic mass of the most abundant carbon isotope ^{12}C, $1u = 931494.009(7)$ keV [98], and the electron mass $m_e = 548.5799110(12)$ μu [99].

---

[1]The estimated values of the molecular binding energy/atom of the carbon clusters varies from 3.1 eV in ^{12}C$_2$ to 7.0 eV in ^{12}C$_{60}$ [97], therefore it is negligible at the present uncertainty level for mass measurements at SHIPTRAP.

Table 6.2: Measured cyclotron frequency ratios $r = \nu_{\mathrm{ref}}/\nu_{\mathrm{c}}$ for the nuclides investigated during the SHIPTRAP campaign of July 2006. In all cases ^{85}Rb was used as reference nuclide. The derived atomic masses m and their relative uncertainties are given in the fourth and fifth column, respectively. Uncertainties (in parentheses) refer to the least significant digits of a quantity. The uncertainties of the frequency ratios are given to two to three figures to reduce rounding errors in subsequent calculations such as the atomic-mass evaluation. For more details, see text.

Nuclide	N_{ions}	r	$m\,(u)$	$\delta m/m \cdot 10^{-8}$
^{89}Tc	879	1.047 294 809(203)	88.927 650(17)	19
^{90}Tc	2516	1.059 029 697(94)	89.924 0745(80)	8.9
^{91}Tc	5890	1.070 740 167(63)	90.918 4251(54)	5.9
^{92}Tc	7638	1.082 480 188(137)	91.915 284(12)	13
^{90}Ru	259	1.059 103 727(127)	89.930 361(11)	12
^{91}Ru	1111	1.070 838 208(131)	90.926 749(11)	12
^{92}Ru	5691	1.082 538 554(67)	91.920 2408(57)	6.2
^{94}Ru	1093	1.105 987 624(289)	93.911 330(25)	26
^{92}Rh	220	1.082 681 725(434)	91.932 398(37)	40
^{93}Rh	1035	1.094 382 514(141)	92.925 926(12)	13

6.3 The atomic-mass evaluation

The 2003 Atomic-Mass Evaluation [98] is the latest compilation of atomic mass values and related properties, as *e.g.* binding energies, nuclear reaction, and separation energies. Such a collection of information is continuously updated by G. Audi *et al.* with new input data coming from nuclear spectroscopy or mass spectrometry experiments and is regularly published every few years. An atomic mass value is generally given as a mass excess D, which is defined as

$$D = (m\,[\text{in}\,u]\, -\, A)\ [\text{in keV}]\,,\tag{6.3}$$

where m is the atomic mass and A is the atomic mass number.

A comparison between the data of the AME2003 and the experimental data analyzed in this work is shown in Fig. 6.4. Here, the difference of mass-excess values $(D_{\mathrm{AME2003}} - D_{\mathrm{exp}})$ is plotted for each nuclide. A good agreement with the already measured values is found but with a significant reduction of the uncertainties up to a factor of 40 (with the exception of ^{92}Tc and ^{94}Ru). The comparison with the data deduced using systematic trends (labeled with #) suggest states less bound than experimentally predicted, *i.e.* with negative mass deviation for all cases. The evaluation of the data presented in this work was performed in collaboration with G. Audi, the evaluator and editor of the mass tables, during a visit to his home institute at the Centre de Spectrométrie Nucléaire et de Spectrométrie de Masse (CSNSM) in Orsay from the 24th to the 27th of May 2007. The evaluation procedure mainly consists of solving an overdetermined system of linear equations, which contain the experimental input values and their uncertainties, studied either in production or decay reactions, or by mass spectrometry. Each experimental datum sets a relation in mass or energy among two nuclides and thus a multi-pole relation

around it is formed. When a given nuclide is only connected by a single relation to another nuclide it is called a *secondary nuclide* and the equation describing the relation between them can be excluded from the general system of equation without loss of information. Nuclides that are interconnected by more than one relation are called *primary nuclides*. In order to consider all relations between primary data an adjustment by a least-squares method is used, which is weighted according to the precision with which each piece of data is known. As a result, a set of adjusted mass values is obtained [100].
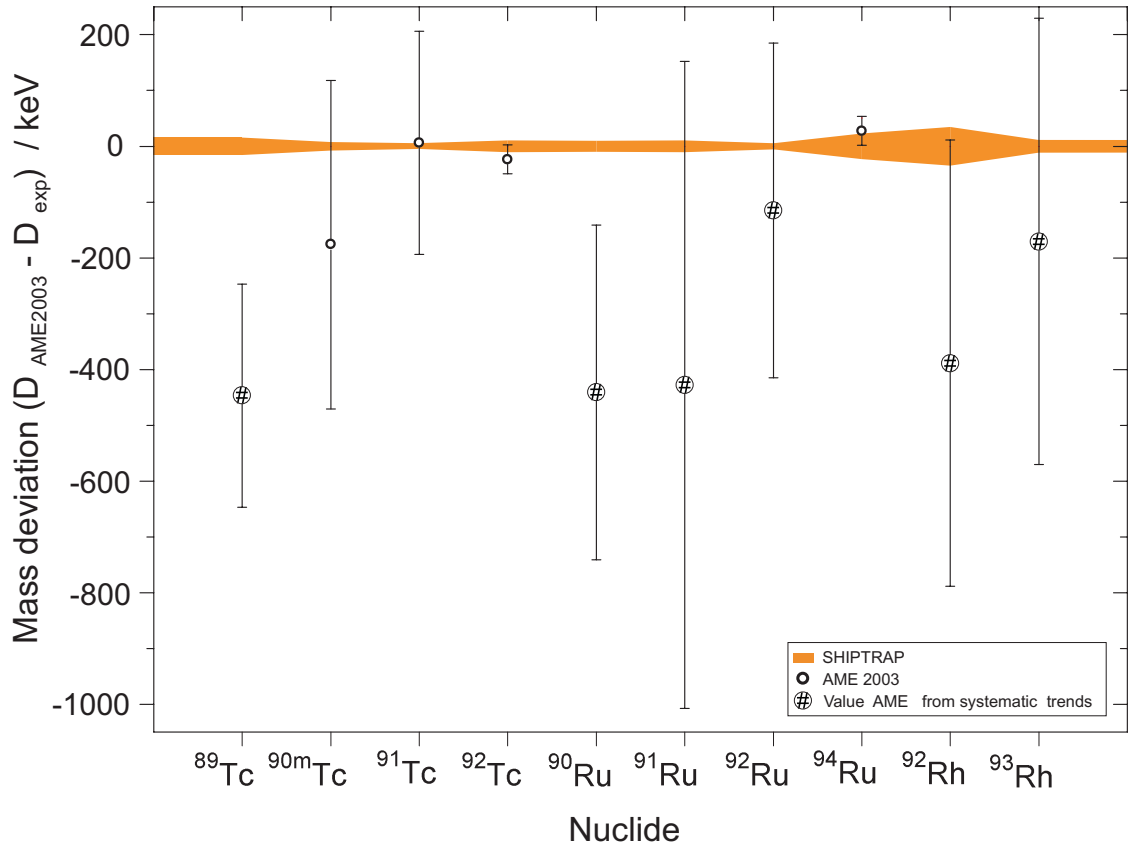
Figure 6.4: Difference of mass-excess values $(D_{\mathrm{AME2003}} - D_{\mathrm{exp}})$ of the investigated nuclides taken from this work (D_{exp}; see Tab. 6.2) and the literature [98]. The shaded area indicates the uncertainties of the SHIPTRAP data. The empty circles represent the AME data which are found to be in good agreement with our values while the filled circles with the symbol # correspond to data derived from the behaviour of systematic experimental trends. Here, the tendency is to predict states that are more bound than experimentally measured, *i.e.* with negative mass deviations for all cases.

6.3.1 Treatment of the input data

In the following the discussion of the treatment of the input values and the final results of the evaluation are presented. All nuclides are considered to exhibit the spin and half-life properties from NUBASE [1] as listed in Tab. 6.1, which served as

a basis for this discussion. The mass excess values obtained within this work D_{exp} are listed in Tab. 6.3.

^{90}Tc

Before the SHIPTRAP measurement the radioactive nuclide ^{90}Tc was produced by the (p,3n) reaction at 40 MeV beam energy and studied by means of β-decay spectroscopy in two independent experiments at Foster Radiation Laboratory in Canada [101, 102]. Two long-lived states were found with i) $T_{1/2} = 8.7$ s and $J^\pi = 1^+$, which is assumed to be the ground state in NUBASE2003 [1] and ii) $T_{1/2} = 49.2$ s and $J^\pi = 8^+$, which lies, according to the Atomic-Mass Evaluation AME2003 [98], at 310 (390) keV. A careful examination of our data using the count-rate class analysis [95] shows no clear evidence of a possible contamination in the trap. In another experiment, ^{90}Tc was studied as well but produced by a very different mechanism, namely the fusion evaporation reaction ^{58}Ni(^{36}Ar, $3pn$) at 149 MeV beam energy [103]. In this reaction no low spin state could be observed. This result can be easily understood since in fusion evaporation reactions states at high spin and excitation energies up to several MeV are populated due to their high geometrical cross sections [104]. Thus, a considerable amount of the flux is expected to populate high-spin states. Our production mechanism at SHIPTRAP is via fusion evaporation reactions, indicating that we most probably did measure a pure high-spin isomer. We therefore assign our result to ^{90m}Tc.

^{89,91}Tc and ^{91}Ru

These three nuclides present very similar isomeric features: a ground state with $J^\pi = 9/2^+$ and a first excited state with $J^\pi = 1/2^-$. In all three cases the half-lives of the ground and of the excited state are very similar. The excitation energies of ^{89m}Tc and ^{91m}Ru are well below the achievable experimental resolution of typically $\Delta m = 120$ keV. Despite the fact that there are only four spin units difference between both isomeric states, instead of seven for ^{90}Tc, similarly to the previous case, we assume that the high spin state products are favored due to the fusion evaporation mechanism. This fact, combined with the application of the count-rate class analysis, which shows clearly that there are no contaminants for the case of ^{91}Tc (see Fig. 6.5), supports the assignment of the mass measurement of these species to the high-spin ground state.

- For ^{89}Tc a Q_β mass measurement was performed by Heiguchi *et al.* [105] yielding a mass excess of $D = -67500(210)$ keV. However, AME2003 assumed this surface to be lower than designed by this experiment by 350 keV due to the poor knowledge of the mass surface in this region. Our result of $D = -67393(16)$ keV lies 447 keV above the value suggested by AME2003 and is in full agreement with [105], although 13 times more precise. Therefore, the value of ^{89}Tc is completely determined by the SHIPTRAP value.

- The Q_β decay energy of ^{91}Tc produced in the reaction (p,2n) at 30 MeV beam energy [102] yielded a mass excess value of -75980(200) keV, which is in exact agreement with our result, but 40 times less precise. Due to the much smaller uncertainty of the new result, the old value is outweighed.
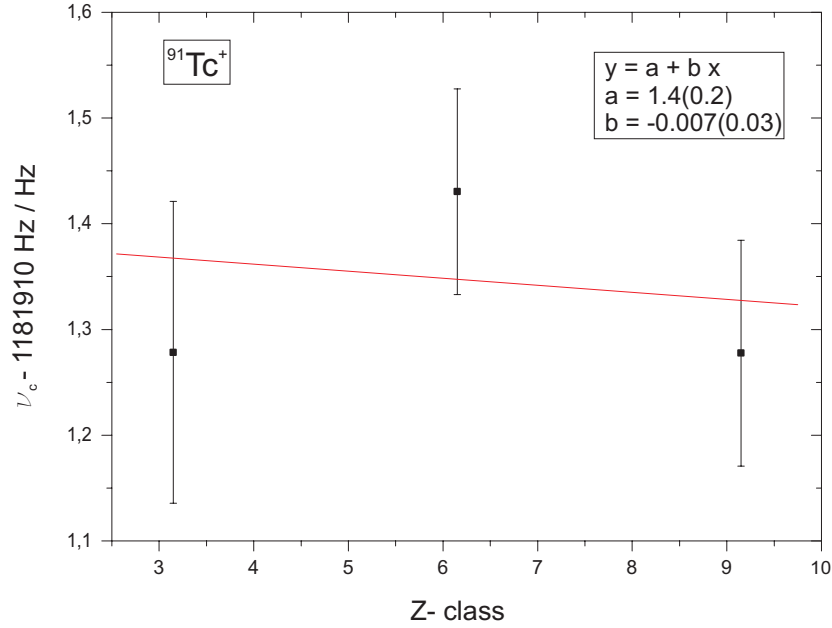
Figure 6.5: Count-rate class analysis procedure. Ions are divided in classes with different number of ions per class. The fitting line is finally extrapolated to one ion. In the plot no influence of contaminants, *i.e.* no significant shifting in the cyclotron frequency ν_c determination of ^{91}Tc for the different z-classes can be clearly observed, since the error associated to the slope of the regression line is larger than the slope itself.

- The mass of ^{91}Ru was previously unknown. In AME2003 it was deduced from the known mass of its isomer, using an estimated excitation energy of 80(300) keV. Our result for ^{91}Ru combined with the mass of the isomer, which was obtained by Hagberg [106] from delayed proton (ϵp) decay energy measurements, locates now the excited state at -350(500) keV. Given the large uncertainty in this value the assignment of the isomeric states in this nuclide is still ambiguous. However, Hagberg clearly states that the value they obtained for the (ϵp) decay energy was only a lower limit. If we assume this energy to be by 500 keV higher than the actual value of 4300 keV, then the excitation energy would be +150 keV.

^{92}Tc

Our mass excess value of $D = -78912(11)$ keV is found to be in very good agreement with all former measurements from reaction studies [107, 108]. Nevertheless, only the last one has an error small enough to be used in combination with our result to derive a mass excess value of $D_{new}^{AME} = -78916(10)$ keV determined to 12% by their work and to 88% by the measurement presented here.

Table 6.3: Summary of the mass adjustment procedure for the ten species investigated within this work. The mass excess D_{exp} refers to the experimental values measured at SHIPTRAP. The third and fourth columns show the AME2003 [98] values and the resulting values from the new evaluation after including the SHIPTRAP data, respectively. The last column shows the influence of SHIPTRAP data to the final value. The symbol # indicates values derived from systematic trends.

Nuclide	D_{exp}/ keV	D_{2003}^{AME}/ keV	D_{new}^{AME}/ keV	Infl./%
^{89}Tc	-67393(16)	-67840(200)#	-67393(16)	100
^{90m}Tc	-70724(7)	-70900(300)	-70724(7)	100
^{91}Tc	-75987(5)	-75980(200)	-75987(5)	100
^{92}Tc	-78912(11)	-78935(26)	-78916(10)	88
^{90}Ru	-64869(10)	-65310(300)#	-64869(10)	100
^{91}Ru	-68232(10)	-68660(580)#	-68232(10)	100
^{92}Ru	-74295(5)	-74410(300)#	-74295(5)	100
^{94}Ru	-82595(23)	-82568(13)	-82575(12)	23
^{92}Rh	-62971(34)	63360(400)#	-62971(34)	100
^{93}Rh	-68999(11)	-69170(400)#	-68999(11)	100

^{94}Ru

The result of this measurement of a mass excess of $D = -82595(23)$ keV agrees with the previously measured value of $D = -82568(13)$ keV determined by [109]. The newly adjusted value results in $D_{new}^{AME} = -82575(12)$ keV, derived to 23% from this work and to 77% from the measurement of [109].

The radionuclides ^{94}Ru and ^{92}Tc, discussed above, are primary elements whose mass value play an important role in a number of species due to their associated reactions.

^{90,92}Ru and ^{92,93}Rh

The mass values of these species were known only by the estimation from systematic trends [98]. Our results agree with all AME2003 values with the exception of ^{90}Ru, which is 1.5 σ more bound than derived from the results presented here. All our mass values for these four nuclides as well as most of the values already discussed above tend to locate the species less bound than predicted by systematic trends as well. Hence, the SHIPTRAP mass values suggest a lifting of the mass surface in this region by several hundreds of keV, which might be applied as a systematic trend to other neighboring isotopic chains as well.

6.3.2 Results of the evaluation and conclusions

The results of the atomic-mass evaluation procedure are summarized in Tab. 6.3. The new AME mass values of eight out of the ten species investigated are 100% influenced by the values presented in this work, either because the very first experimental mass determination was performed replacing the value predicted by systematic trends

Table 6.4: Impact of the SHIPTRAP data on some other 17 species as a result of the adjustment procedure. The second column represents the new adjusted values. ΔD shows the deviation of the new adjusted values with respect to the AME2003 data.

Nuclide	D_{new}^{AME}/ keV	ΔD/ keV
^{94}Rh	-72945(447)#	-5
^{94m}Rh	-72644(400)	-4
^{95}Ru	-83453(12)	-3
^{95}Rh	-78343(151)	-3
^{95m}Pd	-68295(300)	-5
^{96}Ru	-86075(8)	-3
^{96}Rh	-79682(13)	-3
^{96}Pd	-76232(150)	-2
^{97}Ru	-86115(8)	-2
^{97}Rh	-82592(36)	-2
^{97}Pd	-77802(302)	-2
^{97}Ag	-70822(322)	-2
^{98}Pd	-81303(21)	-3
^{99}Pd	-82190(15)	-2
^{195}Po	-11071(39)	-1
^{199}Rn	-1510 (64)	10
^{203}Ra	8657(81)	17

(^{89}Tc, ^{90}Ru, ^{91}Ru, ^{92}Ru, ^{92}Rh, ^{93}Rh) or due to its significantly improved uncertainties (^{90m}Tc, ^{91}Tc). In the two remaining cases (^{92}Tc, ^{94}Ru) the new mass value is only partially influenced by the SHIPTRAP measurements.

The four nuclides with the largest changes in the mass excess values are ^{89}Tc, ^{90}Ru, ^{91}Ru, and ^{92}Rh, where the new values are about 390 to 450 keV less bound. For these nuclides previous values have been extrapolated from systematic trends with high uncertainties. One experimental value of $D = -67500(210)$ keV [105], which had been rejected in the AME2003, agrees to our values. Therefore, we consider, taking into account our results, that the suggested value by systematical trends in AME2003, which replaced the experimental value of ^{89}Tc measured by [105], was inappropriate.

An important fact observed in the results presented here is that the mass surface must be lifted by a few hundred keV to match with the scarce available experimental data. Thus, the values measured at SHIPTRAP suggest a reshaping of the mass surface for neutron-deficient nuclides in the region between $Z = 40$ and $Z = 50$. This behavior affects the general trend of the mass surface and can be applied in order to make better predictions of the unknown species. In the case of the two primary nuclides, ^{92}Tc and ^{94}Ru, the adjustment procedure by the least-squares method has slightly modified the mass value of 17 further nuclides for the elements from rhodium to radium. Although the changes are significantly smaller and uncertainties are slightly improved, the results are compared in Tab. 6.4 in order to illustrate the amount of interconnected nuclides.
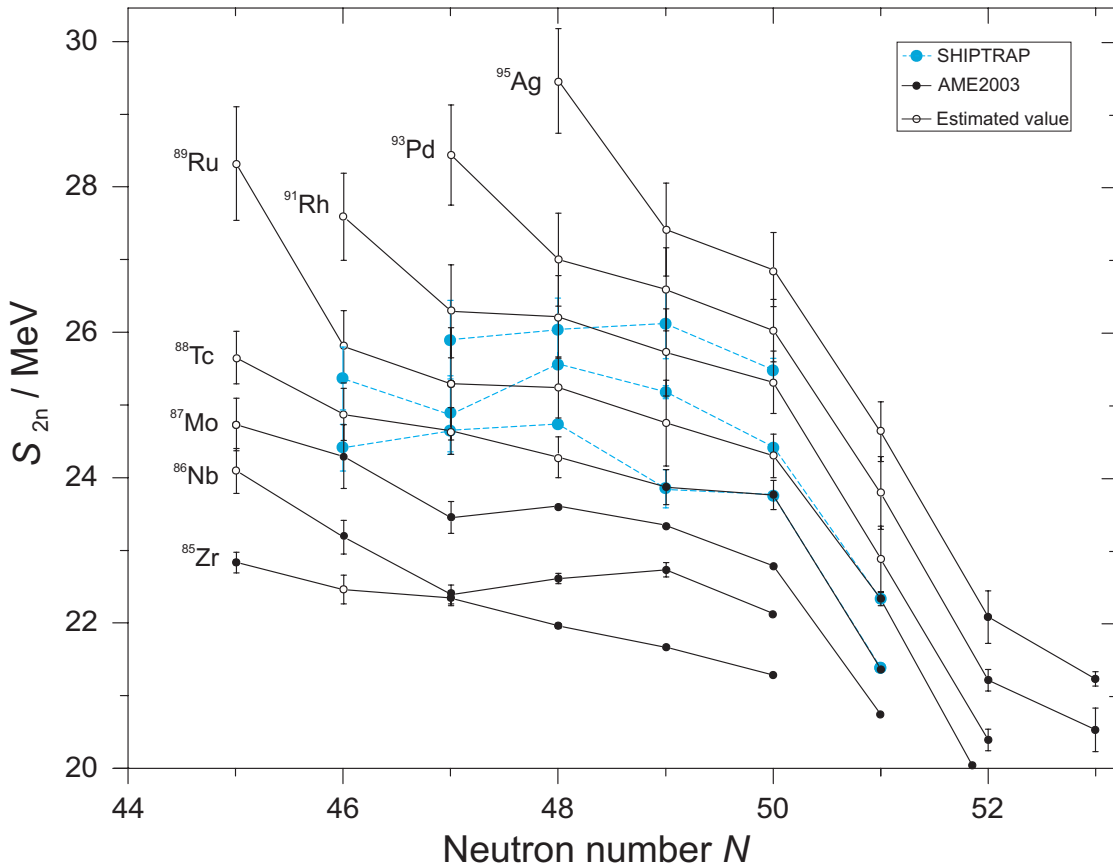
Figure 6.6: Two-neutron separation energy S_{2n} as a function of the neutron number for isotopes from zirconium to silver. The filled large circles connected by a dashed line correspond to the data investigated in this work. The data of the AME2003 are plotted as small circles whereas the empty circles are estimations based on systematic trends.

The best way of studying the nuclear structure from the behavior of mass values along isotonic and isotopic chains is by means of the nucleon separation energies, which represent the energy needed to remove (either one or two) nucleons from the atomic nucleus. Due to the odd-even behavior of pairing effects, the two-nucleon separation energy is taken as an observable for basic information of nuclear shell structure, being defined as

$$S_{2n} = B(Z, N) - B(Z, N-2) = -M(Z, N) + M(Z, N-2) + 2M_n\,, \qquad (6.4)$$

$$S_{2p} = B(Z, N) - B(Z-2, N) = -M(Z, N) + M(Z-2, N) + 2M_p\,, \qquad (6.5)$$

for neutrons and protons, respectively. The two equations are expressed as a difference of atomic binding energies B or alternatively, as a difference of atomic masses M with the corresponding neutron M_n and proton M_p masses.

Figure 6.6 shows the two-neutron separation energy S_{2n} as a function of the neutron number for the nuclides investigated in this work and also for other species, although not directly investigated. For the latter ones their separation energies are
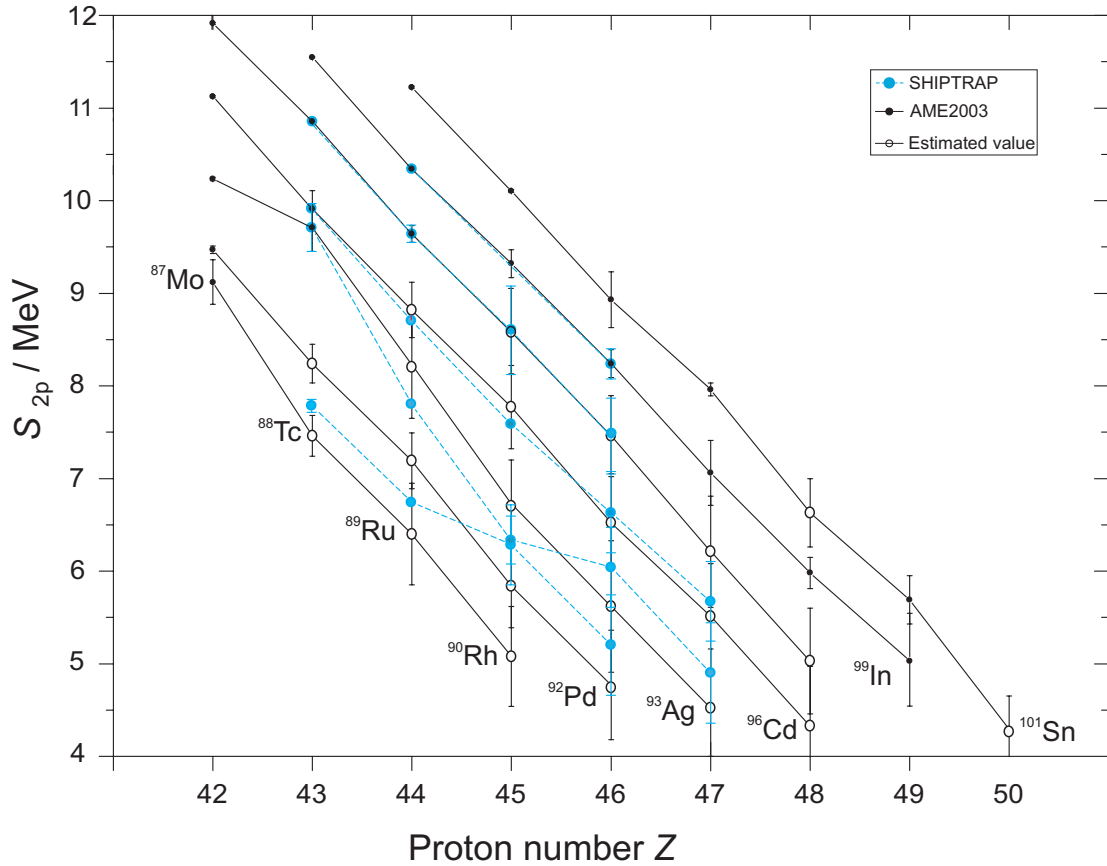
Figure 6.7: Two-proton separation energy as a function of the proton number for the isotones from molybdenum to tin. The filled large circles connected by a dashed line indicate the measured values or partially measured at SHIPTRAP. The small circles indicate the values of the AME2003, whereas the empty circles are based on systematic trends and empty dots indicate experimentally known and predicted vales of the AME2003, respectively.

partially calculated using our experimental values. The graph additionally shows the values of the AME2003 for comparison to the newly adjusted values. The filled large circles connected by a dashed line represent the values determined by this work. The filled small circles represent experimental adjusted data from the AME2003, while the empty circles correspond to values deduced from systematic trends. In the plot a good agreement of our data with the separation energies from nuclides that were already experimentally studied is observed. All three isotopic chains determined by this work show similar trends given by their parallel values with respect to each other. The largest discrepancies are visible, e.g. ^{91}Ru and ^{92}Tc, in the points for which the separation energy is calculated only partially by the SHIPTRAP data and a use of the predicted AME2003 values is made. As suggested by the results of this work, the estimation assumed in the AME2003 for these values represent the species a few hundred keV more bound than experimentally measured. Since the SHIPTRAP data added individual nuclides, a sudden deviation to the former trends is observed.

In general, the two neutron separation energy decreases along an isotopic chain

when increasing the neutron number. This feature is well explained in a macroscopic approximation of the nucleus by the Bethe-Weizsäker formula [4] as a direct consequence of the application of the *liquid drop model*. The predicted shell closure at N = 50 is observed in the plot as an pronounced decrease of the separation energies for the more weakly bound nucleons out of the shell.

The two-proton separation energy S_{2p} as a function of the proton number is given in Fig. 6.7. The situation is very similar to the one for neutrons. Again a comparison of the experimental values investigated in this work with the values of the AME2003 is done. The SHIPTRAP values agree with the values derived from previous experimental data. The expected linear trend is kept in all isotonic chains indicating no phase transition in the region investigated. Discrepancies are found for ^{91}Rh and ^{93}Pd, both with the largest associated uncertainties of 430 keV. For data that are obtained by the extrapolation of systematic trends, larger discrepancies are observed due to the mass differences resulting from the AME2003 extrapolations.

Concerning the nuclear astrophysics calculations for the synthesis of nuclides in the rp-process (r-process), proton (neutron) separation energies are the most important parameters since the maximum abundance in an isotonic (isotopic) chain, and therefore the path of the process for a given density and temperature, occurs at a fixed separation energy. The abundance ratios of two neighboring nuclei depend exponentially on binding energy differences. The results presented above will be published soon and used by nuclear astrophysicists, as *e.g.* by our collaborator H. Schatz from MSU, to determine unambiguously the rp-process pathway in the region around A=90.

As a conclusion of the evaluation one can say that the new mass values of the six species only known so far by systematic trends, are totally reliable due to the very good agreement found in the analysis for the species already measured by means of different techniques to the spectrometry with Penning traps, as β- or proton-decay spectroscopy. Furthermore, the uncertainties assigned to the data are found to be correct and justified by a calculated partial consistency factor of $\chi^2/n = 1.093$ resulting from the AME adjustment procedure of the SHIPTRAP data.

Chapter 7

Commissioning of the cryogenic Penning trap setup

This chapter reports on the commissioning and first off-line tests of a cryogenic setup for SHIPTRAP carried out at the University of Mainz. So far, mass spectrometry on radionuclides relies exclusively on the destructive TOF-ICR technique (see Chap. 4). The setup to be described in the following is a first application of the non-destructive Fourier Transform-Ion Cyclotron Resonance (FT-ICR) detection technique for the investigation of radionuclides [77, 110]. The new setup does not intend to replace the existing destructive detection technique but to complement it. That means that both, destructive and non-destructive detection will be possible, making the setup more versatile and thus, suitable to address a larger region of the nuclide chart. In order to perform all preparatory tests in our laboratory before on-line installation, the setup had to be adapted to a superconducting magnet of different geometry. The characteristics of the original magnet were presented in Chap. 5 within the layout of the SHIPTRAP experiment. Here, only the off-line setup, which uses the magnet in our laboratory, is considered. After a motivation for the non-destructive detection technique and the presentation of the test setup, the study of a differential pumping barrier, a comparison of the efficiency of channeltron and MCP detectors, and the test of the superconducting coil for the FT-ICR detection are described.

7.1 The need of a non-destructive detection technique

At the Penning trap mass spectrometer SHIPTRAP more than 50 neutron-deficient radionuclides have been studied in the first period of operation using the TOF-ICR detection technique [88, 111]. With this detection method at least on the order of 300 detected ions are required for the accumulation of a cyclotron resonance curve and hence, to obtain a single mass value. Due to the temporal instability of the magnetic field (see Sec. 2.3) the long measurement times, which result from the low production rates of nuclides far away from stability or in the heavy/superheavy mass region, limit the applicability of this detection technique to production cross sections in the order of 1 μb (> 1000 ions/s), when considering the present overall detection efficiency of around 0.5% (see Chap. 6). The aim of SHIPTRAP, however, is the investigation of rare transuranium species as they are produced and separated
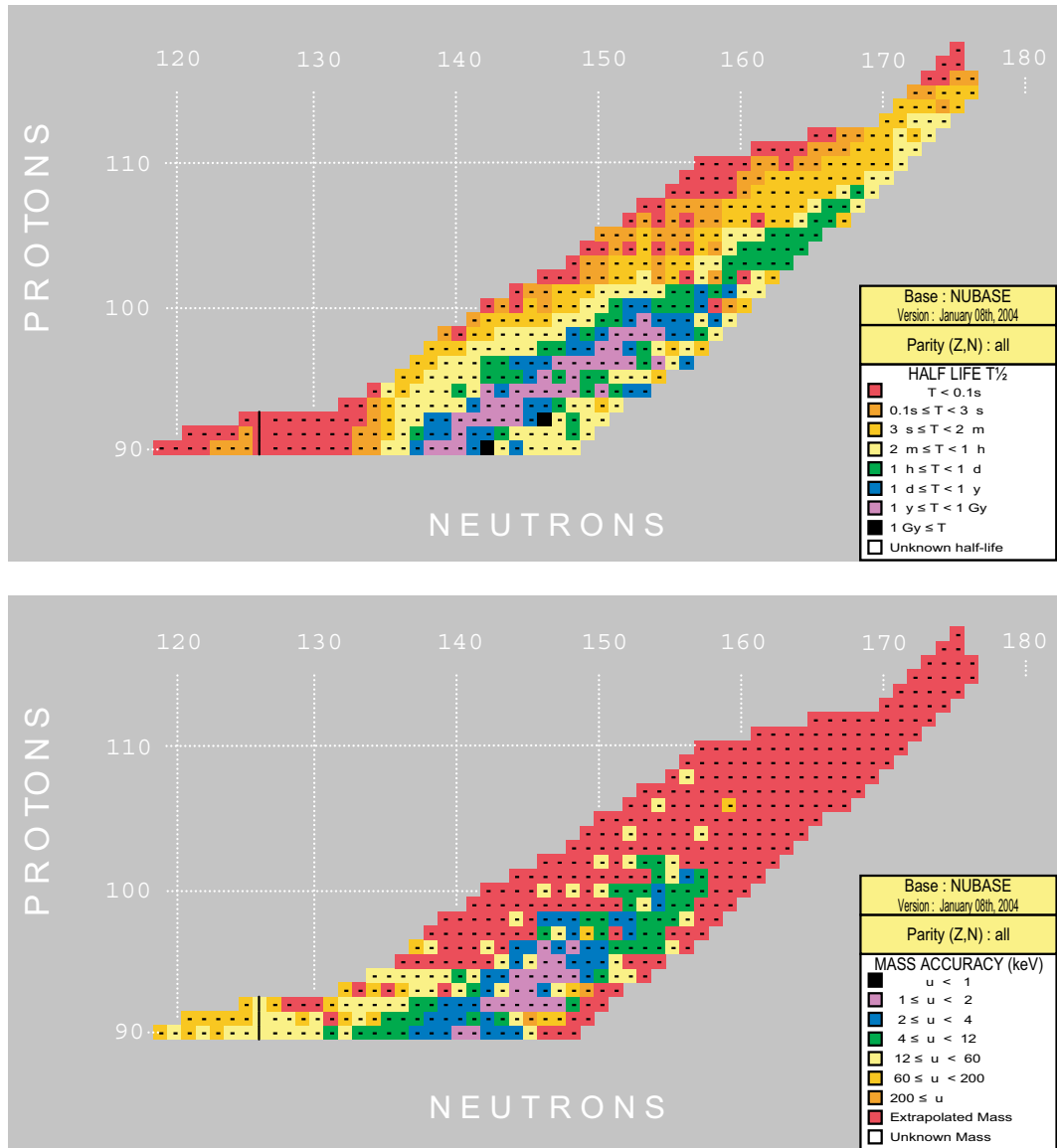
Figure 7.1: Transuranium region of the nuclear chart displayed in a color code according to half-lives (top) and mass accuracy (bottom). Contents of NUBASE [1], http://amdc.in2p3.fr/web/nubdisp_en.html

Table 7.1: Properties of transuranium nuclides between nobelium ($Z = 102$) and dubnium ($Z = 105$) and the respective fusion reaction for their production. The data for the half-lives and excitation energies are taken from the NUBASE [1] compilation. Only known isomers with half-lives $T_{1/2} > 10$ ms are considered. The value of the mass uncertainty was taken from the AME2003 [98]. The sign $\#$ indicates values that are derived from the extrapolation of systematic experimental trends. The listed cross sections are the peak values where the excitation functions are experimentally determined [37].

Nuclide	$T_{1/2}$ (g.s.)/ keV	δm / keV	$\mathbf{E}$(i.s.)/ keV	Reaction	σ/ nb
^{252}No	2.44 s	13		^{208}Pb(^{48}Ca, 4n)	220
^{253}No	1.62 min	100#		^{208}Pb(^{48}Ca, 3n)	1
^{254}No	51 s	18	1293	^{208}Pb(^{48}Ca, 2n)	2200
^{255}No	3.1 min	10		^{208}Pb(^{48}Ca, 1n)	140
^{255}Lr	22 s	210#		^{209}Bi(^{48}Ca, 2n)	200
^{255}Rf	1.64 s	180#	80#	^{207}Pb(^{50}Ti, 2n)	12
^{257}Rf	4.7 s	100#	114	^{208}Pb(^{50}Ti, 1n)	10
^{256}Db	1.9 s	290#		^{209}Bi(^{48}Ti, 3n)	0.19
^{257}Db	1.53 s	230#	100#	^{209}Bi(^{48}Ti, 2n)	2.4
^{258}Db	4.5 s	340#	60#	^{208}Bi(^{48}Ti, 1n)	4.3

in-flight by the velocity filter SHIP (see Sec. 3.2.1) and which are produced in most of the cases with cross sections well below one μb. Table 7.1 gives some examples.

As an extreme case the one neutron evaporation reaction for the production of the element 112[1] is given as an example

$$^{70}\text{Zn} + ^{208}\text{Pb} \longrightarrow ^{277}112 + 1\text{n} \,. \tag{7.1}$$
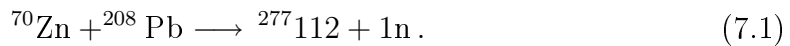
The cross section of this reaction was measured to be 1 pb [8], *i.e.* it has a production rate of two events in 24 days. The measured half-life for ^{277}112 of $T_{1/2} = 1.1$ ms is certainly to short to perform direct mass measurements but it is linked by α-decay chains to other species with longer half-lives, which enable a direct mass measurement, as *e.g.*, ^{269}Hs (7.1 s), ^{265}Sg (24.1 s), and ^{261}Rf (33 s) [8].

Of course not all reactions in this region are so scarce, but the example illustrates clearly that the species in this region have to be detected by a different technique in order to have a chance to perform a direct mass measurement. In Chap. 3 the non-destructive narrow-band FT-ICR detection technique is described and presented to be the suitable detection method for the study of these transuranium species. The combination of a tuned LC-circuit together with the well-known method of Fourier transformation of the image currents will enable single ion experiments. Figure 7.1 shows the nuclear chart with the nuclides sorted by color code indicating their half-life (top) and their mass accuracy (bottom). From uranium $Z = 92$ up to the heaviest known element, more than 200 nuclides are known to have a half-life longer than one minute. These relatively long-lived species will enable the use of the FT-ICR detection and as a consequence first direct mass measurements will be

---
[1]The element ^{277}112 represents the heaviest element produced by SHIP.
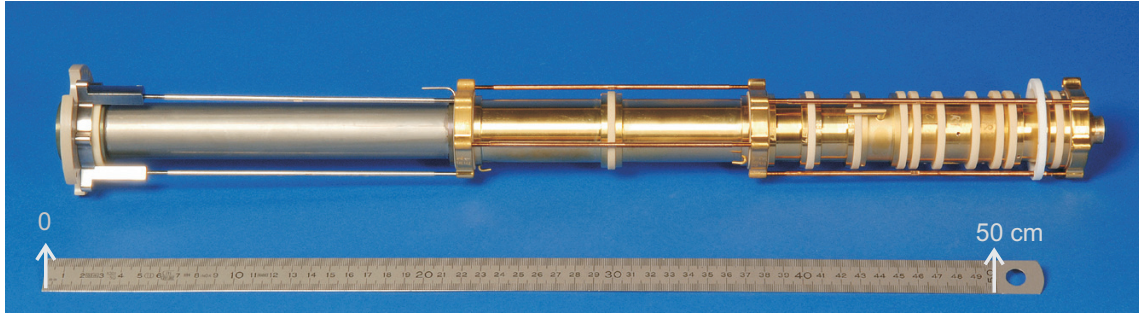
Figure 7.2: Purification trap section consisting of a seven-pole cylindrical Penning trap preceded by three entrance segments. The ions will enter from the left side. The last entrance endcap has a buffer-gas inlet and the last exit endcap segment has a funnel shape for the connection with the pumping barrier.

in reach. Experimental values will give the possibility to check mass models and mass formulas since most of the mass values in this region are only known indirectly or by extrapolations of α-decay chains [98]. One should note that the use of the destructive TOF-ICR technique will still give the possibility of investigating very short-lived species with cross sections above 1 μb.

7.2 The cryogenic Penning trap setup at Mainz

A number of requirements impost by the size of the achievable S/N ratio given by Eq. (4.16) have to be fulfilled in order to reach single-ion sensitivity. The design of the cryogenic narrow-band FT-ICR setup has been carried out within the thesis work of C. Weber [77]. Here, the installation, commissioning, and first results of testing different parts of the setup are presented. The setup consists of two Penning traps: The first is a cylindrical seven-pole *purification trap* (see Fig. 7.2), with the identical characteristic electrode geometry as in the present room-temperature setup of SHIPTRAP [84, 85] (see Chap. 5). In this trap, the ion beam is cooled and isobarically purified by means of buffer-gas cooling (Sec. 2.5). The three entrance drift electrodes are used to guide the ions into the trap. The trap itself has a four-fold asymmetrically segmented ring electrode[2] with a couple of internal and external correction electrodes between a pair of three-fold (entrance) and two-fold (exit) endcap electrodes. The entrance endcap contains the buffer gas inlet in the closest segment to the ring electrode. All electrodes in the 77-K region are made from high purity oxygen free electrolytic (OFE) copper to facilitate the thermal conductivity and hence to guarantee a homogeneous temperature in this region. To avoid thermal losses at the room temperature electrodes, the first and last electrodes are made from stainless-steel due to its reduced thermal conductivity. The use of OFE copper with high purity (99.99%) reduces the distortion of the homogeneity of the magnetic field produced by the magnetization of the impurities. In addition, all electrodes are gold plated to avoid oxidation on the surface that might distort the electrostatic trapping

---

[2]This segmentation allows for the sensitive detection of image currents by a broad-band FT-ICR detection that will be implemented in the future.

Figure 7.3: High-precision hyperbolical Penning trap for the cyclotron frequency determination. It is specially designed to improve the detection of the induced image currents (see text for more detatails).

potential (see Fig. B.1 in Appendix B).

In the second Penning trap the cyclotron frequency measurement is performed and it is thus called *measurement trap* (see Fig. 7.3). In the design of this trap special attention was given to optimize the signal-to-noise ratio to obtain the necessary single ion sensitivity. It consists of a hyperbolically shaped electrode configuration[3]. The use of hyperbolical electrodes ensures a high harmonic potential even in regions far off the center of the trap, which is in general impossible for a cylindrical trap of these dimensions. The orthogonalization of the electrode configuration, which follows the relation $\rho_0 \approx 1.16\, z_0$ [112], allows to keep the eigenfrequencies independent of their motional amplitudes. The endcaps are symmetrically two-fold segmented and the ring electrode is asymmetrically four-fold segmented ($40° - 140° - 40° - 140°$). At the small segments the rf field for the excitation of the ion motion is applied while the bigger ones are used for the detection of the induced image currents. The whole setup is illustrated in Fig. 7.4.

Both traps are placed 20 cm apart from each other in the bore of a superconducting magnet of 7 T magnetic field strength. The measurement trap is situated in the very homogeneous region $\Delta B/B = 2 \cdot 10^{-6}$ of the magnetic field[4] (see Fig. 7.5). Both traps are separated by a 47 mm long channel of 2 mm diameter, which acts as a differential pumping barrier for the suppression of the high pressure conditions in the measurement trap due to the application of buffer gas cooling in the purifi-

---

[3]For dimensions of the measurement trap refer to [77].

[4]This value corresponds to the peak-to-peak homogeneity in a cylinder of 2 cm radius and 3 cm length.
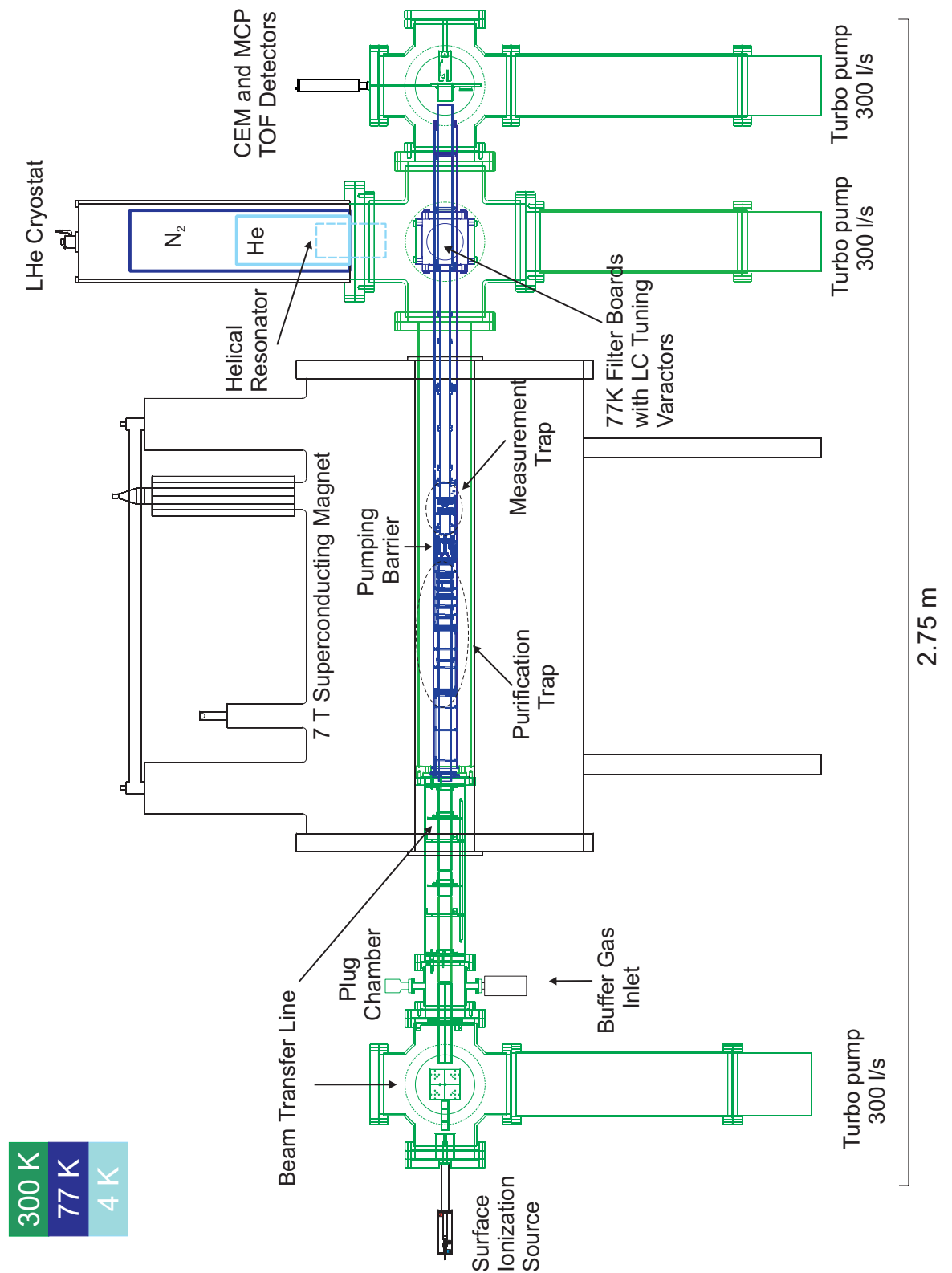
Figure 7.4: Sketch of the cryogenic Penning trap setup for SHIPTRAP adapted for first off-line tests at the University of Mainz.
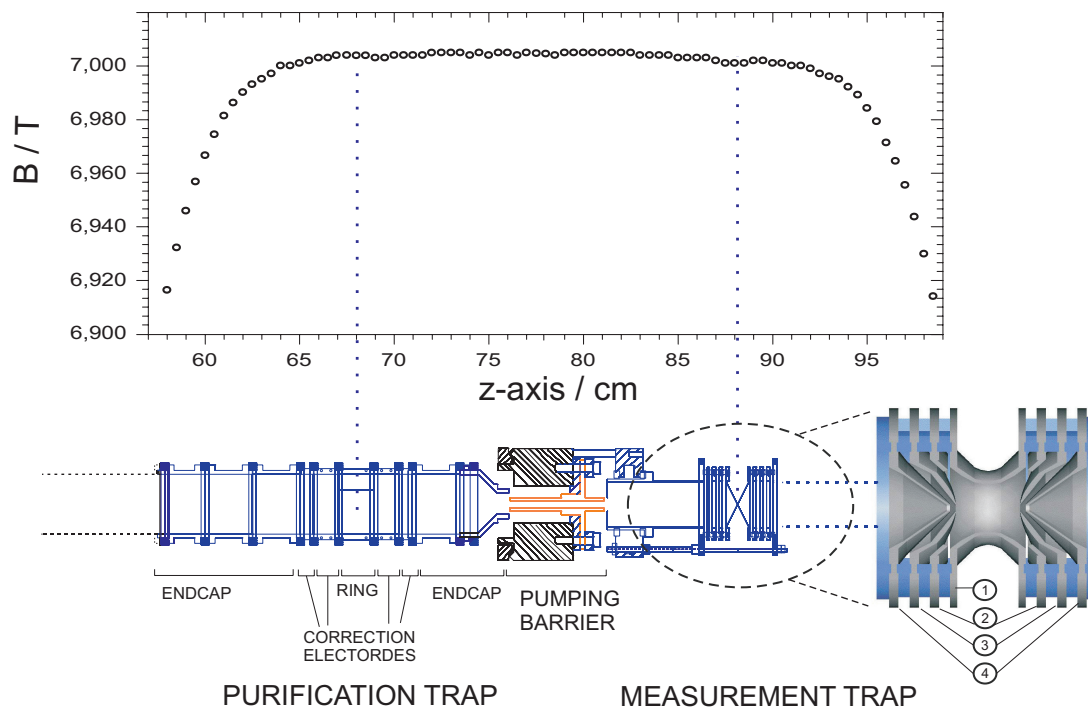
Figure 7.5: Schematic drawing of both traps and their location with respect to the magnetic field at Mainz. For both traps, connected by the pumping barrier, the function of their respective electrode is assigned. A zoom of the measurement trap shows a cutaway view with: ring electrode (1), endcaps (3), and the respective correction electrodes (2) and (4).

cation trap. As mentioned above, the test of the cryogenic setup is carried out in a superconducting magnet with a different field geometry compared to the one used at SHIPTRAP. It has only one homogeneous region, but with an almost identical magnetic field strength of 7 T.

For the commissioning of the setup cesium ions are produced via surface ionization (see left flange of the first CF150 double cross in Fig. 7.4) and guided towards the entrance of the purification trap section by several Einzel lenses and quadrupolar deflectors. At the top of the CF200 double cross a cryostat is located, which houses the superconducting coil for the FT-ICR detection and a first amplification stage at liquid helium (LHe) temperature (4.2 K). A set of drift electrodes follow the measurement trap to guide and focus the ions onto a secondary electron multiplier in order to measure the time of flight. A linear feedthrough is installed to enable the exchange of the channeltron by a MCP detector in case of failure during on-line measurements. For a detailed description of this detector setup see Sec. 7.4. The trap environment is held at 77-K temperature by the use of a double-wall tube filled with liquid nitrogen (LN_2), which is put in contact with the inner region through a 1 mm thickn copper tube and isolated from the exterior by means of a vacuum region, similar to a conventional dewar. The nitrogen is supplied via a connection with the LN_2 reservoir of the He cryostat. This trap vacuum tube made out of copper is at the entrance and exit side formed by stainless-steel segments. The one at the exit side, in the form of a bellow, accounts for the thermal shrinking when cooling down

the system. The trap vacuum tube is intersected by a stainless-steel cube-shaped vacuum chamber with four CF60 flanges, which provide the necessary feedthroughs for the connection of the trap electrodes and drift segments through the temperature and pressure transition between both regions. Two filter boards are placed on two opposite sides of the cube and connected via SubD15 feedthroughs. The room given to the superconducting coil as well as the one employed for the isolation of the LN_2 in the trap tube are connected and evacuated by a turbo pump with 300 l/s pumping speed (EBARA ET300WS) placed on the lower side of the CF200 cross. Two more pumps of the same type provide the vacuum in the trap tube volume at both sides of the pumping barrier.

7.3   The differential pumping barrier

The differential pumping barrier between purification and precision trap is necessary in order to ensure the different pressure conditions that are required for the operation of each trap. In the purification trap the ion beam must be cooled and isobarically cleaned by means of a buffer-gas cooling scheme under the presence of He ($p \approx 10^{-5}$ mbar) [47]. Ultra-high vacuum during the mass determination with pressures of $p < 10^{-8}$ mbar is required in order to avoid collisional damping of the ion motion while the excitation or sampling period in TOF-ICR or FT-ICR takes place. To this end, a differential pumping barrier with a high suppression factor is required. Therefore, a detailed study of the gas flow through a channel of different diameters was performed. Here the holder of this channel is sealed with different materials and tested at room (300 K) and LN_2 (77 K) temperatures.

7.3.1   Theoretical gas flow studies

The most important types of vacuum according to the flow established in their presence are the rough vacuum, the fine vacuum, and the high vacuum. The flow regime in each of these types of vacuum is characterized by the ratio of the mean free path λ of the gas molecules to the width d of the flow channel, *i.e.* by means of the so-called Knudsen-number

$$Kn = \frac{\lambda}{d}. \tag{7.2}$$

In the rough vacuum $Kn \ll 1$. Under these conditions the gas particles collide with each other very often and the gas can be considered as a continuum. In this scenario a viscous flow is established which can either be a laminar or a turbulent flow. In the first case the gas particles move in layers while in the second case the movement is disordered.

In the high vacuum regime ($Kn > 0.5$) the gas molecules are totally independent on each other. The probability that one particle hits another is so small that practically all collisions of the gas molecules will be with the inner walls of the gas container. In this case the flow is called molecular flow and is the one of concern for our studies. The fine vacuum corresponds to the regime between the two mentioned before.

In the region of high vacuum, under molecular flow, the movement of the particles can be described without consideration of the other particles. Each particle will follow a straight path until it hits a wall, so the trajectories can be easily calculated.
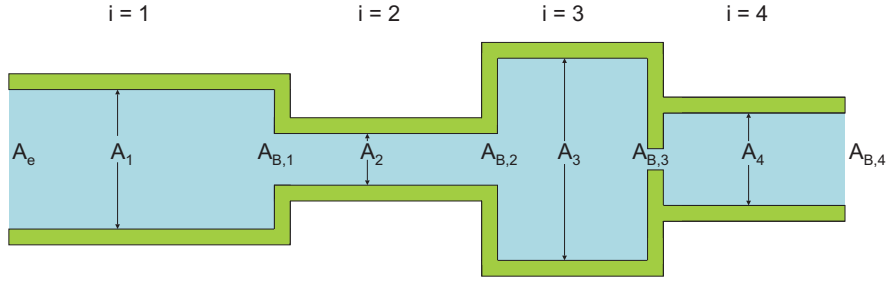
Figure 7.6: Schematic layout of connected vacuum components for the calculation of the transition probability T_{tot}.

The reflection at the walls can be described by a cosine law. Thus, the gas flow q_2 leaving one end of the tube is equivalent to the gas flow q_1 entering the tube multiplied by the transition probability T through the tube

$$q_2 = q_1 \cdot T \,. \tag{7.3}$$

In order to have a flux q passing through a tube, a pressure difference Δp has to be present between both sides of tube. The ratio of both magnitudes defines the flow resistance W of a tube and in analogy to the electrical flow, the reciprocal is called conductance

$$L = \frac{1}{W} = \frac{q}{\Delta p}. \tag{7.4}$$

The relation between the conductance L and the transition probability T is given by [113]

$$L = \frac{\bar{v}}{4} A \cdot T \,, \tag{7.5}$$

where $\bar{v}$ is the mean velocity of the gas particles at a constant temperature, which can be calculated from the Maxwell-Boltzmann distribution, and A is the surface cross section of the entrance tube.

For the calculation of the transition probability of connected vacuum components (see Fig. 7.6) in the regime of molecular flow, the resistances of the individual segments cannot be added to each other, as in the case of electrical currents. In this case, a more complex calculation leads to the formula for the total transition probability [113]

$$T_{tot}^{-1} = 1 + \sum_{1}^{n} \frac{A_e}{A_i} \left[\left(T_i^{-1} - 1 \right) + \left(a_i^{-1} - 1 \right) \right] \,, \tag{7.6}$$

where A_e is the surface cross section of the entrance, A_i is the one of the *ith* tube, T_i is the transition probability of the *ith* tube, and $a_i = A_{B,i}/A_i$ is the transition probability through the slit with the cross section $A_{B,i}$ following the *ith* tube. For the theoretical calculation of the differential pumping the value of T_{tot} and L are taken from a gas flow simulation program based on Monte-Carlo calculations.

Vacuum pumps are mainly characterized by their pumping speed S and their throughput $\dot{Q}$. The pumping speed denotes the volume current at the intake socket.
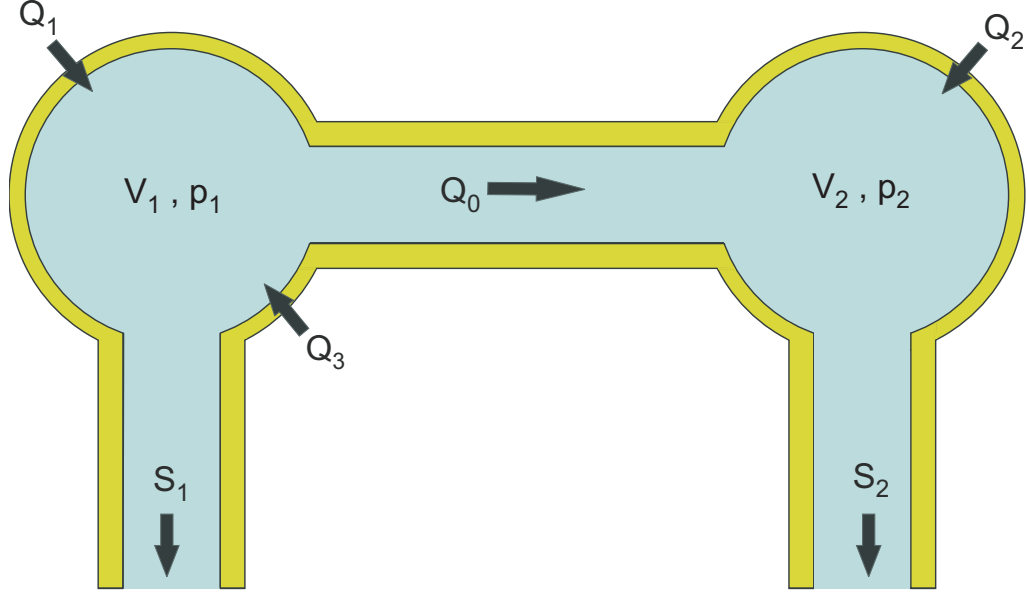
Figure 7.7: Schematic view of the setup for the deduction of the differential pumping through the pumping barrier. All parameters considered in the calculations are indicated. For more details see text.

It depends on the type of gas being evacuated and is constant for most pumps in a large interval of pressures. The throughput is defined as:

$$\dot{Q} = (p\dot{V})_{int.\,socket} = p \cdot S \,, \tag{7.7}$$

and decreases at lower pressures since less gas particles are in one unit volume.

A simplified picture of the experimental setup, shown in Fig. 7.4, is illustrated in Fig. 7.7. Here, all parameters entering in the theoretical description are indicated. V_1 (p_1) and V_2 (p_2) are the volumes (pressures) of the two different chambers and S_1 and S_2 are the pumping speeds, respectively. Q_0 is the gas flow through the pumping barrier, which is the parameter of interest. Q_1 and Q_2 are the outgasing rates and Q_3 is the flux of helium injected into the system to study its diffusion through the channel.

The behavior of the pressures can be described by the following set of differential equations [114]:

$$V_1 \frac{dp_1}{dt} + S_1 p_1 + L(p_1 - p_2) = Q_1 + Q_3 \tag{7.8}$$

$$V_2 \frac{dp_2}{dt} + S_2 p_2 = Q_0 + Q_2 \tag{7.9}$$

$$Q_0 = L(p_1 - p_2) \,. \tag{7.10}$$

Since we do not have information about the outgasing rates Q_1 and Q_2, we will use the initial pressures p_1^0 and p_2^0 to compensate for that and modify Eqs. (7.8-7.10) accordingly. Considering only static processes, we obtain from Eq. (7.9)

$$S_2(p_2 - p_2^0) = L(p_1 - p_0) - L(p_2 - p_2^0), \tag{7.11}$$
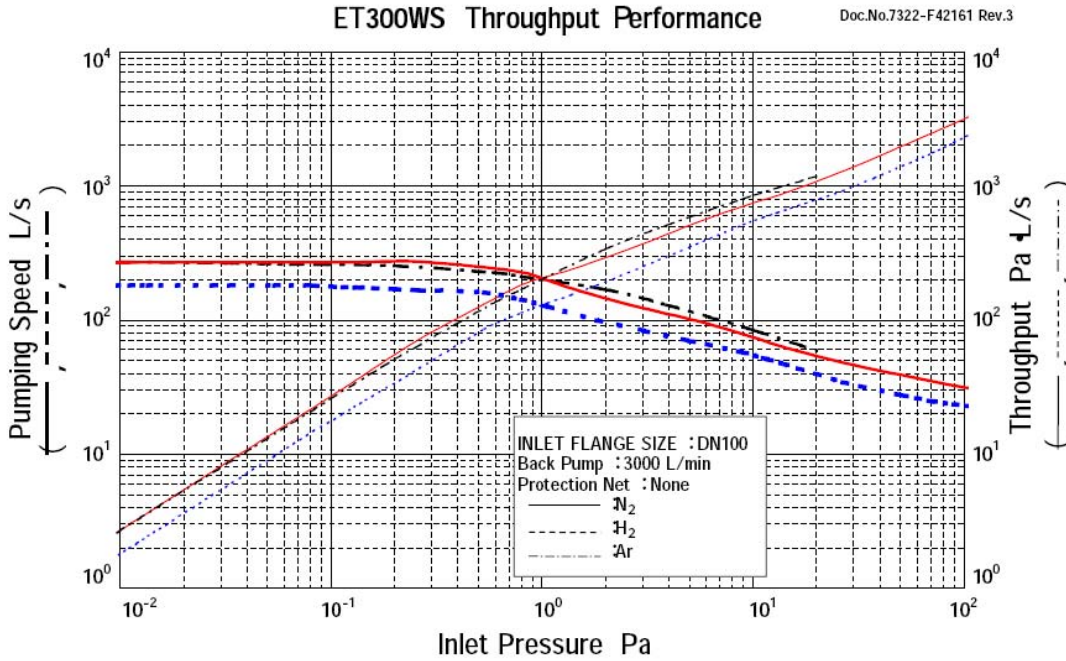
Figure 7.8: Pumping speed and throughput of EBARA ET300WS turbo pumps for different gases [115]. In our calculations the curve corresponding to hydrogen is used for helium in good approximation due to its similar mass.

from which the pressure ratio is calculated

$$\frac{p_1}{p_2} = \left(\frac{S_2}{L} + 1\right) + \frac{1}{p_2}\left(p_1^0 - p_2^0 - \frac{S_2}{L}p_2^0\right) . \tag{7.12}$$

The second term represents a correction for lower pressures p_2. Thus, the ratio p_1/p_2 saturates for high flow rates Q_3 or equivalently for high pressures p_2 (low suppression factor). Taking into account the experimental performance of the measurement devices employed in our setup, like the pumping performance and the mass dependent uncertainty of the gauges, the last equation has still to be modified in order to describe the real behavior of the gas flow: The assumption of a constant pumping speed S in the deduction of Eq. (7.11) is not realistic due to the range of pressures covered in our tests. In particular for p_1, which ranges from 10^{-8} to 10^{-2} mbar, the pumping speed is not constant in all interval. Considering the similar mass between helium and hydrogen, one can use the curves illustrated in Fig. 7.8 as an approximation for the pumping speed. Accordingly, a correction factor

$$k_1 = \frac{S_1(p_1^0)}{S_1(p_1)} , \tag{7.13}$$

has to be included in Eq. (7.12).

A further correction accounts for the different sensitivity of the Penning gauges to the kind of gas being detected. Thus, the initial pressures p_1^0 and p_2^0 of the rest gas mainly correspond to the detection of molecular hydrogen H_2 and therefore the

sensitivity of the vacuum gauges has to be corrected as well, *i.e.*, the read out of the pressure controller has to be multiplied by 2.44, which is the correction factor corresponding to H_2. In the same way, the pressure p_1 is determined by the injected helium gas in the system and the read-out pressure has to be corrected by a factor 7.1. The pressure p_2 is a mixture of rest gas (H_2) and the diffused helium through the pumping barrier. Then, the correction factor k_2 for the pressure p_2 will be given by

$$k_2 = \frac{2.44 p_2 + 7.1(p_2 - p_2^0)}{p_2} \, . \tag{7.14}$$

After including the correction factors, the theoretical description of the pressure ratio in the two volumes connected by the pumping barrier is given by

$$\frac{p_1}{p_2} = k_1 \frac{S_2}{L} \left(1 - \frac{2.44 p_2^0}{k_2 p_2} \right) + \left(1 + \frac{2.44(p_1^0 - p_2^0)}{k_2 p_2} \right) \, . \tag{7.15}$$

7.3.2   Comparison with experimental results

The experimental results from the study of the gas diffusion through the pumping barrier were obtained after a number of measurements using three different channel diameters and are described in the Diploma thesis of D. Neidherr [114]. The pressure ratios between the two volumes were recorded by active-Penning gauges (BOC Edwards-AIM-X) in a pressure range of $p = 10^{-2}$ to 10^{-9} mbar, at room temperature as well as 77 K, for different flow rates of helium gas injected into the system via a gas-flow regulator valve (Pfeiffer-RVC300). The pumping barrier (see Fig. 7.9) consists of a cylindrical holder made from OFE copper with a bore in the center in order to mount the different channels. A threaded ring to the holder is used to press and confine a sealing fixing the whole array within the vacuum tube (see Fig. B.2).

Figure 7.10 shows the results of the pressure ratio p_1/p_2 between the purification and precision trap as a function of the gas inlet flow for a series of measurements in which no pumping barrier is used or three different channels with 1.5, 2, and 3 mm diameter are tested. The theoretical data points are obtained from Eq. (7.15) when using the results of the Monte-Carlo simulations for the transition probability T and the conductance L of the different channel diameters. These results are summarized in Tab. 7.2. The channels are attached to the holder of the pumping barrier using a Viton™ ring as a sealing. The error bars for the theoretical results

Table 7.2: Transmission probability T and the conductance L obtained by simulations based on Monte-Carlo calculations.

Channel diameter	T	δT	L (l/s)	δL (l/s)
no pumping barrier	$5 \cdot 10^{-2}$	$7 \cdot 10^{-5}$	44.02	$6 \cdot 10^{-2}$
3 mm	$18 \cdot 10^{-5}$	$1.3 \cdot 10^{-5}$	0.16	$1.0 \cdot 10^{-2}$
2 mm	$50 \cdot 10^{-6}$	$2.2 \cdot 10^{-6}$	0.043	$2 \cdot 10^{-3}$
1.5 mm	$2 \cdot 10^{-5}$	$1.6 \cdot 10^{-6}$	0.0022	$1.4 \cdot 10^{-3}$

as well as for the experimental data points are obtained by error propagation of the individual parameters entering in the mathematical expression of the pressure ratio
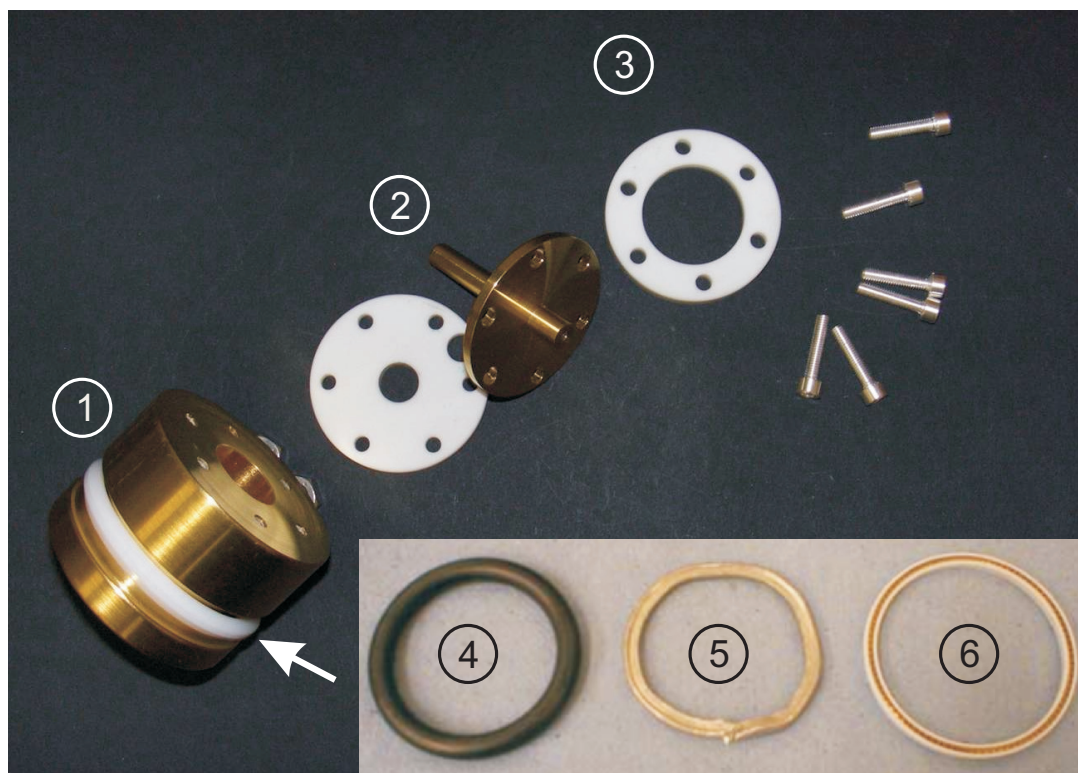
Figure 7.9: Pumping barrier elements. (1) Channel holder and support ring with Teflon™ sealing, (2) channel with 2 mm diameter used for our tests, (3) Macor™ discs for the electrical insulation of the channel with respect to the holder, (4,5,6) Viton™ indium, and Turcon™ sealings, respectively. The different sealings were installed at the position indicated by the arrow.

(see Appendix A). The error assigned to the experimental pressures is 10% of the readout value. The results show very good agreement between experimental and theoretical data. In the low pressure regime (low flows) the theoretical curves result in slightly higher pressure ratios, which could be explained by microscopic effects not taken into account in the theoretical derivation, as *e.g.* the atomic interaction of the gas with the tube walls, which might decrease the conductance. In general, the results demonstrate a good understanding of the differential pumping process. In the present SHIPTRAP setup a 3 mm-diameter channel attached mechanically to the trap tube is used. The suppression factor for the typical operation pressure in the purification trap of $p = 10^{-4} - 10^{-5}$ mbar was determined to be in the order of 60. The use of a pumping barrier as tested here having a 1.5 mm channel will result in an improvement of a factor of about 100, *i.e.*, a suppression factor of 6000 between purification and precision trap.

However, in our setup the traps are cooled to 77 K temperature. When cooling down from room temperature to LN_2 temperature the measured suppression factor decreases dramatically due to the thermal contraction of the Viton™sealing ring ($\alpha = 13 \cdot 10^{-5}$ K^{-1}) or alternatively of the Teflon™ring ($\alpha = 5 \cdot 10^{-5}$ K^{-1}), also tested in these measurements. At this lower temperature the gas diffusion is no longer only through the channel but also through the edges of the pumping barrier
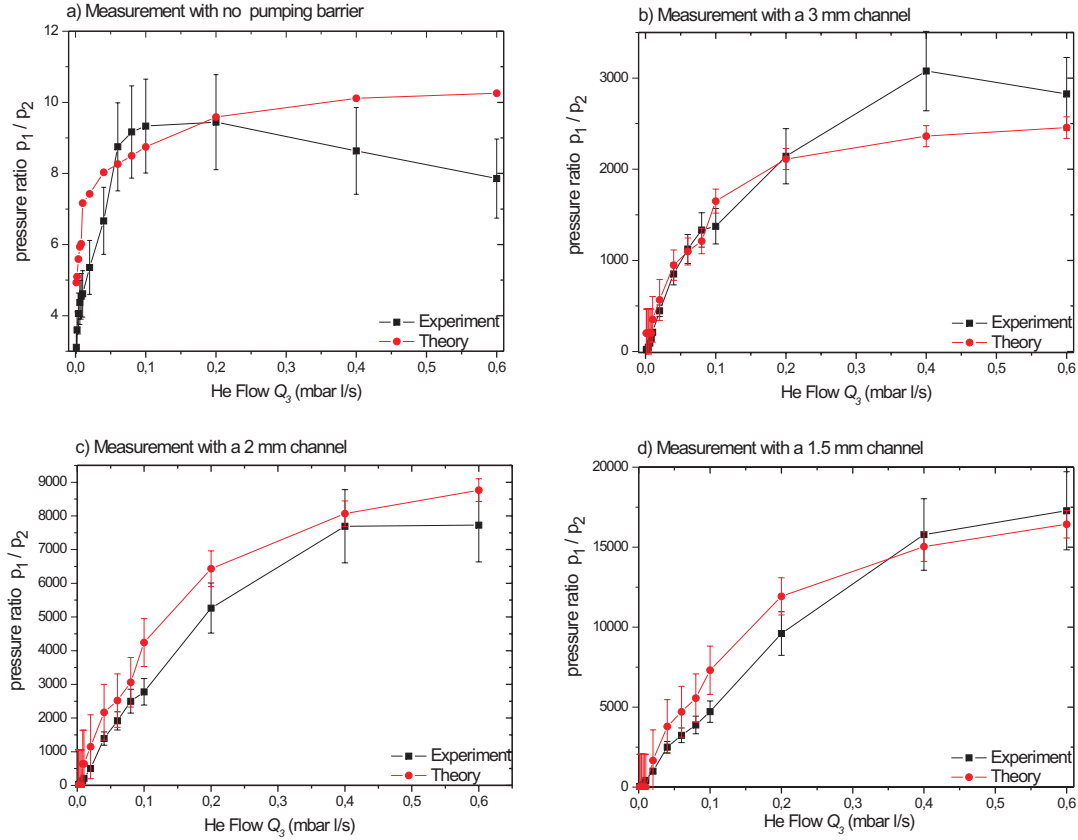
Figure 7.10: Results of the differential pumping tests at room temperature, see also [114]. (a) no pumping barrier, (b) 3 mm , (c) 2 mm, and (d) 1.5 mm diameter channel. The pressure ratios (circles) are calculated using Eq. (7.15).

since the sealing material does not efficiently seal the barrier against the wall. For that reason, further tests have been performed in order to improve the sealing of the pumping barrier at cryogenic temperatures. Several measurements were performed using different materials of the sealing ring (see Fig. 7.9).

After the insufficient results obtained with Viton™and Teflon™(see Fig. 7.11), a new design of the holder was used in combination with a sealing made from indium. Here the results were much better due in part to its lower thermal contraction ($\alpha = 2.5 \cdot 10^{-5}$ K^{-1}) and to its malleability, that makes it a very good sealing material even at LN$_2$ temperature. However, it is an extremely soft metal and the sealing ring gets destroyed after each dismantling of the traps. Moreover, indium sticks to the walls of the vacuum tube and can be hardly removed.

In the next attempt a commercial sealing from Turcon™ Variseal was tested. This sealing consists of a Teflon shield covering a ring shaped spring that counteracts the thermal contraction by mechanical expansion. In this case the sealing is not pressed against the trap tube. That is the reason why it gives the worst results at room temperature. However, a special design of the holder makes the sealing to expand in order to press efficiently the pumping barrier edges against the trap tube at 77 K. Consequently, the Turcon™ sealing gives the best results in all pressure ranges at cryogenic temperatures. Focusing on the flow interval ranging from 0.001 to 0.06
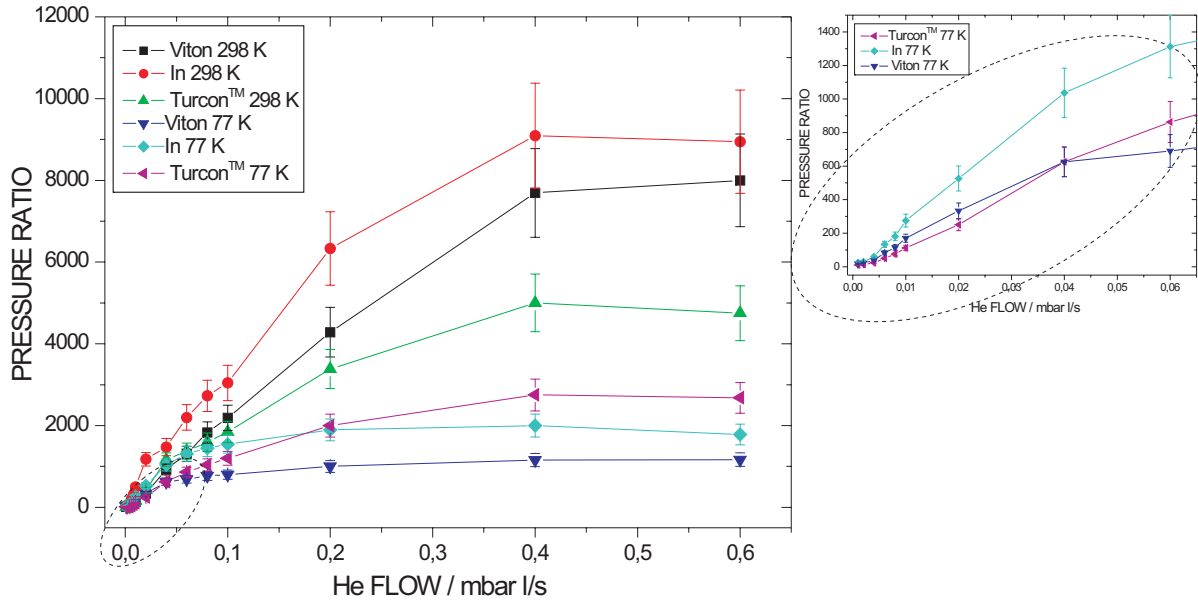
Figure 7.11: Differential pumping test at room temperature and at 77 K with a 2 mm diameter channel for different sealing materials. The plot at the right hand side shows a zoom on the pressure ratios of relevance in the buffer gas cooling technique.

mbar l/s (see Fig. 7.11 (right)) corresponding to the typical pressures (10^{-4} to 10^{-5} mbar) used in the purification trap for buffer gas cooling, it seems that indium or even Viton™ show better results than Turcon™. The reason for that is that in the pressure ratio comparison shown in Fig. 7.11, not all initial pressures p_2^0 (initial pressure in the measurement trap side) are the same. What is important in these measurements of the differential pumping is to preserve the high vacuum in the measurement trap while increasing the pressure at the other side of the pumping barrier.

Taking into consideration the initial pressures, Turcon™ gives the highest differential pumping rate. To check this, in Fig. 7.12 the different pressures measured in the two regions for indium and Turcon™ (from which the ratio is taken in Fig. 7.11) are represented. One can see that for the flows injected in the purification trap volume, which produce a pressure interval $\Delta p_1 = 10^{-6} - 10^{-2}$ mbar in the purification trap, the net increment $\Delta p_2 = p_2 - p_2^0$ of pressure in the measurement trap is minimal for the Turcon™ sealing and only $2.5 \cdot 10^{-6}$ mbar, compared to $4 \cdot 10^{-6}$ mbar for indium[5]. In view of the last results, a suppression factor of 10^3 while buffer gas cooling is still possible for the new cryogenic setup provided by a pumping barrier with a 2 mm-diameter channel and a Turcon™ ring as a sealing. This result improves the actual suppression factor in the room temperature setup by a factor of 20. The use of a 1.5 mm-diameter channel would increase the differential pumping by another factor of two.

---

[5]Even when indium seems a very good sealing for low pressures, one should consider the disadvantages of its use, regarding the difficulties of removing the traces of the soft metal.
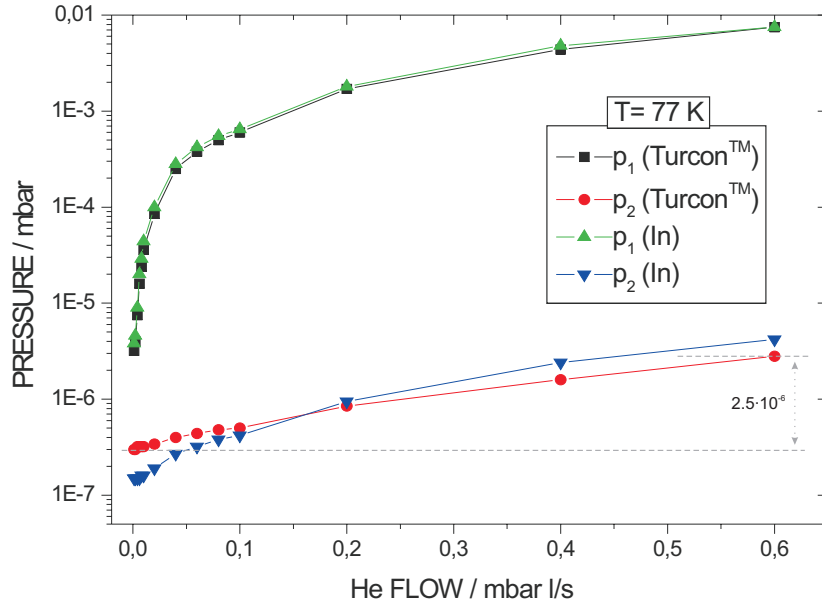
Figure 7.12: Evolution of the pressure in the purification (p_1) and measurement (p_2) trap regions as a function of the injected gas flow. The performance of indium and Turcon™ sealings at 77 K temperature is shown in which the latter gives a smaller net pressure increment of $2.5 \cdot 10^{-6}$ mbar in the measurement trap side for the complete interval of flow injected in the purification trap side. The pressure ratio p_1/p_2 in Fig. 7.11 is taken from such a measurement.

7.4   Comparison of the detector efficiencies

In this section the investigation of the relative detection efficiency of microchannel plate detectors (MCP) compared to channel electron multipliers (CEM), also known as channeltrons, is addressed. As was already stated before (see Sec. 4.1.1), MCPs are the detectors of choice in mass spectrometry on radionuclides in combination with the TOF-ICR detection technique, as *e.g.* it is the case at SHIPTRAP. Taking into account the ion energies at the SHIPTRAP mass spectrometer, which are in the order of 2 keV, the resulting detection efficiency with the MCP in use is in the order of 30% (see Fig. 4.3). Since such a detection efficiency is a severe limitation in studying exotic species far from stability, which are produced in rare amounts, a new detection scheme based on a channeltron with a conversion dynode is proposed. The dynode is used in order to convert the incoming positive ions into electrons with a conversion efficiency of practically 100%. The energy of these electrons can be easily tuned to be detected more efficiently by the channeltron. In that way the detection efficiency for ions can be increased by a factor of three compared to the microchannel plate detector.

In this work a study of the detection efficiency of a MCP and a channeltron, for the typical ion energies employed at SHIPTRAP, was carried out with a dedicated test setup, which is schematically shown in Fig. 7.13. The main purpose of this setup was to prepare an ion beam under identical conditions in order to achieve a realistic, direct comparison of both detector efficiencies. In the setup, ions can be created by two different ion sources: a surface ionization source (A) and an electron impact
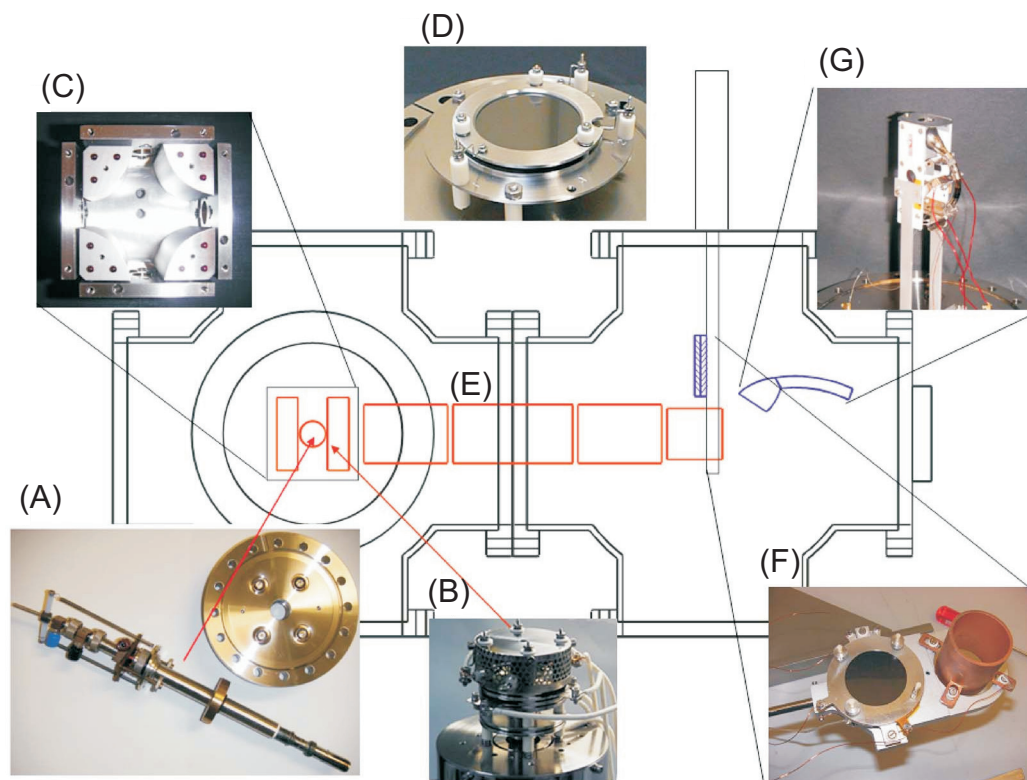
Figure 7.13: Test setup for the determination of the relative detection efficiencies of a MCP compared to a CEM detector. Shown are: the two different ion sources; a surface ionization source (A) and an electron impact ion source (B), the 90° bender (C), a first MCP for ion monitoring (D) and an Einzel lens (E) for guiding and focusing the ion beam on the test MCP (F) and the channeltron (G) detectors.

ion source (B). The ions are deflected by 90° employing a quadrupole deflector (C) and can be guided and focused with an electrostatic lens (E) towards the detectors. The MCP is mounted on a linear feedthrough (F). In this way the detectors can be quickly exchanged by removing the MCP from the beam line and allowing the ions to pass a short-drift tube towards the channeltron (G), which is placed behind in an off-axis configuration. A second MCP (D) is located opposite to the ion sources for beam monitoring and optimization of the 90° bending of the quadrupolar deflector. In order to find typical operation voltages, simulations were performed by using the SIMION 3D ion optics simulation program. A detailed description of the different parts of the setup as well as an optimized set of parameters to guide and focus the ions into the detectors are given in Appendix A.

Several series of measurements were performed with both ion sources for different ion energies[6], see as an example Fig. 7.14. Here, an ion beam of 60 eV energy was created by electron impact ionization of the rest gas. The beam was then bent by 90° and guided to the detector system. Measurements were taken for different voltages applied to the Einzel lens. At a certain voltage, the Einzel lens is exactly focusing the

---

[6]In these measurements even two different CEM detectors where tested obtaining almost identical results.
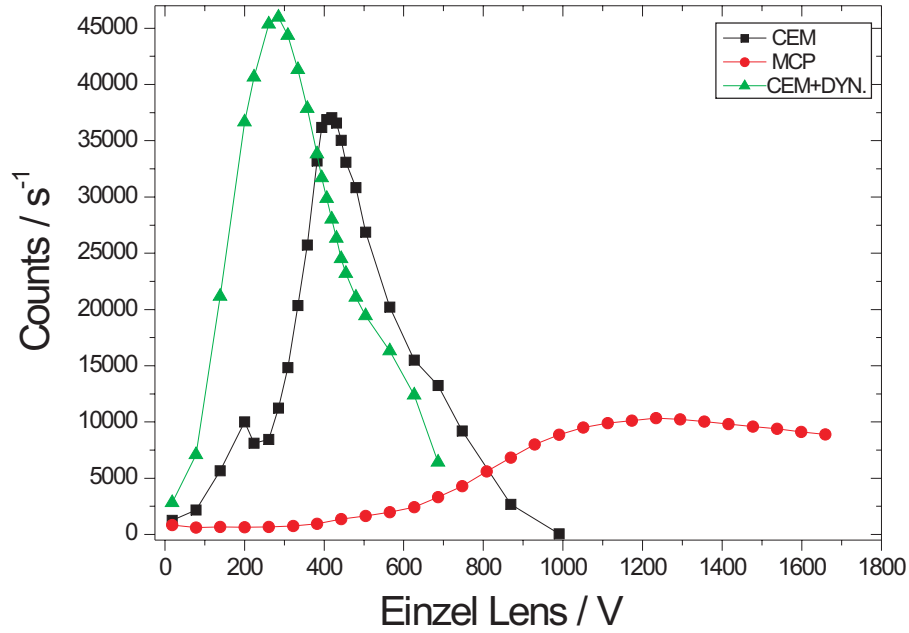
Figure 7.14: Number of counts as a function of the voltage applied to the Einzel lens, which is responsible for the focusing of the ion beam for the various detector configurations. Ions were detected in the channeltron (CEM), in the microchannel plate (MCP), and in the channeltron using in addition a conversion dynode (CEM+DYN). The operation voltages were: $V_{\mathrm{MCP}} = 2.1$ kV, $V_{\mathrm{CEM}} = 2$ kV, and $V_{\mathrm{DYN}} = 4$ kV.

ion beam on the detector and a maximum count rate in the detector is observed. This value is the one considered in the calculation of the maximum detection efficiency. Figure 7.14 shows the number of detected ions as a function of the applied Einzel lens voltage for three different detector configurations: a MCP and a channeltron, the latter with and without applying a voltage to the conversion dynode.

The different voltage settings for the maximum count rate and the different line shape of the curves result from the different axial positions and effective detection areas of the detectors, respectively. This measurement reveals a factor of up to 3.5 higher detection efficiency of the CEM compared to the MCP. Between CEM with and without conversion dynode there is a factor 1.2, possibly due to the higher detection efficiency exhibited by the CEM when detecting electrons of energy 1.9 keV (see Fig. 4.7) compared to ions at 2 keV. Another source of uncertainty to take into account in all measurements is the setting of the discrimination level. Prior to each measurement, the detector signal was triggered externally in order to see the detected ions in a time window of about 0.1 to 1 ms. Thus, one could decide what signals belong to real ions by their higher amplitude as compared to the background noise. Assuming an absolute detection efficiency of 90% for the channeltron while detecting electrons at 1.9 keV, as given in the technical specifications in Fig. 4.7, an absolute detection efficiency of 75% and of 25% for the ion detection using a CEM and a MCP, respectively, can be derived, which is in good agreement with the values given in Sec. 4.1.1 in Figs. 4.3 and 4.7.

In order to verify the higher efficiency of the CEM as compared to the MCP
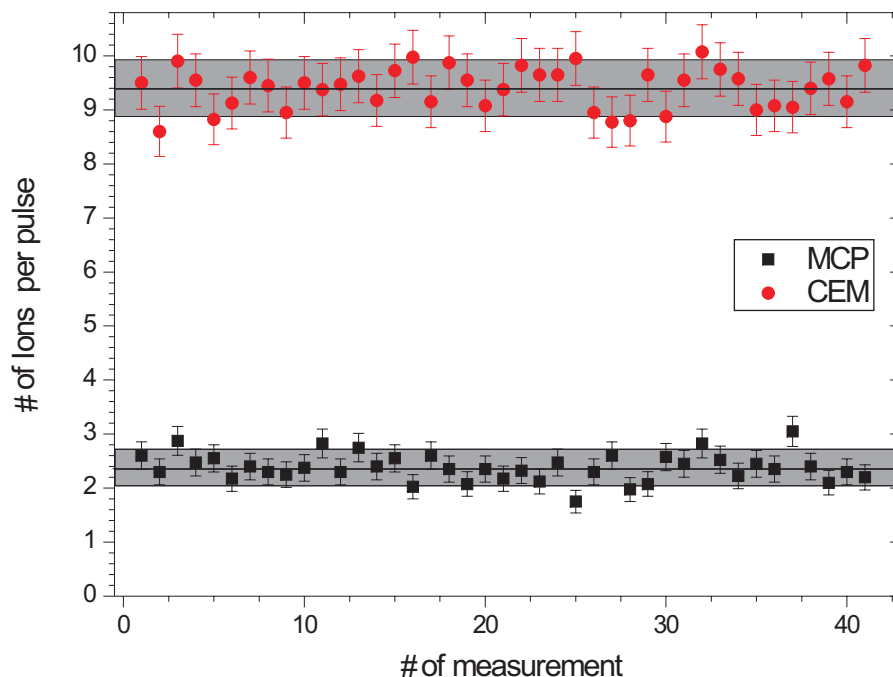
Figure 7.15: Relative detection efficiency of MCP and CEM using a pulsed beam. Each measurement represents the mean value of the number of ions detected in 40 pulses of 2 ms duration. The length of the pulse was selected in order to detect about 10 ions in average with the CEM.

detector, we performed several measurement with increased statistics. For this measurement the beam was pulsed by applying a voltage to the quadrupolar deflector with a pulse length of ($\sim$ 2 ms) in which 10 ions were detected in average by the CEM. Each point in Fig. 7.15 represents the mean value of the number of ions detected in 40 pulses. Here, the detection efficiency of the CEM is a factor of 3.9 larger as compared to that of the MCP. From this result one can again derive a 20-25% absolute detection efficiency for the MCP, according to the absolute efficiency of the CEM found in the former measurement. That turns out to be a bit lower than the results of [116, 117], where an absolute detection efficiency for the MCP ranging from 30% to 35% is reported. One reason might be that the discrimination level set for this measurement might have been a little bit too high.

To summarize the results that were obtained, the replacement of the commonly used MCP detector by a CEM is more than justified considering the range of energies with which ions are usually detected. The use of a CEM with a conversion dynode might well reach the 100% detection efficiency, independent of the energy of the ion beam, allowing for higher statistics and a significant reduction in the mass uncertainty and/or the measurement time. Thus, the investigation of radionuclides with the TOF-ICR detection technique can exploits this higher efficiency in order to address regions of more exotic species.

7.5   Characterization of the FT-ICR detection system

The expected single-ion sensitivity with the FT-ICR detection technique is based on the ability of the detection LC circuit to produce a measurable voltage drop as response to the tiny image current induced for a single ion on the two opposite segments of the ring electrode. As already discussed in Sec. 4.2.1, this feature of the resonant circuit is given by the quality factor, *i.e.* Q-value of the circuit, which is proportional to the resistance seen by the ion and thus, when having a high value, produces a voltage drop suitable to be detected. In order to reach high Q-values, the detection inductance is built as a helical resonator (see Fig. 7.16), which consists of a coaxial shield and a helical inner conductor. The latter is formed as a cylindrical single-layer air-core coil with a primary winding as the detection inductance, including a center tap to apply the DC voltage to the segments of the ring electrode, and a secondary winding to couple out the signal, as illustrated in Fig. 7.17. The windings are made from niobium-titanium (NbTi) superconducting wire, which has its transition temperature at 9.3 K and is hence cryogenically cooled to LHe temperatures (4.2 K). The output signal of the detection circuit needs to be
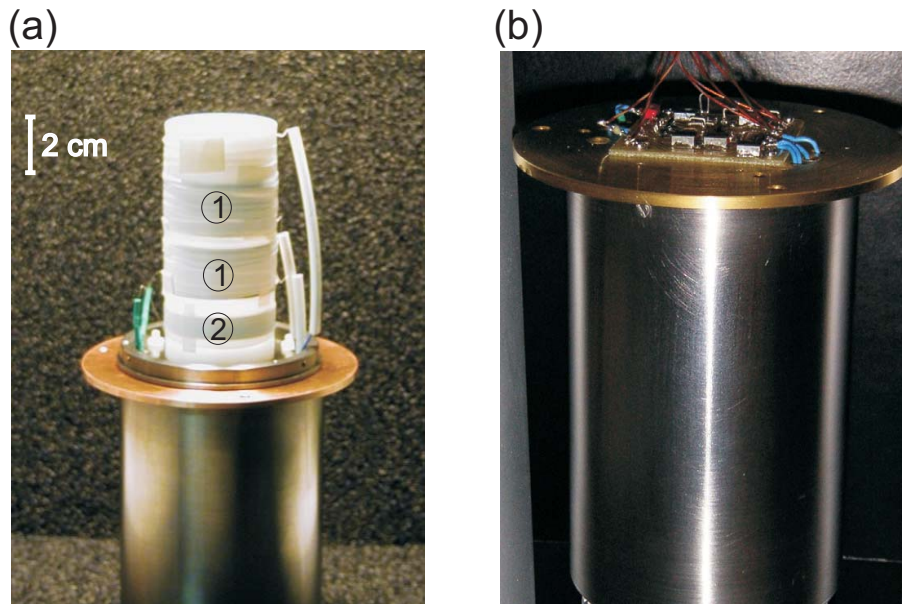
Figure 7.16: (a) Photo of the superconducting coil showing the primary (1) and secondary (2) windings. In (b) the mounted helical resonator (coil plus coaxial shield) is shown. The 4-K amplifier, shown on the top plate, is directly connected to the secondary winding of the coil.

amplified and properly prepared prior Fourier transformation into the mass domain (see Fig. 7.17). It is estimated to be in the order of 0.1 to 1 μV, which is well below the noise level of the further room temperature electronics. In order to improve the signal-to-noise ratio a first amplification stage at around 4 K is used. This is done by means of the KSC1 GaAs-MESFET amplifier from *Stahl Electronics* [118] with a measured amplification factor of 3. The next amplification stage is the so-called
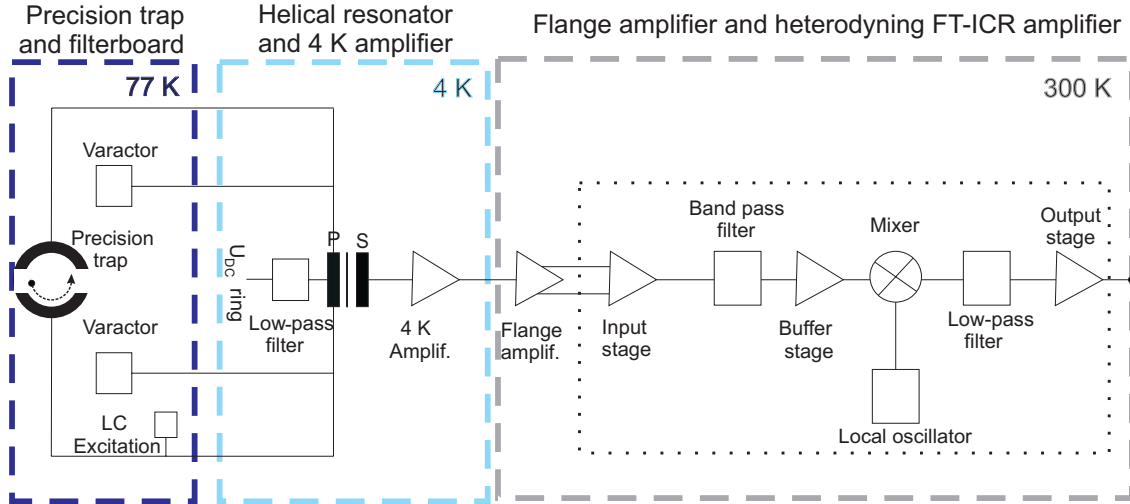
Figure 7.17: Sketch of the FT-ICR detection electronics. The signal induced in two opposite segments of the ring electrode is connected to the primary winding which has a center tap for the application of the DC trapping potential. The use of varactor diodes in the filter board allow to tune the capacity in a small range and to increase the detection sensitivity band-width. The signal is inductively coupled and primarily amplified by the 4-K amplifier. Further amplification and processing is performed in the so-called flange and the heterodyning amplifiers (see text).

flange amplifier H-LNA1. This amplifier is located at room temperature outside the vacuum chamber and electrically shielded by a stainless-steal cage. The output of this flange amplifier transforms the signals from balanced to unbalanced to reduce distortions from outside the electric shielding[7]. A typical amplification factor of 50 is measured for this stage. The last part in the analogue signal processing is the heterodyning FT-ICR amplifier which consists of a switchable band pass filter, with two available frequency ranges in order to be adjusted to the cyclotron frequencies of the reference ion and of the ion of interest. A mixer with an additional low pass filter shifts the frequency down by the local oscillator frequency (heterodyning). The total amplification of the heterodyning amplifier is measured to be 800 [79]. With this, the signal is prepared for the digital processing. Here, a Network Signal Analyzer SR780 from Stanford Research Systems [119] is used for digitization and the digital signal analysis.

Within this work a set of measurements were performed in order to check the performance of the helical resonator as well as of the other components of the FT-ICR electronics, which are partialy reported in the diploma thesis of J. Ketelaer [79]. There, a detailed description of the complete signal amplification and processing can be found. From this measurements the main characteristics of the detection circuit can be extracted and a conclusion on the final output signal's amplitude can be drawn. This information will reveal whether single ion sensitivity is feasible with such a detection scheme or not.

---

[7]In order to reduce the effect of external influences the signal is fed through two lines, each other 180° phase shifted. Since distortions are expected to act equally on both parts, the difference signal of the two lines delivers the original signal free of perturbations.
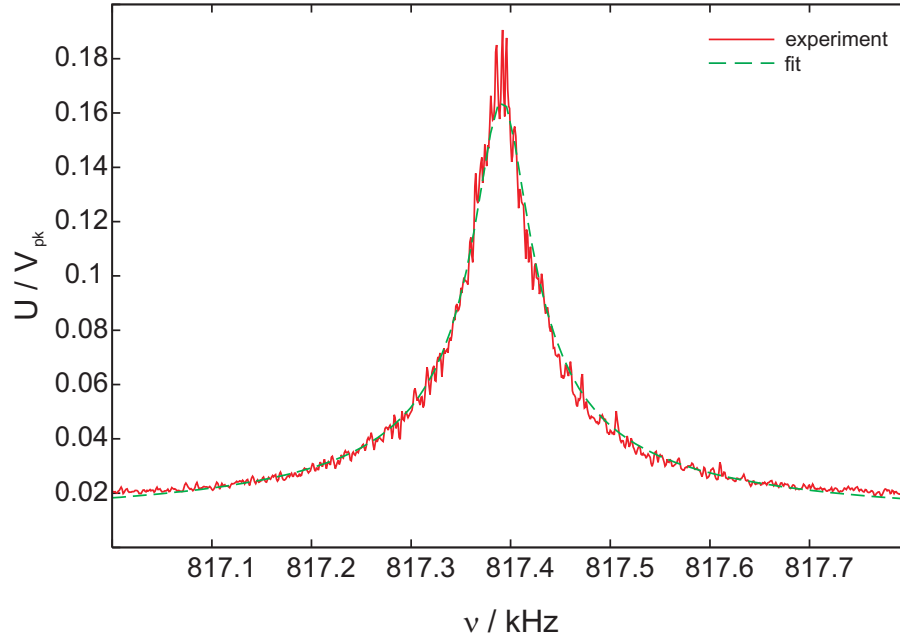
Figure 7.18: Resonance spectrum of the unloaded superconducting helical resonator with a parallel capacitance $C_{\mathrm{par}} = 106$ pF. The fit (dashed line) of the theoretical line shape yields a quality factor $Q = 15372 \pm 153$ and a resonance frequency $\nu_{\mathrm{LC}} = (817.39 \pm 0.06)$ kHz.

7.5.1 Performance of the detection inductivity

In a first measurement, the Q-value of the helical resonator was investigated without being connected to the trap electrodes (referred to as unloaded Q-value). With this measurement an upper limit of the reachable Q-value could be determined, since later the additional ohmic resistance of the wires connecting the resonator with the trap electrodes and capacitive losses will always deteriorate its performance. An important information obtained from this measurement is the intrinsic capacity of the helical resonator and the cryogenic amplifier board. In this measurement the capacity C is formed by a trim capacitor C_{par} in parallel to the helical resonator with a value of $C_{\mathrm{par}} = (106 \pm 1)$ pF, and the intrinsic capacity C_{int}, which accounts for the contribution of the resonator and the amplifier board. Such a system was excited by white noise with an amplitude of $5\,\mathrm{mV_{rms}}$. The result is shown in Fig. 7.18. A fitting of the theoretical line-shape, given in [79], to the experimental points results in a Q-value of $Q = 15372 \pm 153$ and a resonance frequency $\nu_{\mathrm{LC}} = 817.39 \pm 0.06$ kHz. One more measurement was performed with a different value of C_{par} in order to calculate the value of C_{int} and the inductance L of the helical resonator by means of Eq. (4.21). From the system of two equations with the two unknown parameters the inductance $L = (337 \pm 6)\,\mu\mathrm{H}$ and the capacitance $C_{\mathrm{int}} = 6.3 \pm 1.8$ pF were deduced.

7.5.2 Performance of the complete FT-ICR detection system

For this test the helical resonator was connected to the trap electrodes and thus the performance of the full FT-ICR detection system was investigated. Here, a decrease
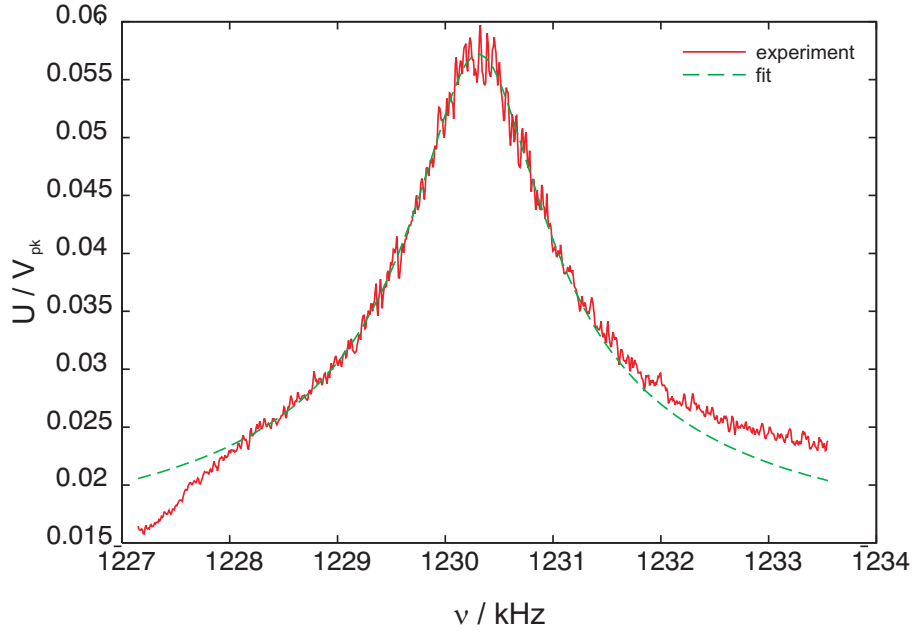
Figure 7.19: Resonance spectrum of the complete FT-ICR detection system including trap and filterboard. The dashed curve represents a fit of the theoretical lineshape which yields a resonance frequency $\nu_{LC} = (1230.31 \pm 0.01)$ kHz and a quality factor $Q = 1064 \pm 14$. The deviation of the experimental curve from the theoretical shape at the resonance's base is due to the noise level, which is not constant in the displayed frequency range.

of the Q-value with respect to the unloaded configuration is expected. An additional information that can be extracted from these measurements via Eq. (4.21) is the parasitic capacitance of the complete setup provided the known inductance L of the resonator and the determined resonance frequency ν_{LC}. The connection of the trap electrodes to the resonator are done via the filterboard located at the CF60 flange of the cube in contact with the 77-K region. In this board two identical circuits including a varactor (variable capacitor) diode are connected to the end taps of the coil and allow to tune the parallel capacitance within a certain limit to cover a wider band with increased detection sensitivity as well as to correct asymmetric capacitances due to the wires. With this configuration, several spectra were recorded in order to determine the Q-value and the resonance frequency. An example of such a measurement is illustrated in Fig. 7.19. The new resonance frequency $\nu_{LC} = 1230.31 \pm 0.01$ kHz is different to the one for the unloaded case since the total capacity of the system is smaller than the capacity used there ($C_{par} = 106 \pm 1$ pF) in order to calculate the L and C of the resonator and amplifier board. In all measurements a Q-value around $Q = 1000$ was obtained. This dramatic decrease of the Q-value as compared to the unloaded system points to some limiting components in the detection electronics. In fact a factor of 2 is missing taking into account the predictions of $Q = 2171 \pm 185$ for such a system given by the quality factor of the inductance. Several tests were performed with the different components (varactors, feedthroughs, heat contact of the filterboard, etc.) in oder to find the missing factor without any indication. The reason for such deviation is still not well understood

but further tests are foreseen in order to clarify the situation. However, the obtained Q-value is still good enough for single ion detection, as will be discussed below.

Given the value of the resonator's inductance L found in Sec. 7.5.1, the value of the capacitance due to the trap electrodes C_{trap} can easily be calculated using Eq. (4.21). All results corresponding to the test of the FT-ICR detection system are summarized in Tab. 7.3. Due to a fine tuning -in a small interval- of the total capacitance by means of the varactors, the high-sensitivity detection can be tuned to be in resonance with ions of mass number $A = 87$ and 88. A replacement of the Cs-zeolite in the present surface ionization source by Rb-zeolite enriched with the stable isotope ^{87}Rb is foreseen. This will enable a frequency measurement with ions of a well-known mass ($\delta m/m \approx 10^{-10}$ [120]). Considering the induced image current of a single singly-charged ion, which was estimated to be 0.12 pA (see Sec. 4.9) and a resistance in resonance of the detection circuit $R = (2.72 \pm 0.07)$ MΩ, given by Eq. (4.24), the voltage drop across the LC circuit is found to be $U = (0.33 \pm 0.01)$ μV. After the analogue signal processing (see Fig. 7.17) an amplification factor of $A = (1.24 \pm 0.15) \cdot 10^5$ has been measured, which will lead to a final signal amplitude of $U = (41 \pm 5)$ mV . This amplitude is perfectly suited for a digital FFT analysis that will provide the frequency domain information, and finally the mass value of a single trapped ion.

Table 7.3: Parameters involved in the FT-ICR detection system determined by two different tests. C_{filter} indicates the capacitance of the filterboard, including the connections to the resonator and the feedthroughs to the trap vacuum chamber, depending on the varactor's biasing. Given are the resulting lower and upper limits. The same is valid for the resonance frequency ν_{LC}, which is given for the complete detection system. In some cases the tabulated quantities correspond to the average value of the various measurements performed.

test Q-unloaded	test Q-loaded
$Q = 14700 \pm 300$	$Q = 1050 \pm 20$
$\nu_{\text{LC}} = (817.39 \pm 0.06)$ kHz	$\nu_{\text{LC}} = ([1214.89 - 1233.85] \pm 0.02)$ kHz
$L = (337 \pm 6)$ μH	$C_{\text{filter}} = ([26.6 - 28.0] \pm 1.9)$ pF
$C_{\text{coil}} = (6 \pm 2)$ pF	$C_{\text{trap}} = (16.52 \pm 0.01)$ pF

7.6   Experimental mass measurement procedure using FT-ICR

The mass measurement procedure using the FT-ICR detection will be performed after isobaric selection of the species of interest via buffer-gas cooling in the purification trap [47]. The cooling and selection of the isobars are done in two steps: First, the ions are excited by a radiofrequency field at the magnetron frequency, which increases the magnetron orbit of all ions to a radius larger than that of the channel of the pumping barrier connecting both traps. The second step is the application of a quadrupolar excitation at the cyclotron frequency of the ion specie of interest. As discussed in Sec. 2.5, this excitation in combination with a buffer gas at a pressure

around 10^{-5} mbar cools and centers only those ions whose charge-to-mass ratio corresponds to the applied cyclotron frequency. Consequently, only centered ions can pass the channel towards the measurement trap. Once the ions have been selected, they are transfered to the hyperbolical measurement trap. Here, first a resonant azimuthal dipolar excitation at the cyclotron frequency ω_+ is performed in order to enhance the motional amplitude of the ions and thus to improve the induced image current[8]. Even when the detection sensitivity allows for the detection of a single ion, phase-coherence must be established between the small number of ions present in the trap. If not, two ions with the same cyclotron radius but $180°$ phase-shifted would generate a net zero induced image current.

Since the exact cyclotron frequency is not known beforehand, the excitation bandwidth must be increased using a shorter excitation time T_{exc}[9]. The excitation has to be followed by a short waiting period in order to avoid the influence of the excitation signal on the detection electronics. Subsequently, a transient is recorded for a time T_{s} in order to perform a Fourier transformation of the ion signal to the frequency domain. In case a signal amplitude well above the background noise level is detected or not, the transient recording will be continued or the trap will be emptied and reloaded in order to search for a detectable ion signal.

In case the transient recording reveals a clear signal of induced image current, the corresponding excitation bandwidth is made narrower and thus more selective by increasing the excitation time. In fact, a single-frequency excitation of duration T_{exc} broadens the spectral range of the excitation to a bandwidth of $\sim 1/T_{\mathrm{exc}}$ around the selected frequency. This Fourier-limited excitation defines the ultimately precision with which ions can be mass selective. For instance, an excitation time longer than 10 ms would be required to separate the isobars ^{92}Tc and ^{92}Ru, considering singly charged ions in a magnetic field of 7 T. Alternatively, in case the contaminants are known or identified, a dipolar excitation at their cyclotron frequency ν_+ can be applied to remove them from the trap and to leave only the ions of interest.

The length of the transient recording, which will fix the mass resolution, is limited by the half-life and the ion mean-free-path or equivalently, the ion-neutral collisions responsible of the signal damping. The first cannot be changed, however, the signal coherence in the measurement can be done longer than the half-lives of the investigated ions by keeping ultra-high vacuum conditions in the measurement trap, so there are essentially no ion-atom collisions while data recording.

In case of investigation of long-lived species, which might exceed the coherence time, the sampling time T_s has to be selected according to the number of ion-atom collision per second ν_{col} and thus, perform the data acquisition in the low pressure regime, *i.e.* free of ion-atom collisions. Prior the calculation of ν_{col} one must first

---

[8]It is worth to note that different detection schemes for FT-ICR can be applied [121], as *e.g.* the azimuthal quadrupolar detection proposed for broad-band detection by L. Schweikhard *et al.* [122]. In this scheme, instead of taking the difference of the transient signals from two opposite electrodes, as used in this work to obtain a signal at the cyclotron frequency ν_+, the difference of the sum of these signals and the sum of a similar set of electrodes perpendicular to the first is taken. In this way resonances are observed at the free cyclotron frequency $\nu_c = \nu_+ + \nu_-$, which does not depend on the trapping potential.

[9]The excitation of the ions with white noise is not considered due to the possible presence of isobars in the measurement trap that might be excited as well, distorting the ion signal of interest.

determine the *ion-atom collision rate constant k* that is given by [76]

$$k = \sqrt{\frac{\pi\alpha' q^2}{\epsilon_0 \mu}} \,, \tag{7.16}$$

where α' is the neutral polarizability, q is the elementary charge, ϵ_0 the vacuum permittivity, and μ is the reduced mass of the ion and atom.

Here, an ion of mass $A = 250$ u is considered to collide with helium atoms. In order to obtain the collision frequency for a single ion, the pressure must be given as the number of atoms per volume unit. Assuming a pressure of 10^{-8} mbar in the measurement trap and considering ideal gas conditions, it corresponds to an atom concentration of $9.4 \cdot 10^8$ atoms per cm^3 at 77 K (temperature of the trap environment). For an ion of 250 u colliding with He atoms, the neutral polarizability is found to be $\alpha' = 0.2 \cdot 10^{-24}$ cm^3 [123]. From these values, Eq. (7.16) yields an ion-atom collision rate constant $k = 5.3 \cdot 10^{-10}$ cm^3 s^{-1} . If we now multiply this number by the atom concentration we obtain $\nu_{\text{col}} \approx 0.5$ collisions per second per ion. Since the damping constant α_+ (see Sec. 2.5.1) can be written as a function of the collision frequency [76]:

$$\alpha_+ = \frac{m_{\text{atom}}}{m_{\text{ion}} + m_{\text{atom}}} \cdot \nu_{\text{col}} \,, \tag{7.17}$$

we can conclude that the the amplitude of the cyclotron motions is damped with a time constant $\tau_+ = 1/\alpha_+ = 128$ s.

However, with a single measurement of ν_+ we are not able to get the mass value of the atom of interest since the magnetic field and trapping voltage are not known. In order to get the required information about the magnetic field and trapping voltage we will use a mass calibration formula from which the measurement of the frequency of two ions of known mass will serve to derive the magnetic field strength and to calibrate the trapping voltage. This calibration formula is derived in [124] and for the case of zero pressure (free ion-atom collision while transient recording) can be easily derived from Eq. (2.10) to yield

$$\frac{m}{q} = \frac{a}{\nu_+} - \frac{b}{\nu_+^2} \,, \tag{7.18}$$

where $a = B/2\pi$ and $b = U/8\pi^2 d^2$. These two constants can be determined experimentally by measuring the frequencies of two reference ions with well-known mass. In order to account for the intrinsic magnetic field drift (see Sec.2.3), a and b will be determined before and after the measurement of the ion of interest. In such a way a linear interpolation will be employed to calculate the magnetic field strength B and the trapping voltage U at the moment of the mass measurement of the ion under investigation.

Chapter 8

Summary and Outlook

The work carried out in the scope of this thesis has dealt, in the first part, with the mass measurement and the analysis of ten neutron-deficient radionuclides (^{89}Tc, ^{90m}Tc, ^{91}Tc, ^{92}Tc, ^{90}Ru, ^{91}Ru, ^{92}Ru, ^{94}Ru, ^{92}Rh, ^{93}Rh) interspersed in the rp-process path, important to clarify the mechanisms of stellar nucleosynthesis. The SHIP-TRAP mass spectrometer in combination with the destructive time-of-flight detection technique was used to obtain experimental mass values with a relative mass uncertainty of $\delta m/m \geq 6 \cdot 10^{-8}$ for the evaporation residues delivered by SHIP. Six of the reported masses have been measured for the first time and have served to check the predictive power of systematical trends based on the knowledge of the mass surface in this region. The remaining four mass values are found to be in very good agreement with the already experimentally known values. With the exception of ^{94}Ru, all experimental mass uncertainties have been improved, many of them by more than an other of magnitude. An important consequence of the results presented, is that the mass surface must be lifted by a few hundred keV as compared to the predictions done in the AME 2003, based on systematical trends. As a conclusion of the atomic-mass evaluation of the SHIPTRAP data, a reshaping of the mass surface for neutron-deficient nuclides in the region between $Z = 40$ and $Z = 50$ is suggested, which can be applied as a general trend in order to make better predictions of the unknown species in the region investigated.

In the second part of the thesis, the commissioning and set-up of a new cryogenic double Penning trap mass spectrometer for SHIPTRAP is reported. It combines the former destructive detection technique with a non-destructive detection based on the Fourier transformation of the ion-induced image currents. In addition, a detailed description of the work carried out in order to characterize the performance of the individual parts of the newly developed experimental setup is reported. These first off-line tests include:

- A theoretical and experimental characterization of the gas flow through a differential pumping barrier, which is required for the effective suppression of the diffused gas originated from the presence of a buffer-gas in the purification trap. The experimental requirements of pressure conditions better than $p = 10^{-8}$ mbar in the measurement trap are matched by the use of a pumping barrier with a 2 mm diameter and ~ 50 mm long channel together with a customized sealing from Turcon™ Variseal. With this configuration a suppression factor of 10^3 between both trap volumes is obtained, which enables a coherent ion motion during the measurement process. This new approach improves the

performance of the pumping barrier in the present room-temperature setup by at least a factor of 20. A further increase in the differential pumping by a factor of 2 can be achieved by using a 1.5 mm diameter channel, however with the drawback of a reduction in transport efficiency.

- A direct comparison of the relative detection efficiencies of a channeltron and a MCP detector revealing a factor of 3.5 higher efficiency for the former. The suspected misalignment between the MCPs' bias angle in the Chevron configuration might have slightly decreased its detection efficiency. In any case, the replacement of the present MCP detector by a channeltron with a conversion dynode is clearly justified. This combination might well reach close to 100% detection effciency, independently of the energy of the ion beam, allowing for higher statistics and a significant reduction in the final mass uncertainty. Thus, the investigation of radionuclides with the TOF-ICR detection technique can exploit this higher efficiency in order to address regions of more exotic species. A similar system is meanwhile also in use at ISOLTRAP (CERN).

- The characterization of the complete system for the FT-ICR detection technique. The determination of an unloaded Q-value, *i.e.* quality factor, of the helical resonator of $Q = 14700 \pm 300$ is reported together with the main features of the different components of the detection system. A severe decrease of the Q-value is observed when connecting the trap segments to the tank circuit limiting its value to $Q = 1050 \pm 20$. Estimations of the total resistance due to the cables and electrodes connected result in $Q \approx 2000$. The factor of two missing in the experimental Q-value is to date still not well understood. Without consideration of the last, the present Q-value still meets the S/N-ratio requirements and allows us to perform first off-line measurements in order to demonstrate the single singly-charged ion detection sensitivity. A resistance of the tank circuit in resonance of $R = (2.72 \pm 0.07)\,\mathrm{M\Omega}$ with the estimated induced current by a single singly-charged ion of about 100 fA, will produce a voltage drop across the detection circuit of $U = (0.33 \pm 0.01)\,\mu\mathrm{V}$. After the signal processing a total amplification factor of $A = (1.24 \pm 0.15) \cdot 10^5$ has been measured, which will provide a voltage signal well suited for the FFT analysis into the frequency domain.

After the complete installation of the apparatus a series of beam transfer tests were performed prior to the capture and the demonstration of the mass measurement with the FT-ICR technique. The aim of these tests was to optimize the transfer of ions from the surface ionization source through more than 50 electrodes up to the detector at the end of the setup. Simulations of the whole setup were performed with SIMION 7.0 and were found to be decisive to succeed in this task. A count rate of 30 kHz was measured at the MCP detector for a high current in the ion source after setting the voltages obtained by the simulations. Due to the unshielded magnetic field of the superconducting magnet used for the off-line tests, which causes an extended stray field, and the lack of proper ion optics in the beam line to overcome it, the transfer efficiency was found to be insufficient to pulse the beam and to initiate the capturing process. A new set of three Einzel lenses and four quadrupolar deflectors have been recently installed along the beam line, which will allow an

efficient injection into the magnetic field and therefore will enable higher transfer efficiencies.

A new MCP delay-line detector is presently being tested and will be included in the setup for the realization of the TOF-ICR technique. It combines the time resolution of a MCP in Chevron configuration with the spatial resolution of a delay-line anode. The use of such a detector will offer the time information required for the time-of-flight detection and also the spatial position of the ions inside the trap prior to their extraction. From the spatial information we will for example be able to select only the ions properly centered and hence, unaffected by the higher-order contributions to the trapping field. Furthermore, a clear separation between resonantly and non-resonantly excited ions will enable to select the best contrast conditions to perform a high-precision time-of-flight detection with a minimum number of ions.

After the demonstration of the trapping and detection capabilities in our laboratory, the setup will move to the Mainz TRIGA reactor at the end of the summer 2007. A new superconducting magnet identical to the SHIPTRAP magnet was set up in the reactor hall in July 2007, where a first period of operation in the mass spectrometry of heavy ions via the FT-ICR technique will be carried out. In the first attempts, samples of transuranium elements ranging from $Z = 92$ to $Z = 98$ will be prepared and transferred to the ion source in the apparatus for off-line ionization. Later, a target of californium will be bombarded with neutrons from the reactor and the products of the spallation reactions (Cd, In, Sn, etc..) will be directly transported from the reactor to the Penning trap system.

Once the setup has been completely characterized and has demonstrated perfect capability to perform mass measurements on single singly-charged heavy ions, the setup will be installed at SHIPTRAP for the investigation of transfermium elements. At SHIPTRAP, a beam time is scheduled for August 2007 for the investigation of the rarely-produced ^{254}No nuclide with the present TOF-ICR detection technique [37]. ^{254}No has a relatively high cross section of $\sigma = 2.2 \, \mu b$, as compared to other transfermium elements. This is due to the production via a double-magic projectile and target reaction and due to the vicinity of nobelium to the neutron subshell closure at $N = 152$. With a primary beam intensity of 1.5 particle μA and a target thickness of 0.5 mg/cm^2 this cross section corresponds to a rate of 5 ions per second entering the gas cell. For this rate, a measurement time of at least four hours is required for a single cyclotron resonance with about 300 ions, assuming an overall efficiency of 0.5%. In order to improve the present mass uncertainty of ^{254}No of $\delta m = 18$ keV, obtained from nuclear spectroscopy experiments, a minimum of 1500 ions (one day of data acquisition) are needed to reach a mass uncertainty of $\delta m = 10$ keV with a resolving power of $R = 500000$, very close to the limit of the present experimental performance of the setup.

With the use of the FT-ICR cryogenic setup presented in this work, the transient recording of a single ion of 10 s duration will yield a resolving power of about $R = 5 \cdot 10^6$ and a mass uncertainty of $\delta m = 55$ keV from a single measurement. This transient recording duration might be even increased due to the ultra-high vacuum conditions in the measurement trap by the use of the cryogenic pumping barrier, which ensures coherence times of up to $\tau = 128$ s. According to the half-life of $T_{1/2} = 51$ s for ^{254}No, a minimum of about six ions, *i.e.* 25 transients of $T_s = 10$ s, would be required in this conditions to reach a mass uncertainty of $\delta m = 10$ keV. Considering the overall efficiency mentioned above and assuming a similar empirical

relation for the calculation of the mass uncertainty as for the TOF-ICR case, a mass measurement of ^{254}No with a mass uncertainty of 10 keV will be performed in less than 10 minutes. A tremendous reduction in measurement time.

Appendix A

Simulations as a first approach

Calculation of errors for the pressure ratio

In the following, the error bars for the theoretical and experimental data presented in Fig. 7.15 and Fig. 7.11 is derived employing the propagation of errors of the individual parameters involved in the value of the pressure ratio.

$$
\begin{aligned}
\delta\left(\frac{p_1}{p_2}\right)_{\text{theo}} &= \left[\left(-k_1\frac{S_2}{L^2} - \frac{k_1}{1+\frac{7.1}{2.44}\left(\frac{p_2}{p_2^0}-1\right)}\frac{S_2}{L^2}\right)^2 \cdot (\delta L)^2 \right. \\
&\quad + \left(-\frac{7.1\cdot 2.44\cdot p_2^0}{[7.1(p_2-p_2^0)+2.44\cdot p_2^0]^2}\left(k_1\frac{S_2}{L}+\frac{p_1^0}{p_2^0}-1\right)\right)^2 (\delta p_2)^2 \\
&\quad + \left(\frac{1}{1+\frac{7.1}{2.44}\left(\frac{p_2}{p_2^0}-1\right)}\frac{1}{p_2^0}\right)^2 \cdot (\delta p_1^0)^2 \\
&\quad + \left(\frac{7.1\cdot 2.44\cdot p_2}{[7.1\left(p_2-p_2^0\right)+2.44\cdot p_2^0]^2}\left(k_1\frac{S_2}{L}+\frac{p_1^0}{p_2^0}-1\right) - \frac{1}{1+\frac{7.1}{2.44}\left(\frac{p_2}{p_2^0}-1\right)}\frac{p_1^0}{(p_2^0)^2}\right)^2 \\
&\quad \left. \cdot \left(\delta p_2^0\right)^2\right]^{1/2} \tag{A.1}
\end{aligned}
$$

$$
\begin{aligned}
\delta\left(\frac{p_1}{p_2}\right)_{\text{exp}} &= \sqrt{\left(\frac{\delta p_1}{\delta p_2}\right)^2 + \left(-\frac{p_1\cdot\delta p_2}{p_2^2}\right)^2} \\
&= 0.1\cdot\sqrt{2}\frac{p_1}{p_2} \tag{A.2}
\end{aligned}
$$

Simulation Studies

Electron Impact Ion Source

The axial ionizer manufactured by ABB Extrel is designed specifically for a high-efficient electron impact ionization of atomic and molecular beams. It can be used for the ionization of residual gas, which can be varied by a regulated inlet valve at the vacuum chamber.

The main parts of this ionizer are an ion creation region, where the ions are created by electron bombardement from a hot tungsten wire, an extraction disk, and an electrostatic lens for focussing the ion beam. The geometry file for the SIMION program as well as its graphical representation in the program is shown below.

Ion Source Geometry file with a cross-sectional (top) and an isometric view (botton)

```
pa_define(210,190,1,Cyl,y,e)
;
Locate(5,0,0,1)
{Elect(1)
;                               Lens 1 (A) + lens 3 (C)
  { Fill   { within { Box(10.2,25,35.2,26) }
      within  { Box(35.2,25,41.4,73.5) }
      within { Box(78.9,9.35,85.1,73.5) }
    }
   }
}
Locate(5,0,0,1)
{Elect(2)
;                               lens 2 (B)
  { Fill
    { within { Box(44.6,25,50.8,73.5) }
      within  { Box(50.8,25,75.8,26) }
    }
   }
}

Locate(5,0,0,1)
{Elect(3)
;                        Extractor (D)
 { Fill
    { within { Box(88.3,6.25,94.5,73.5) }

    }
  }
}
Locate(5,0,0,1)
{Elect(4)
;                          Ion region (E)
  { Fill
    { within { Box(97.7,17.5,103.9,73.5) }
      within  { Box(97.7,17,150.5,17.5) } ;
      within  { Box (150.5,9.25,151.5,17.5)} ; small ring in the ion region
    }
   }
}
Locate(5,0,0,1)
{Elect(5)
;                     Ion region shield (grounded) (F)
 { Fill
    { within { Box(107.1,25,113.3,73.5) }

    }
   }
}

Locate(5,0,0,1)
{Elect(6)
```
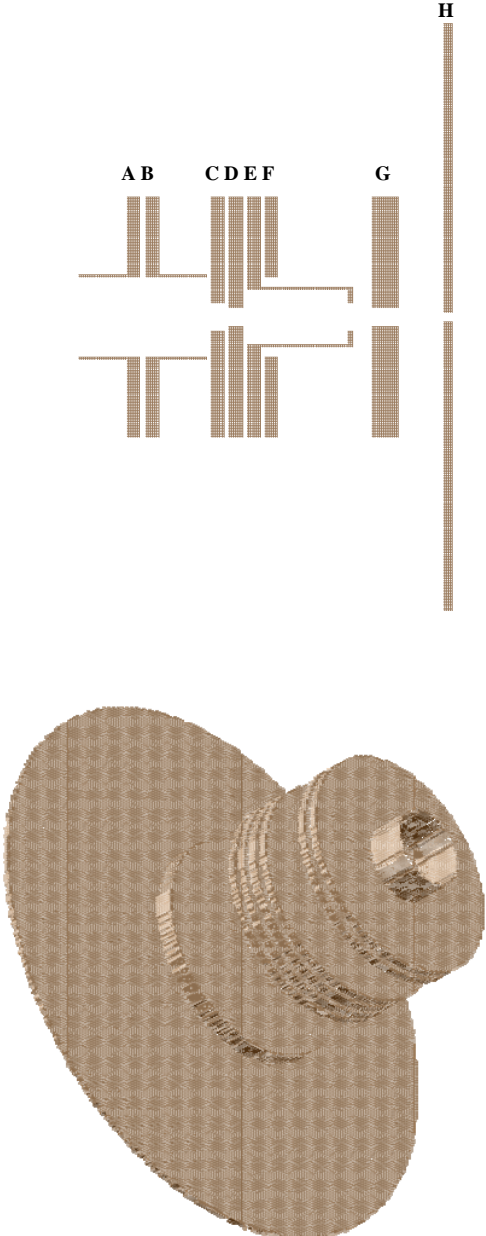
```
;                            entrance plate (grounded) (G)
```

```
{ Fill    { within { Box(163.3,6.25,175.8,73.5) }
    }
  }
}
```

```
Locate(5,0,0,1)             ; extraction disk (H)
{ Elect(7)
  { Fill
      { within { Box(200,3,204,181) }}}}
```

Quadrupolar Deflector Energy Filter

The quadrupolar deflector allows to separate ion species according to their different energies. It consists of four hyperbolically shaped electrodes placed in the parallel vertex of a cube, which produce the electrostatic quadrupole field used to deflect the ions. A cutview is illustarted below to show its inner structure. Changing the polarity of the potential applied to these electrodes, it is possible to deflect the ion beam by 90º in both directions. A circular lens at each entrance and exit side of the deflector allows for optimized focussing conditions of the ion beam. The geometry file for its implementation in SIMION is given below.

Quadrupolar Deflector Geometry file with isometric views


```
pa_define(311,200,311,p,y)

;----------------------------hyperbolic poles--------------------------------------------------------------------

locate(80,0,80,26.8,-90,,-90)    ;scaling (26.83) factor taken according to the real size of our deflector
     {
electrode(1)              ; 2 opposite hyperbolic poles  upper left,lower right
         {
         fill
             {
             within{
                 locate(0,0,0,1,,-45)
                      {hyperbola(0,0,0.723,0.789)}
                 centered_box3D(0,0,0,2.4,2.4,2.4)
                   }
              }
          }
electrode(2)          ; 2 remaining opposite hyperbolic poles
         {
         fill
             {
             within{
                 locate(0,0,0,1,,45)
                      {hyperbola(0,0,0.723,0.789)}
                 centered_box3d(0,0,0,2.4,2.4,2.4)
                    }
              }
           }
}

;---------------------------------------- 4 'side' plates housing the focusing lenses of the bender----------------------------

locate(80,0,80,26.8)
{
      electrode(3)    ;
            {
            fill
              {
              within{centered_box3d(1.375,0,0,0.25,2.4,2.4)}         ;right(on the zx view) grounded plate
              locate(0,0,0,1,-90)
                    {
                    notin{cylinder(0,0.625,-1.25,0.048,,0.25)}     ;holes
                    notin{cylinder(0,0.625,-1.25,0.13,,0.125)}
                    notin{cylinder(0.625,0,-1.25,0.048,,0.25)}
                    notin{cylinder(0.625,0,-1.25,0.13,,0.125)}

                    notin{cylinder(-0.625,0,-1.25,0.048,,0.25)}
                    notin{cylinder(-0.625,0,-1.25,0.13,,0.125)}

                    notin{cylinder(0,0.8,-1.25,0.0565,,0.25)}
                    notin{cylinder(0.8,0,-1.25,0.0565,,0.25)}
                    notin{cylinder(-0.8,0,-1.25,0.0565,,0.25)}
```
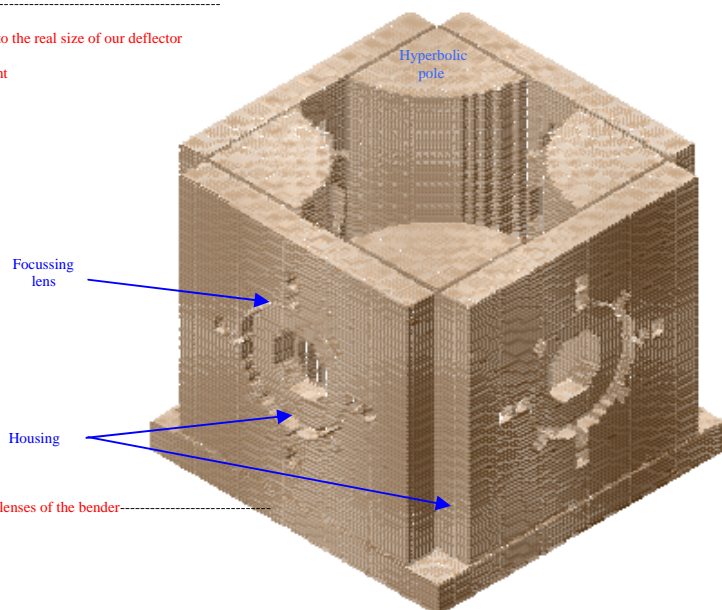
```
                                notin{cylinder(0.442,0.442,-1.25,0.032,,0.25)}
                                notin{cylinder(0.442,0.442,-1.25,0.13,,0.125)}

                                notin{cylinder(-0.442,0.442,-1.25,0.032,,0.25)}
                                notin{cylinder(-0.442,0.442,-1.25,0.13,,0.125)}

                                notin{cylinder(0,0,-1.25,0.53,,0.25)}
                                }
                                }
            fill
                {
                within{centered_box3d(-1.375,0,0,0.25,2.4,2.4)}        ; left (on the zx view) grounded plate
                locate(0,0,0,1,90)
                        {
                        notin{cylinder(0,0.625,-1.25,0.048,,0.25)}        ; holes
                        notin{cylinder(0,0.625,-1.25,0.13,,0.125)}
                        notin{cylinder(-0.625,0,-1.25,0.048,,0.25)}
                        notin{cylinder(-0.625,0,-1.25,0.13,,0.125)}

                        notin{cylinder(0.625,0,-1.25,0.048,,0.25)}
                        notin{cylinder(0.625,0,-1.25,0.13,,0.125)}

                    notin{cylinder(0,0.8,-1.25,0.0565,,0.25)}
                    notin{cylinder(-0.8,0,-1.25,0.0565,,0.25)}
                    notin{cylinder(0.8,0,-1.25,0.0565,,0.25)}

                    notin{cylinder(-0.442,0.442,-1.25,0.032,,0.25)}
                    notin{cylinder(-0.442,0.442,-1.25,0.13,,0.125)}

                    notin{cylinder(0.442,0.442,-1.25,0.032,,0.25)}
                    notin{cylinder(0.442,0.442,-1.25,0.13,,0.125)}

                    notin{cylinder(0,0,-1.25,0.53,,0.25)}
                    }
                    }
            fill
                {
                within{centered_box3d(0,0,-1.375,2.4,2.4,0.25)}        ; back (on the zx view) grounded plate
                notin{cylinder(0,0,-1.25,0.53,,0.25)}

                notin{cylinder(0,0.625,-1.25,0.048,,0.25)}        ; holes
                notin{cylinder(0,0.625,-1.25,0.13,,0.125)}
                notin{cylinder(-0.625,0,-1.25,0.048,,0.25)}
                notin{cylinder(-0.625,0,-1.25,0.13,,0.125)}
                notin{cylinder(0.625,0,-1.25,0.048,,0.25)}
                notin{cylinder(0.625,0,-1.25,0.13,,0.125)}

                notin{cylinder(0,0.8,-1.25,0.0565,,0.25)}
                notin{cylinder(0.8,0,-1.25,0.0565,,0.25)}
                notin{cylinder(-0.8,0,-1.25,0.0565,,0.25)}

                notin{cylinder(0.442,0.442,-1.25,0.032,,0.25)}
                notin{cylinder(0.442,0.442,-1.25,0.13,,0.125)}
                notin{cylinder(-0.442,0.442,-1.25,0.032,,0.25)}
                notin{cylinder(-0.442,0.442,-1.25,0.13,,0.125)}
                }

            fill
                {
                locate(0,0,0,1,180)                        ; front(xz view) grounded electrode
                        {
                        within{centered_box3d(0,0,-1.375,2.4,2.4,0.25)}
                        notin{cylinder(0,0,-1.25,0.53,,0.25)}

                        notin{cylinder(0,0.625,-1.25,0.048,,0.25)}        ;holes
                        notin{cylinder(0,0.625,-1.25,0.13,,0.125)}
                        notin{cylinder(-0.625,0,-1.25,0.048,,0.25)}
                        notin{cylinder(-0.625,0,-1.25,0.13,,0.125)}

                        notin{cylinder(0.625,0,-1.25,0.048,,0.25)}
                        notin{cylinder(0.625,0,-1.25,0.13,,0.125)}


                        notin{cylinder(0,0.8,-1.25,0.0565,,0.25)}
                        notin{cylinder(-0.8,0,-1.25,0.0565,,0.25)}

                        notin{cylinder(0.8,0,-1.25,0.0565,,0.25)}


                        notin{cylinder(-0.442,0.442,-1.25,0.032,,0.25)}
                        notin{cylinder(-0.442,0.442,-1.25,0.13,,0.125)}

                        notin{cylinder(0.442,0.442,-1.25,0.032,,0.25)}
                        notin{cylinder(0.442,0.442,-1.25,0.13,,0.125)}
                        }
                    }
                }
;--------------------------------------------'side' focusing lenses of the bender----------------------------------
        electrode(4)
                {
                fill
                    {
                    locate(0,0,0,1,-90)                        ;right(zx view) focusing lens
                            {
                            within{cylinder(0,0,-1.25,0.5,,0.2)}
                            notin{cylinder(0,0,-1.25,0.25,,0.2)}
                            }
                    }
```
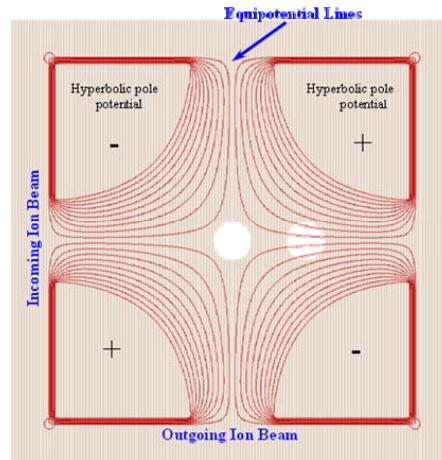
```
                   fill
                          {
                          locate(0,0,0,1,90)
                                 {
                                 within{cylinder(0,0,-1.25,0.5,,0.2)}          ;left(zx view) focusing lens
                                 notin{cylinder(0,0,-1.25,0.25,,0.2)}
                                 }
                          }
                   }


         electrode(5)
                          {                                                    ;focusing lens of the bender
                          fill
                                 {
                                 locate(0,0,0,1,180)                  ; front (zx view) focusing lens
                                        {
                                        within{cylinder(0,0,-1.25,0.5,,0.2)}
                                        notin{cylinder(0,0,-1.25,0.25,,0.2)}
                                        }
                                 }
                          fill
                                 {
                                 within{cylinder(0,0,-1.25,0.5,,0.2)}          ;back (zx) focusing lens
                                 notin{cylinder(0,0,-1.25,0.25,,0.2)}
                                 }
                          }
;----------------------------------------upper and lower housing plates of the bender--------------------------------------------------
electrode(6)
{
 fill
         {
         within{centered_box3d(0,1.31,0,3,0.22,3)}                    ;upper plate (the lower plate is deduced by symmetry)
         locate(0,1.2,0,1,,90)
                 {
                 notin{cylinder(0,0,0,0.125,,0.22)}                  ; holes
                 notin{cylinder(0,0.5,0,0.125,,0.22)}
                 }

         locate(0.8,1.2,0.8,1,,90)
                 {notin{cylinder(0,0,0,0.0945,,0.22)}}
         locate(-0.8,1.2,0.8,1,,90)
                 {notin{cylinder(0,0,0,0.0945,,0.22)}}

         locate(0.8,1.2,-0.8,1,,90)
                 {notin{cylinder(0,0,0,0.0945,,0.22)}}
         locate(-0.8,1.2,-0.8,1,,90)
                 {notin{cylinder(0,0,0,0.0945,,0.22)}}

         locate(1,1.2,0.6,1,,90)
                 {notin{cylinder(0,0,0,0.0565,,0.22)}}
         locate(-1,1.2,0.6,1,,90)
                 {notin{cylinder(0,0,0,0.0565,,0.22)}}

         locate(1,1.2,-0.6,1,,90)
                 {notin{cylinder(0,0,0,0.0565,,0.22)}}
         locate(-1,1.2,-0.6,1,,90)
                 {notin{cylinder(0,0,0,0.0565,,0.22)}}

         locate(1,1.2,1,1,,90)
                 {notin{cylinder(0,0,0,0.0565,,0.22)}}
         locate(-1,1.2,1,1,,90)
                 {notin{cylinder(0,0,0,0.0565,,0.22)}}

         locate(1,1.2,-1,1,,90)
                 {notin{cylinder(0,0,0,0.0565,,0.22)}}
         locate(-1,1.2,-1,1,,90)
                 {notin{cylinder(0,0,0,0.0565,,0.22)}}

         locate(0.6,1.2,1,1,,90)
                 {notin{cylinder(0,0,0,0.0565,,0.22)}}
         locate(-0.6,1.2,1,1,,90)
                 {notin{cylinder(0,0,0,0.0565,,0.22)}}
         locate(0.6,1.2,-1,1,,90)
                 {notin{cylinder(0,0,0,0.0565,,0.22)}}
         locate(-0.6,1.2,-1,1,,90)
                 {notin{cylinder(0,0,0,0.0565,,0.22)}}


         locate(1.375,1.2,1,1,,90)
                 {notin{cylinder(0,0,0,0.058,,0.22)}}
         locate(-1.375,1.2,1,1,,90)
                 {notin{cylinder(0,0,0,0.058,,0.22)}}
         locate(1.375,1.2,-1,1,,90)
                 {notin{cylinder(0,0,0,0.058,,0.22)}}
         locate(-1.375,1.2,-1,1,,90)
                 {notin{cylinder(0,0,0,0.058,,0.22)}}

         locate(1,1.2,1.375,1,,90)
                 {notin{cylinder(0,0,0,0.058,,0.22)}}
         locate(-1,1.2,1.375,1,,90)
                 {notin{cylinder(0,0,0,0.058,,0.22)}}
         locate(1,1.2,-1.375,1,,90)
                 {notin{cylinder(0,0,0,0.058,,0.22)}}
         locate(-1,1.2,-1.375,1,,90)
                 {notin{cylinder(0,0,0,0.058,,0.22)}}}}
```
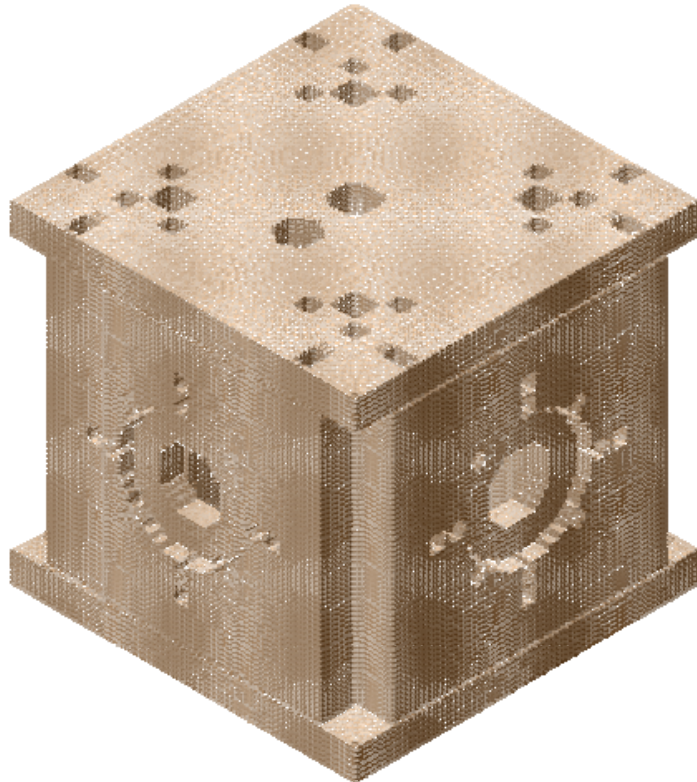
Electrostatic Lens (Einzel Lens)

The einzel lens is a three-element lens which has the freedom of having the inner electrode at either a higher or lower potential than the outer electrodes, a feature that allows the use of a simple constant geometry to achive many different focussing conditions. The einzel lens is operated at different voltages in order to obtain the focal point of the ion beam always at the position of the detector independent of the ions' energy. This imaging cannot be done just with a two element lens since a pair of voltage ratios is required to determine the focal properties. With a three-element lens, however, there are two voltage ratios, and a given focal condition may be satisfied by pairs of values of this ratios. These pairs of values form the focal point of the lens. The lens for this setup is made with two outer cylinders of 70 mm length connected electrically and a central element of 100 mm usually connected to ground.
The implementation of such an einzel lens in SIMION is done using the following geometry file:

Einzel Lens Geometry file wth isometric view

```
 pa_define(310,60,60,p,non-mirror)


locate(12,30,30,,-90)
        {
          e(1)                                              ; first element (A)
                {
                  fill{within{cylinder(0,0,0,25.5,,70)}
        notin{cylinder(0,0,0,24,,70)}}}}

locate(84,30,30,,-90)
 {
  e(2)                                                    ; second (central) element (B)
     { fill{within{cylinder(0,0,0,25.5,,100)}
      notin{cylinder(0,0,0,24,,100)}}}}

locate(186,30,30,,-90)
 {
  e(3)                                                    ; third element (C)
     { fill{within{cylinder(0,0,0,25.5,,70)}
      notin{cylinder(0,0,0,24,,70)}
             }
            }
          }
locate(258,30,30,,-90)
 {
  e(4)                                                    ; channeltron prolongation segment (D)



     { fill{within{cylinder(0, 0,0,21,,46)}

      notin{cylinder(0,0,0,19,,46)}
             }
            }
          }
locate(306,30,30,,-90)
     {
       e(5)                                               ;  detector plate (E)
         {
           fill{ within{cylinder(0,0,0,25.5,,1)}}}}
```


A

B

C

D

E
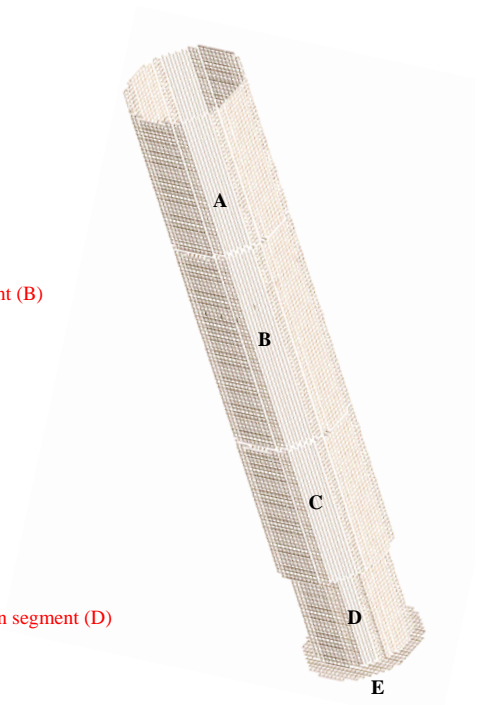
Notice the last geometry file a fourth segment is included in order to cover the empty gap during the operation of the Channeltron. In the simulation, the detector itself, is replaced by a disk of 25.5 mm diameter.

Simulation Results

After the implementation of the different electrodes in the simulation program, the behaviour of an incoming ion beam in dependence on the applied voltages was studied. The ion beam is modelled in such a way that a realistic ion distribution is represented. We have defined five different ion groups (see Tab. 1.) while one of the starting parameters is varied in each group. Figure 4 shows the definition of the coordinate system as well as the angle definition of the starting ion beam.

In the first group the elevation angle θ of the incoming ions is changed from one ion to the next one in two degree steps. The second group covers, in the same way, the azimuthal angle ϕ and the third and fourth vary the starting coordinate y and z, respectively, in 0.2 mm steps from one ion to the next one. The last group varies the energy of the ions in 2 eV steps.
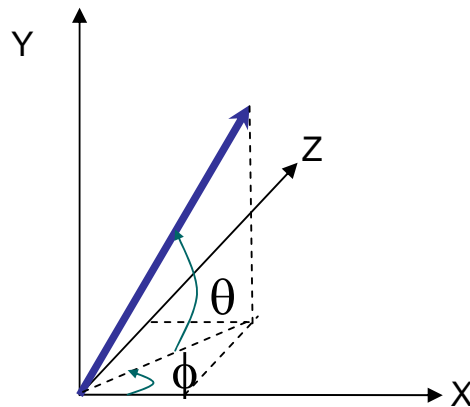

Fig. 1. Definition of the coordinate system and angle definition with θ being the elevation angle and ϕ the azimuthal angle.

The ion groups include a reduced number of ions in order to speed up the computer calculations, but the ion offsets are chosen at a maximum position of a realistic ion beam in order to model the envelope.

Tab. 1. Set of starting parameters of the different ion groups.

Group	Variable Parameter	Number of Ions	Step Size Variation	Range
1	Elevation angle	5	2°	-4°, .., 0°, ..,+4°
2	Azimuthal angle	5	2°	-4°, .., 0°, ..,+4°
3	Coordinate Y	5	0.3 mm	[-0.6,…, 0,…,+0.6] mm
4	Coordinate Z	5	0.3 mm	[-0.6,…, 0,…, +0.6] mm
5	Energy	6	2 eV	[0 – 12] eV

Using these beams we start to adjust the potentials of the electrodes in order to guide and focus the beam from the ion creation region towards the detector. The ion beam trajectories for a set of optimized values in the electrodes is shown in Fig. 2. These values are given in Tab. 2.
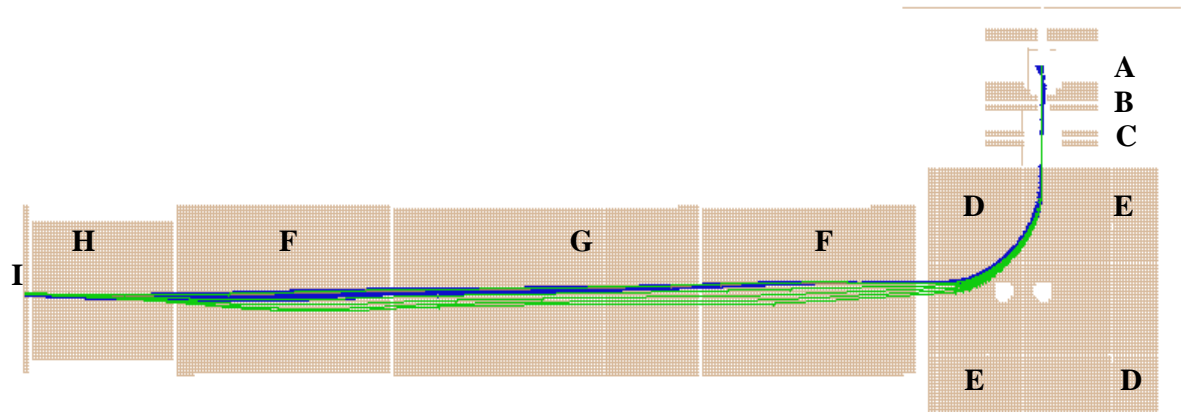
Fig. 2 Ion beam trajectories from the ion creation region in (A) to the detection region in (I) for an optimized set of parameters.

Tab. 2. Optimized electrode parameters.

	Electrode	Voltage/V
A	Ion Region	+ 40
B	Extractor	- 10
C	Lens 1&3 Ionizer	- 120
C	Lens 2 Ionizer	grounded
D	Bender Pair 1	- 36
E	Bender Pair 2	+ 36
F	Einzel lens 1&3	- 500
G	Einzel lens 2	grounded
H	Drift Segment	grounded
I	Detector	- 2000

Appendix B

Drawings
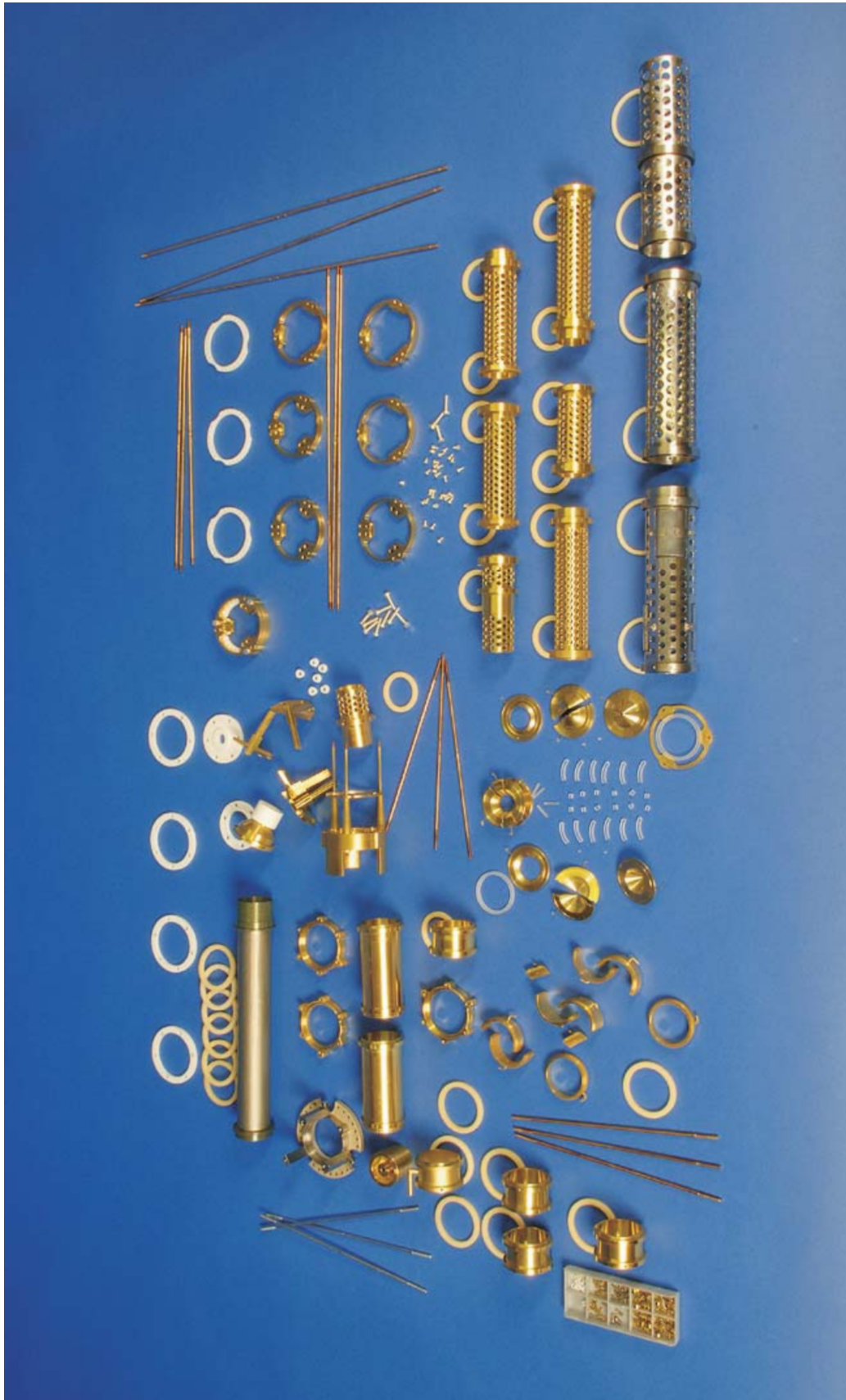
Figure B.1: Photo of all pieces used in the cryogenic Penning trap prior their assembling in the vacuum chamber. The OFE copper electrodes are covered with a silver layer (5-10 μm) to avoid the diffusion of the external gold layer, which avoid oxidation and thus a distortion of the electrostatic potential. Macor and Sapphire are used for isolation of the different parts.

Figure B.2: Zoom on the connection between the purification and measurement traps through the pumping barrier.

Figure B.3: Future layout of the SHIPTRAP setup with the cryogenic Penning trap system.

Bibliography

[1] G. Audi, O. Bersillon, J. Blanchot, and A. H. Wapstra,
The NUBASE evaluation of nuclear and decay properties,
Nucl. Phys. A **729** (2003) 3.

[2] R. A. Brightsen,
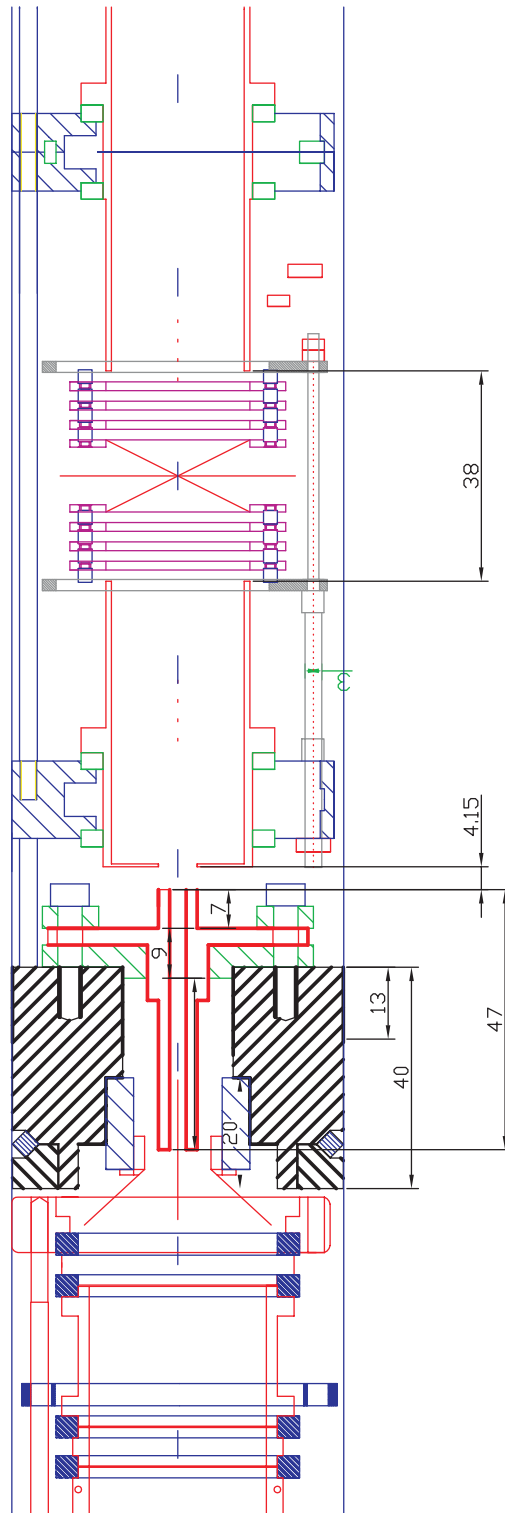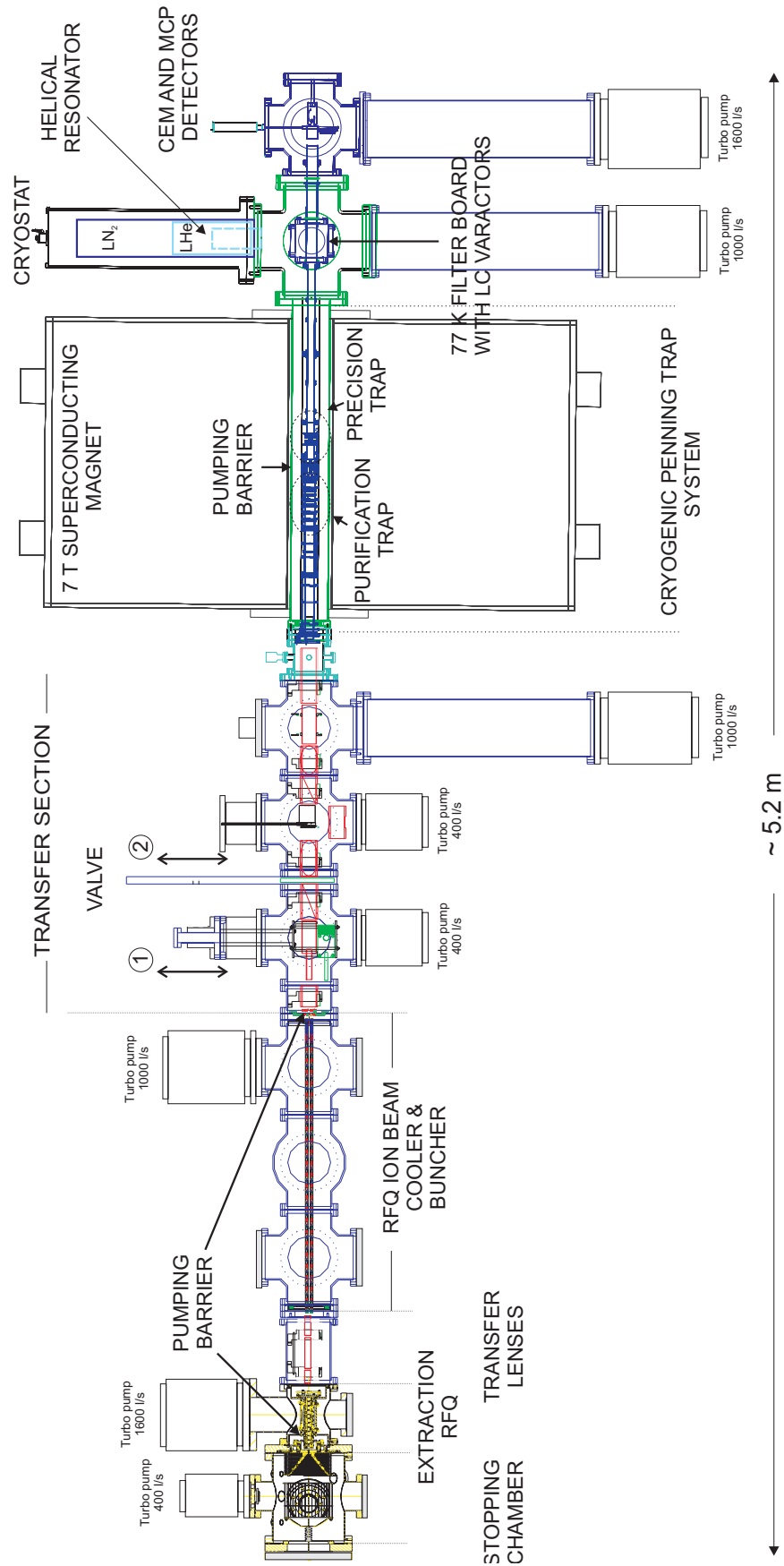*The Nucleon Cluster Model and Thermal Neutron Fission,*
Infinite Energy **31** (2000) 55.

[3] M. Huyse,
The why and how of radioactive beam research,
Lecture Notes Phys., Springer **651** (2004) 32.

[4] K. Blaum,
High-accuracy mass spectrometry with stored ions,
Phys. Rep. **425** (2006) 1.

[5] D. Lunney,
Latest trends in the ever-surprising field of mass measurements,
Eur. Phys. J. A **25** s01 (2005) 3.

[6] D. Lunney, J. M. Pearson, and C. Thibault,
Recent trends in the determination of nuclear masses,
Rev. Mod. Phys. **75** (2003) 1021.

[7] R.-D. Herzberg, P. T. Greenlees, P. A. Butler, G. D. Jones, M. Venhart,
I. G. Darby, S. Eeckhaudt, K. Eskola, T. Grahn, C. Gray-Jones, F. P.
Heßberger, P. Jones, R. Julin, S. Juutinen, S. Ketelhut, W. Korten, M.
Leino, A.-P. Leppänen, S. Moon, M. Nyman, R. D. Page, J. Pakarinen, A.
Pritchard, P. Rahkila, J. Sarén, C. Scholey, A. Steer, Y. Sun, Ch. Theisen,
and J. Uusitalo,
*Nuclear isomers in superheavy elements as stepping stones towards the
island of stability,*
Nature **442** (2006) 896.

[8] S. Hofmann and G. Münzenberg,
The discovery of the heaviest elements,
Rev. Mod. Phys. **72** (2000) 733.

[9] J. C. Hardy and I. S. Towner,
Superallowed $0^+ \longrightarrow 0^+$ β decays: A critical survey with tests of the conserved vector current hypothesis and the standard model,
Phys. Rev. C **71** (2005) 055501.

[10] K. Langanke, F. K. Thielemann, and M. Wiescher,
      Nuclear astrophysics and nuclei far from stability,
      Lecture Notes Phys., Springer **651** (2004) 383.

[11] H. Schatz and K. E. Rehm,
      X-ray binaries,
      Nucl. Phys. A**777** (2006) 601.

[12] F. Kaeppeler, F.-K. Thielemann, and M. Wiescher,
      Current quests in nuclear astrophysics and experimental approaches,
      Annu. Rev. Nuc. Part. Sci. **48** (1998) 175.

[13] H. Schatz,
      The importance of nuclear masses in the astrophysical rp-process,
      Int. J. Mass Spectr. **251** (2006) 293.

[14] H.-J. Kluge, K. Blaum, F. Herfurth, and W. Quint,
      Atomic and Nuclear Physics with Stored Particles in Ion Traps,
      Physica Scripta **T104** (2003) 167.

[15] A. G. Marshall,
      *Milestones in Fourier transform ion cyclotron resonance mass
      spectrometry technique developments,*
      Int. J. Mass Spect. **200** (2000) 331.

[16] F. M. Penning,
      Verzögerungen bei der Zündung von gasgefüllten Photozellen im Dunkeln,
      Physica **3** (1936) 563.

[17] J. R. Pierce,
      Theory and Design of Electron Beams,
      D. van Nostrand Co., New York 1949 (Chapter 3).

[18] W. Paul and H. Steinwedel,
      Ein neues Massenspektrometer ohne Magnetfeld,
      Z. Naturf. **8a** (1953) 448.

[19] K. Blaum, Ch. Geppert, P. Müller, W. Nörtershäuser, E. W. Otten, A.
      Schmitt, N. Trautmann, K. Wendt, and B. A. Bushaw,
      *Properties and performance of a quadrupole mass filter used for resonance
      ionization mass spectrometry,*
      Int. J. Mass Spectrom. **181** (1998) 67.

[20] W. Paul, H. P. Reinhard, and U.v. Zahn,
      Das elektrische Massenfilter als Massenspektrometer und Isotopentrenner,
      Z. Phys. **152** (1958) 143.

[21] W. Paul,
      Electromagnetic traps for charged and neutral particles,
      Rev. Mod. Phys. **62** (1990) 531.

[22] R. S. Van Dyck, Jr., Paul B. Schwinberg, and Hans G. Dehmelt,
New high-precision comparison of electron and positron g-factors,
Phys. Rev. Lett. **59** (1987) 26.

[23] G. Gabrielse, D. Hanneke, T. Kinoshita, M. Nio, and B. Odom,
*New Determination of the Fine Structure Constant from the Electron
g Value and QED,*
Phys. Rev. Lett. **97** (2006) 030802.

[24] J. Verdú, T. Beier, S. Djekić, H.-J. Kluge, W. Quint, S. Stahl,
T. Valenzuela, M. Vogel, and G. Werth,
Electronic g-Factor of Hydrogenlike Oxygen $^{16}O^{7+}$,
Phys. Rev. Lett. **92** (2004) 093002.

[25] G. Werth, J. Alonso, T. Beier, K. Blaum, S. Djekic, H. Häffner,
N. Hermanspahn, W. Quint, S. Stahl, J. Verdú, T. Valenzuela,
and M. Vogel,
Highly charged ions, quantum-electrodynamics, and the electron mass,
Int. J. Mass Spectrom. **251** (2006) 152.

[26] T. Beier, H. Häffner, N. Hermanspahn, S. Karshenboim, H.-J. Kluge,
W. Quint, S. Stahl, J. Verdú, and G. Werth,
New Determination of the Electron's Mass,
Phys. Rev. Lett. **88** (2001) 011603.

[27] R. S. Van Dyck, Jr., F. L. Moore, D. L. Farnham, and P. B. Schwinberg,
Bull. Am. Phys. Soc. **31** (1986) 244.

[28] G. Gabrielse, D. S. Hall, C. Heimann, W. Jhe, H. Kalinowsky,
and A. Khabbaz,
*Precision Mass Spectroscopy of the Antiproton and Proton Using
Simultaneously Trapped Particles,*
Phys. Rev. Lett. **82** (1999) 3198.

[29] H. Dehmelt,
Experiments with an isolated subatomic particle at rest,
Rev. Mod. Phys. **62** (1990) 525.

[30] G. Bollen,
Traps for rare isotopes,
Lect. Notes Phys., Springer **651** (2004) 169.

[31] F. Herfurth, J. Dilling, A. Kellerbauer, G. Bollen, S. Henry, H.-J. Kluge,
E. Lamour, D. Lunney, R.B. Moore, C. Scheidenberger, S. Schwarz, G.
Sikler, and J. Szerypo,
*A linear radiofrequency ion trap for accumulation, bunching, and emit-
tance improvement of radioactive ion beams,*
Nuc. Instrum. Meth. A **469** (2001) 254.

[32] D. Rodríguez Rubiales,
An RFQ buncher for accumulation and cooling of heavy radionuclides at

SHIPTRAP and high precision mass measurements on unstable Kr isotopes at ISOLTRAP,
Ph.D. Thesis, University of Valencia, Spain (2003).

[33] L. S. Brown and G. Gabrielse,
Precision spectroscopy of a charged particle in an imperfect Penning trap,
Phys. Rev. A **25** (1982) 2423.

[34] F. G. Major, V. N. Gheorghe, and G. Werth,
Charged particle traps: The physics and techniques of charged particle field confinement,
Springer (2004).

[35] L. S. Brown and G. Gabrielse,
Geonium theory: Physics of a single electron or ion in a Penning trap,
Rev. Mod. Phys. **58** (1986) 233.

[36] P. W. Anderson,
Theory of flux creep in hard superconductors,
Phys. Rev. Lett. **9** (1962) 309.

[37] M. Block, D. Ackermann, K. Blaum, A. Chaudhuri, Z. Di, S. Eliseev,
R. Ferrer, D. Habs, F. Herfurth, F. P. Heßberger, S. Hofmann, H.-J. Kluge,
G. Maero, A. Martín, G. Marx, M. Mazzocco, M. Mukherjee,
J. B. Neumayr, W.R. Plaß, W. Quint, S. Rahaman, C. Rauth, D. Rodríguez, C. Scheidenberger, L. Schweikhard, P. G. Thirolf, G. Vorobjev, and C. Weber,
Towards direct mass measurements of nobelium at SHIPTRAP,
Eur. Phys. J. D (2007) 10.1140/epjd/e2007-00189-2.

[38] C. Yazidjian, K. Blaum, R. Ferrer, F. Herfurth, A. Herlert, H.-J. Kluge, and L. Schweikhard,
A new Channeltron-detector setup and regulation systems for ISOLTRAP,
Hyp. Interactions (2007) 10.1007/s10751-007-9555-y.

[39] D. J. Wineland and H. G. Dehmelt,
Principles of the stored ion calorimeter,
J. Appl. Phys. **46** (1975) 919.

[40] G. Bollen, H.-J. Kluge, M. König, T. Otto, G. Savard, H. Stolzenberg, R. B. Moore, G. Rouleau, G. Audi, and the ISOLDE Collaboration,
Resolution of nuclear ground and isomeric states by a Penning trap mass spectrometer,
Phys. Rev. C **46** (1992) R2140.

[41] A. Kellerbauer, K. Blaum, G. Bollen, F. Herfurth, H.-J. Kluge,
M. Kuckein, E. Sauvan, C. Scheidenberger, and L. Schweikhard,
From direct to absolute mass measurements: A study of the accuracy of ISOLTRAP,
Eur. Phys. J. D **22** (2003) 53.

[42] K. Blaum, G. Bollen, F. Herfurth, A. Kellerbauer, H.-J. Kluge, M. Kuck-
     ein, S. Heinz, P. Schmidt, and L. Schweikhard,
     *Recent developments at ISOLTRAP: towards a relative mass accuracy of
     exotic nuclei below 10^{-8},*
     J. Phys. B **36** (2003) 921.

[43] G. Bollen, R. B. Moore, G. Savard, and H. Stolzenberg,
     *The accuracy of heavy-ion mass measurements using time of flight-ion
     cyclotron resonance in a Penning trap,*
     J. Appl. Phys. **68** (1990) 4355.

[44] R. Ringle, G. Bollen, P. Schury, S. Schwarz, and T. Sun,
     *Octupolar excitation of ion motion in a Penning trap - A study performed
     at LEBIT,*
     Int. J. Mass Spectr. **262** (2007) 33.

[45] S. Eliseev, M. Block , A. Chaudhuri, F. Herfurth, H.-J. Kluge, A. Martín,
     C. Rauth, and G. Vorobjev,
     *Octupolar excitation of ions stored in a Penning trap mass spectrometer
     - A study performed at SHIPTRAP,*
     Int. J. Mass Spectr. **262** (2007) 45.

[46] M. Mukherjee,
     The mass of ^{22}Mg and a concept for a novel laser ion source trap,
     Ph.D. Thesis, University of Heidelberg, Germany (2005).

[47] G. Savard, St. Becker, G. Bollen, H.-J. Kluge, R. B. Moore, Th. Otto,
     L. Schweikhard, H. Stolzenberg, and U. Wiess,
     A new cooling technique for heavy ions in a Penning trap,
     Phys. Lett. A **158** (1991) 247.

[48] E. de Hoffmann and V. Sroobant,
     Mass Spectrometry: Principles and Applications,
     John Wiley and Sons (2007)

[49] R. Kirchner,
     Review of ISOL target-ion-source systems,
     Nucl. Instrum. Meth. B **204** (2003) 179.

[50] R. Kirchner,
     Progress in ion source development for on-line separators,
     Nucl. Instrum. Meth. **181**(1981) 275.

[51] Y. Fujii, H. Iwabuchi, M. Nomura, K. Iio, and T. Suzuki,
     Surface ionization mechanism of alkali halides,
     Vacuum **47** (1996) 501.

[52] R. Kirchner,
     The ion-source for the GSI on-line separator,
     Nucl. Instrum. Meth. **186** (1981) 295.

[53] S. Ohshimaa, A. Fujisawa, H. Nakano, and A. Shimizu,
Development of zeolite ion source for beam probe measurements of high temperature plasma,
Rev. Sci. Intrum. **77** (2006) 03B704.

[54] R. Kirchner,
On the thermoionization in hot cavities,
Nucl. Instrum. Meth. A **292** (1990) 203.

[55] *Axial Molecular Beam Ionizer User Manual,*
ABB Automation Inc. Analytical Division - Extrel.

[56] K. Blaum, G. Bollen, F. Herfurth, A. Kellerbauer, H.-J. Kluge, M. Kuckein, E. Sauvan, C. Scheidenberger, and L. Schweikhard,
Carbon clusters for absolute mass measurements at ISOLTRAP,
Eur. Phys. J. A **15** (2002) 245.

[57] A. Chaudhuri, M. Block, S. Eliseev, R. Ferrer, F. Herfurth, A. Martín, G. Marx, M. Mukherjee, C. Rauth, L. Schweikhard, and G. Vorobjev,
Carbon-cluster mass calibration at SHIPTRAP,
Eur. Phys. J. D (2007) 10.1140/epjd/e2007-00001-5.

[58] D. J. Morrissey and B. M. Sherrill,
In-Flight Separation of Projectile Fragments,
Lect. Notes Phys., Springer **651** (2004) 113.

[59] G. Münzenberg, H. Ewald, W. Faust, K. Günter, S. Hofmann, and P. Armbruster,
The velocity filter SHIP, a separator of unslowed heavy ion fusion products,
Nucl. Instrum. Meth. **161** (1979) 65.

[60] E. Kugler,
The ISOLDE facility,
Hyp. Interactions **129** (2000) 23.

[61] G. Gräff, H. Kalinowsky, and J. Traut,
A direct determination of the proton electron mass ratio,
Z. Phys. A **297** (1980) 35.

[62] M. König, G. Bollen, H.-J. Kluge, T. Otto, and J. Szerypo,
Quadrupole excitation of stored ion motion at the true cyclotron frequency,
Int. J. Mass Spectrom. **142** (1995) 95.

[63] S. George, K. Blaum, F. Herfurth, A. Herlert, M. Kretzschmar, Sz. Nagy, S. Schwarz, L. Schweikhard, and C. Yazidjian,
The Ramsey method in high-precision mass spectrometry with Penning traps: Experimental results,
Int. J. Mass Spectrom. **264** (2007) 110.

[64] S. George, S. Baruah, B. Blank, K. Blaum, M. Breitenfeldt, U. Hager, F. Herfurth, A. Herlert, A. Kellerbauer, H.-J. Kluge, M. Kretzschmar, D.

Lunney, R. Savreux, S. Schwarz, L. Schweikhard, and C. Yazidjian
Ramsey Method of Separated Oscillatory Fields for High-Precision Penning Trap Mass Spectrometry
Phys. Rev. Lett. **98** (2007) 162501.

[65] C. Rauth,
Direct mass measurements beyond the proton drip-line,
Ph.D. Thesis, University of Heidelberg, Germany (2006).

[66] M. Dworschak,
Optimierung der Zyklotronfrequenzbestimmung und Hochpräzisions-massenmessungen an neutronenreichen Zinnisotopen mit ISOLTRAP,
Diploma Thesis, University of Mainz, Germany (2006).

[67] *Channeltron Electron Multiplier handbook for mass spectrometry applications,*
Burle Technologies, Inc.
http://www.burle.com/cgi-bin/byteserver.pl/pdf/ChannelBook.pdf

[68] C. Yazidjian,
A new detector setup for ISOLTRRAP and test of the Isobaric Multiplet Mass Equation,
Ph.D. Thesis, University of Caen, France (2006).

[69] W. Shockley,
Currents to conductors induced by a moving point charge,
J. Appl. Phys. **9** (1938) 635.

[70] S. Guan and A. G. Marshall,
Ion traps for Fourier transform ion cyclotron resonance mass spectrometry: principles and design of geometric and electric configurations,
Int. J. Mass Spectrom. Ion Proc. **146/147** (1995) 261.

[71] M. B. Comisarow,
Signal modeling for ion cyclotron resonance,
J. Chem. Phys. **69** (1978) 4097.

[72] L. Schweikhard,
Theory of quadrupole detection Fourier Transform-Ion Cyclotron Resonance,
Int. J. Mass Spectrom. Ion Proc. **107** (1991) 281.

[73] M. B. Comisarow and A. L. Marshall,
Fourier transform ion cyclotron resonance,
Chem. Phy. Lett **25** (1974) 282.

[74] M. B. Comisarow and A. L. Marshall,
The early development of Fourier transform ion cyclotron resonance (FT-ICR) spectroscopy,
J. Mass Spectr. **31** (1996) 581.

[75] R. T. Kouzes,
Fourier transform ion cyclotron resonance versus time of flight for precision mass measurements,
Hyp. Interactions **81** (1993) 123.

[76] A. G. Marshall, C. L. Hendrickson, and G. S. Jackson,
Fourier transform ion cyclotron resonance mass spectrometry: a primer,
Mass Spectr. Rev. **17** (1998) 1.

[77] C. Weber,
Konzeption eines kryogenen Penningfallenaufbaus für SHIPTRAP und Massenbestimmungen von Radionukliden um den Z = 82-Schalenabschluss an ISOLTRAP,
Ph.D. Thesis, University of Heidelberg, Germany (2004).

[78] S. Stahl,
Aufbau eines Experiments zur Bestimmung von elektronischer g-Faktoren einzelner wasserstoffähnlicher Ionen,
Ph.D. Thesis, University of Mainz, Germany (1998).

[79] J. Ketelaer,
Development of a non-destructive Fourier Transform-Ion Cyclotron Resonance detection system for singly charged ions in a cryogenic Penning trap,
Diploma thesis, University of Mainz, Germany (2006).

[80] J. Dilling, D. Ackermann, J. Bernard, F. P. Heßberger, S. Hofmann, W. Hornung, H. J. Kluge, E. Lamour, M. Maier, R. Mann, G. Marx, R. B. Moore, G. Münzenberg, W. Quint, D. Rodriguez, M. Schädel, J. Schönfelder, G. Sikler, C. Toader, L. Vermeeren, C. Weber, G. Bollen, O. Engels, D. Habs, P. Thirolf, H. Backe, A. Dretzke, W. Lauth, W. Ludolphs, and M. Sewtz,
The SHIPTRAP project: A capture and storage facility at GSI for heavy radionuclides from SHIP,
Hyp. Interact. **127** (2000) 491.

[81] M. Block, D. Ackermann, D. Beck, K. Blaum, M. Breitenfeldt, A. Chauduri, A. Doemer, S. Eliseev, D. Habs, S. Heinz, F. Herfurth, F. Heßberger, S. Hofmann, H. Geissel, H. -J. Kluge, V. Kolhinen, G. Marx, J. Neumayr, M. Mukherjee, M. Petrick, W. Plass, W. Quint, S. Rahaman, C. Rauth, D. Rodríguez, C. Scheidenberger, L. Schweikhard, M. Suhonen, P. Thirolf, Z. Wang, C. Weber, and the SHIPTRAP Collaboration,
The ion-trap facility SHIPTRAP,
Eur. Phys. J. A. **25** S01 (2005) 49.

[82] J. Dilling, D. Ackermann, F. Heßberger, S. Hofmann, H.-J. Kluge, G. Marx, G. Münzenberg, Z. Patyk, W. Quint, D. Rodríguez, C. Scheidenberger, J. Schönfelder, G. Sikler, A. Sobiczewski, C. Toader, and C. Weber,
A Physics Case for SHIPTRAP: Measuring the Masses of Transuranium Elements,
Hyp. Interactions **132** (2001) 495.

[83] J. B. Neumayr, L. Beck, D. Habs, S. Heinz, J. Szerypo, P. G. Thirolf, V. Varentsov, F. Voit, D. Ackermann, D. Beck, M. Block, Z. Di, S. A. Eliseev, H. Geissel, F. Herfurth, F. P. Heßberger S. Hofmann, H.-J. Kluge, M. Mukherjee, G. Münzenberg, M. Petrick, W. Quint, S. Rahaman, C. Rauth, D. Rodríguez, C. Scheidenberger, G. Sikler, Z. Wang, C. Weber, W. R. Plaß, M. Breitenfeldt, A. Chaudhuri, G. Marx, L. Schweikhard, A. F. Dodonov, Y. Novikov, and M. Suhonen,
The ion-catcher device for SHIPTRAP,
Nucl. Instr. Meth. B **244** (2006) 489.

[84] G. Sikler,
Massenspektrometrie kurzlebiger Sr- und Sn- Isotope und Aufbau der SHIPTRAP-Penningfallen,
Ph.D. Thesis, University of Heidelrberg, Germany (2003).

[85] H. Raimbault-Hartmann, D. Beck, G. Bollen, M. König, H.-J. Kluge, E. Schark, J. Stein, S. Schwarz, and J. Szerypo,
A Cylindrical Penning Trap for Capture, Mass Selective Cooling and Bunching of Radioactive Ion Beams,
Nucl. Instr. Meth. B**126** (1997) 378.

[86] H. Schatz, A. Aprahamian, V. Barnard, L. Bildsten, A. Cumming, M. Ouellette, T. Rauscher, F.-K. Thielemann, and M. Wiescher,
End Point of the rp Process on Accreting Neutron Stars,
Phys. Rev. Lett. **86** (2001) 3471.

[87] R. R. C. Clement, W. Benenson, B. A. Brown, W. A. Richter, H. Schatz, B. M. Sherrill, and A. Volya,
Sensitivities of rp-process calculations to nuclear mass uncertain ties,
Nucl. Phys. A **718** (2003) 617.

[88] G. Vorobjev, D. Ackermann, D. Beck, K. Blaum, M. Block, A. Chaudhuri, Z. Di, S. Eliseev, R. Ferrer, D. Habs, F. Herfurth, F. Heßberger, S. Hofmann, H.-J. Kluge, G. Maero, A. Martín, G. Marx, C. Rauth, D. Rodríguez, C. Scheidenberger, L. Schweikhard, M. Sewtz, P. Thirolf, W. Quint, and C. Weber,
Mass measurements of radionuclides near the endpoint of the rp-process at SHIPTRAP,
Proceedings of Science (NIC-IX) 208 (2006).

[89] M. Mazzoco, private communication.

[90] B. A. Brown, R. R. C. Clement, H. Schatz, A. Volya, and W. A. Richter,
Proton drip-line calculations and the rp process,
Phys. Rev. C **65** (2002) 045802.

[91] D. Rodríguez, V. S. Kolhinen, G. Audi, J. Äystö , D. Beck, K. Blaum, G. Bollen, F. Herfurth, A. Jokinen, A. Kellerbauer, H.-J. Kluge, M. Oinonen, H. Schatz, E. Sauvan, and S. Schwarz,
Mass measurement on the rp-process waiting point ^{72}Kr,
Phys. Rev. Lett. **93** (2004) 161104.

[92] J. A. Clark, G. Savard, K. S. Sharma, J. Vaz, J. C. Wang, Z. Zhou, A. Heinz, B. Blank, F. Buchinger, J. E. Crawford, S. Gulick, J. K. P. Lee, A. F. Levand, D. Seweryniak, G. D. Sprouse, and W. Trimble,
Precise mass measurement of ^{68}Se, a waiting-point nuclide along the rp process,
Phys. Rev. Lett. **92** (2004) 192501.

[93] M. Block, D. Ackermann, K. Blaum, A. Chaudhuri, Z. Di, S. Eliseev, R. Ferrer, D. Habs, F. Herfurth, F. P. Heßberger, S. Hofmann, H.-J. Kluge, G. Maero, A. Martín, G. Marx, M. Mazzocco, M. Mukherjee, J. B. Neumayr, W. R. Plaß, W. Quint, S. Rahaman, C. Rauth, D. Rodríguez, C. Scheidenberger, L. Schweikhard, P. G. Thirolf, G. Vorobjev, and C. Weber,
Mass measurements in the endpoint region of the rp-process at SHIP-TRAP,
Hyp. Interactions (2007) 10.1007/s10751-007-9550-3.

[94] D. Kast, A. Jungclaus, A. Harder, K. P. Lieb, D. Rudolph, R. Schubart, H. Grawe, D. Foltescu, H. A. Roth, Ö. Skeppstedt, I. Bearden, and T. Shizuma,
First identification and shell model structure of ^{92}Rh,
Z. Phys. A **356** (1997) 363.

[95] A. Kellerbauer, K. Blaum, G. Bollen, F. Herfurth, H.-J. Kluge, M. Kuckein, E. Sauvan, C. Scheidenberger, and L. Schweikhard,
From direct to absolute mass measurements: A study of the accuracy of ISOLTRAP,
Eur. Phys. J. D **22** (2003) 53.

[96] R. Birge,
The calculation of errors by the method of least squares,
Phys. Rev. **40** (1932) 207.

[97] D. Tománek, M. A. Schluter,
Growth regimes of carbon clusters,
Phys. Rev. Lett. **65** (1991) 2331.

[98] G. Audi, A. H. Wapstra, and C. Thibault
The AME2003 atomic mass evaluation (II). Tables, graphs and references,
Nucl. Phys. A **729** (2003) 337.

[99] P. J. Mohr and B. N. Taylor,
CODATA Recommended Values of the Fundamental Physical Constants: 1998,
J. Phys. Chem. Ref. Data **28** (1999) 1713.

[100] A. H. Wapstra, G. Audi, and C. Thibault,
The AME2003 atomic mass evaluation (I). Evaluation of input data, adjustment procedures,
Nucl. Phys. A **729** (2003) 129.

[101] K. Oxorn and S. K. Mark,
The Beta Decay of ^{90g}Tc and ^{90m}Tc,
Z. Phys. A **303** (1981) 63.

[102] R. Iafigliola, S. C. Gujrathi, B. L. Tracy, and J. K. P. Lee,
The Mass Excesses of ^{91}Tc and ^{90}Tc,
Can. J. Phys. **52** (1974) 96.

[103] D. Rudolph, C. J. Gross, M. K. Kabadiyski, K. P. Lieb, M. Weiszflog, H. Grawe, J. Heese, K. -H. Maier, and J. Eberth,
High spin shell model states in the isotope $^{90}_{43}Tc_{47}$,
Phys. Rev. C **47** (1993) 2574.

[104] R. Bass,
Nuclear reactions with heavy ions,
Text and monographs in physics, Springer (1980).

[105] K. Heiguchi, T. Hosoda, T. Komatsubara, T. Nomura, K. Furuno, R. Nakatani, S. Mitarai, and T. Kuroyanagi,
Half-lives and Q_β measurements for new nuclei of ^{89}Tc and ^{89m}Tc,
Z. Phys. A **338** (1991) 7.

[106] E. Hagberg, J. C. Hardy, H. Schmeing, E. T. H. Clifford, and V. T. Koslowsky,
The decays of the $T_z = 3/2$ β-delayed proton precursors ^{83}Zr, ^{87}Mo and ^{91m}Ru,
Nucl. Phys. A **395** (1983) 152.

[107] C. F. Moore, P. Richard, C. E. Watson, D. Robson, J. D. Fox,
Isobaric Analogue States in Heavy Nuclei. I. Molybdenum Isotopes,
Phys. Rev. **141** (1966) 1166.

[108] S. I. Hayakawa, S. K. Mark, J. K. Lee, J. E. Kitching, G. C. Ball, and W. G. Davies,
Study of low-lying states in ^{92}Tc with the $^{92}Mo(^3He,t)$ reaction,
Nucl. Phys. A **199** (1973) 560.

[109] J. B. Ball,
Studies of ^{95}Ru and ^{94}Ru with the $^{96}Ru(p,d)$ and (p,t) reactions,
Nucl. Phys. A **160** (1971) 225.

[110] R. Ferrer, K. Blaum, M. Block, F. Herfurth, J. Ketelaer, Sz. Nagy, D. Neidherr, C. Weber, and the SHIPTRAP collaboration,
Development of a Fourier-Transform Ion-Cyclotron-Resonance detection for short-lived radionuclides at SHIPTRAP,
Eur. Phys. J. A (2007) in press.

[111] C. Rauth, D. Ackermann, G. Audi, M. Block, A. Chaudhuri, S. Eliseev, F. Herfurth, F. P. Heßberger, S. Hofmann, H.-J. Kluge, A. Martín, G. Marx, M. Mukherjee, J. B. Neumayr, W. R. Plaß, S. Rahaman, D. Rodríguez, L. Schweikhard, P. G. Thirolf, G. Vorobjev, C. Weber, and the SHIPTRAP

Collaboration,
Direct mass measurements around A = 146 at SHIPTRAP,
Eur. Phys. J. A (2007) In press.

[112] G. Gabrielse,
Relaxation calculations of the electrostatic properties of compensated Penning traps with hyperbolic electrodes,
Phys. Rev. A **27** (1983) 2277.

[113] M. Wutz, H. Adam, W. Walcher, and K. Jousten,
Handbuch Vakuumtechnik,
Vieweg, Braunschweig-Wiesbaden (2000).

[114] D. Neidherr,
Entwicklung einer Pumpsperre für das Penning-Falle-Massenspektrometer SHIPTRAP,
Diploma Thesis, University of Mainz, Germany (2006).

[115] G. Kiese, private communication from EBARA-Europe, Cologne (2006).

[116] B. Brehm, J. Grosser, T. Rusheinski, and M. Zimmer,
Absolute detection efficiencies of a microchannel plate detector for ions,
Meas. Sci. Technol. **6** (1995) 953.

[117] J. Oberheide, P. Wilhelms, and M. Zimmer,
New results on the absolute ion detection efficiencies of a microchannel plate,
Meas. Sci. Technol. **8** (1997) 354.

[118] Dr. Stefan Stahl, Kellerweg 23, 67582 Mettenheim, Germany.

[119] Stanford Research Systems,
Network Signal Analyzer SR780,
Operating manual and programming reference (1996).

[120] M. P. Bradley, J. V. Porto, S. Rainville, J. K. Thompson, and D. E. Pritchard,
Penning Trap Measurements of the Masses of ^{133}Cs, $^{87,85}Rb$, and ^{23}Na with Uncertainties ≤ 0.2 ppb,
Phys. Rev. Lett. **83** (1999) 4510.

[121] L. Schweikhard,
Excitation and detection geometries for Fourier-transform mass spectrometry,
Rap. Com. Mass Spectr. **8** (1994) 10.

[122] L. Schweikhard, M. Lindinger, and H.-J. Kluge,
Quadrupole-detection FT-ICR mass spectrometry,
Int. J. Mass Spectr. **98** (1990) 25.

[123] D. Cappelletti, G. Liuti, and F. Pirani,
Generalization to ion-neutral systems of the polarizability correlations for interaction potential parameters,
Chem. Phys. Lett. **183** (1991) 297.

[124] E. Ledford, Jr., D. Rempel, and M. Gross,
Space charge effects in Fourier transform mass spectrometry. Mass calibration,
Anal. Chem. **56** (1984) 2744.